UNIVERSIDAD DE CHILE
FACULTAD DE CIENCIAS FÍSICAS Y MATEMÁTICAS
DEPARTAMENTO DE INGENIERÍA CIVIL

CARACTERIZACIÓN Y ESTUDIO DE LA RESPUESTA DE HORMIGÓN REFORZADO CON FIBRAS DE PVA

TESIS PARA OPTAR AL GRADO DE MAGÍSTER EN CIENCIAS DE LA INGENIERÍA, MENCIÓN INGENIERÍA ESTRUCTURAL, SÍSMICA Y GEOTÉCNICA

MEMORIA PARA OPTAR AL TÍTULO DE INGENIERO CIVIL

JAIME HÉCTOR REVECO ARRIOLA

PROFESOR GUÍA:
LEONARDO MASSONE SÁNCHEZ

MIEMBROS DE LA COMISIÓN:
FABIÁN ROJAS BARRALES
RAÚL HERNÁN SANTA MARÍA OYANEDEL

SANTIAGO DE CHILE
2021

RESUMEN DE LA MEMORIA PARA OPTAR
AL TÍTULO DE MAGÍSTER EN CIENCIAS
DE LA INGENIERÍA MENCIÓN ESTRUCTURAL,
SÍSMICA Y GEOTÉCNICA
Y AL TÍTULO DE INGENIERO CIVIL
POR: **JAIME HÉCTOR REVECO ARRIOLA**
FECHA: ENERO 2021
PROF. GUÍA: LEONARDO MASSONE S.

CARACTERIZACIÓN Y ESTUDIO DE LA RESPUESTA DE HORMIGÓN REFORZADO CON FIBRAS DE PVA

Las fibras han sido usadas a lo largo de la historia en la construcción como adición que refuerza la característica quebradiza del concreto. Las fibras sintéticas de alcohol polivinílico (PVA) poseen una buena interacción con la matriz de concreto, además tiene excelentes propiedades mecánicas comparada con otras fibras. Debido a esto, ha sido comúnmente utilizada en la industria como refuerzos de morteros, sin embargo, su comportamiento con mezclas de concreto con árido grueso no ha sido estudiada a cabalidad. La siguiente investigación consiste en el análisis del comportamiento de hormigón con árido grueso reforzado con 0.62% y 1.23% PVA. El estudio contempla una documentación detallada de lo que se ha realizado y el impacto que ha tenido el uso de fibras en la industria, además, la obtención de las propiedades mecánicas del hormigón con árido grueso reforzado con fibras de PVA, contemplando ensayos hormigón en compresión y tracción. Posteriormente, se realizó un análisis de los datos obtenidos junto con el ensayo de vigas cortas y largas que evaluarán la respuesta del hormigón con árido grueso reforzado con fibras de PVA de miembros estructurales sometidos a un ensayo pushover. Por último, se calibró un modelo analítico que replica el ensayo de vigas anteriormente descrito, capturando y contrastando la respuesta de este. Durante la primera etapa, se realizaron un conjunto de probetas de hormigón reforzado con distintas concentraciones de PVA, variando además el tamaño máximo de árido. La idea es cuantificar la influencia del tamaño de árido y de la concentración de refuerzo de PVA en la mezcla. De aquí, se puede extraer que la fibra de PVA en la mezcla de hormigón con árido grueso, aumenta la deformación máxima y reduce en un 5% aproximadamente la resistencia máxima del elemento en compresión. Por otro lado, los ensayos de tracción arrojaron que la fibra de PVA aumenta la resistencia a tracción del hormigón en un 30%, sin embargo, datos con respecto al cambio de deformación no pudieron ser obtenidos. Las fibras de PVA en el ensayo de vigas cortas cambiaron el modo de falla de corte a flexión, aumentando la deflexión y la capacidad del elemento. También, el ensayo de las vigas esbeltas arrojo que la adición de PVA aumenta la capacidad, pero disminuye la flecha. El ensayo fue replicado mediante un modelo analítico, usando el elemento E-SFI, capturando ambos fenómenos observados en el ensayo.

RESUMEN DE LA MEMORIA PARA OPTAR
AL TÍTULO DE MAGÍSTER EN CIENCIAS
DE LA INGENIERÍA MENCIÓN ESTRUCTURAL,
SÍSMICA Y GEOTÉCNICA
Y AL TÍTULO DE INGENIERO CIVIL
POR: **JAIME HÉCTOR REVECO ARRIOLA**
FECHA: ENERO 2021
PROF. GUÍA: LEONARDO MASSONE S.

EFFECT OF POLYVINYL ALCOHOL (PVA) FIBER ON COARSE AGGREGATE FIBER REINFORCED CONCRETE

Fibers have been used throughout history in the construction field as a strengthener of concrete's brittleness. Polyvinyl-alcohol (PVA) fibers have a strong bond with the concrete matrix, also have excellent mechanical properties compared to other fibers. Therefore, it has been commonly used in the industry as mortar reinforcement, but its behavior with coarse aggregate concrete has not been fully studied yet. The following research analyses the behavior of concrete with coarse aggregate with 0.62% and 1.23% PVA content. The study summarizes the documentation of what has been done and the impact that the use of fibers has had in the industry. Later, performing both tensile and compressive concrete tests obtains coarse aggregate concrete's mechanical properties with PVA addition. Next, one of the mixtures is selected and used to elaborate a short and long beam to assess coarse aggregate concrete's behavior reinforced with PVA fibers of structural members by performing a pushover test. Finally, a computational model was made that replicates the previously described beam test, capturing and contrasting its response. During the first stage, a set of reinforced concrete specimens were made with different PVA content, varying the maximum aggregate size. The idea is to quantify the aggregate size's influence and the PVA content on the concrete mixture. It was noticed that the PVA fiber addition in coarse aggregate concrete increases the maximum strain and barely reduces the concrete maximum compressive strength, approximately 5 %. On the other hand, the tensile tests showed that the PVA fiber increases the tensile strength of concrete specimens by 30 % in coarse aggregate members. PVA fibers addition in short beams changed the failure mode from shear to flexural, increasing the deflection and the member's capacity. On the other hand, the test of long beams revealed that the addition of PVA increases the member's capacity but reduces the deflection. The test was replicated employing a computational model on OpenSees, using E-SFI element, capturing both phenomena observed during the test.

Para mis abuelos,
mi familia,
y mi pareja.

Acknowledgements

Este trabajo, junto a todo lo realizado en mi carrera universitaria no hubiese sido posible sin el apoyo de todos/as los que me rodean. Sus consejos, las vivencias y todo lo que hemos compartido ha ayudado a ser más ameno el duro esfuerzo y sin duda, facilitar el trabajo que estudiar implica. Son muchas personas y es complicado nombrarlas a todas, pero si leen esto, les estoy muy agradecido.

Agradezco además a mi familia, a mi padre y a mi madre por su constante sacrificio y entrega, por sacarnos adelante y siempre apoyarme en todas las decisiones que he tomado. Estoy muy orgulloso del ejemplo que me han dado, de sus valores y de siempre perseverar en situaciones complicadas. Les debo mucho y este trabajo es un grano de arena en la playa de todo lo que ustedes me han dado a mí. A mis tatas, que me criaron cuando mis padres trabajaban y me formaron como la persona que soy hoy en día. Sin duda, esto no hubiese sido posible sin su incondicional apoyo, agradezco al mundo por tenerlos. A mi hermana, que pese a todo lo que hemos pasado en el transcurso de nuestras cortas vidas, siempre me has apoyado con tus risas y tu forma de ser. Los amo a todos!

A Fernanda, mi pareja, sin su apoyo en el transcurso de estos nueve años, nada de esto hubiese sido posible. Agradezco al mundo por juntarnos y caminar juntos por la vida. Por tus risas, consejos, caricias y abrazos, por todo lo que me has dado y ayudado a ser mejor persona cada día, este trabajo es un hito más de todo lo que hemos logrado y que lograremos en el futuro, te amo negra! Agradezco también a su familia de Fernanda, por tratarme como un hijo más y haberme apoyado en todo lo que necesitado.

Ha sido un camino largo, con muchos cambios. Agradezco también a las personas que me dio la universidad, a Pablo, Charlie, Mauro, Gonzo, Pato, Goza, Perro y muchos otros más, por sus vivencias, consejos y apoyo durante mi formación. También, por supuesto, agradezco a Carlos y PP por su amistad, risas, cervezas y consejos, no pude haber encontrado mejores amigos para culminar este proceso. Varios de las personas nombradas ya salieron, espero que siempre les vaya bien, mis mejores deseos sean para ustedes. Como no olvidarme de la pecera de magister, a los Gabos, Lucho, Roberto, Mariale y Camilo, les agradezco su apoyo, sus conversaciones y risas que hicieron más ameno el tiempo que podíamos estar todos juntos.

Por último pero no menos importante, quiero agradecer a mi profesor guía, Leonardo Massone, por los consejos y las conversaciones que me ayudaron enormemente a encausar este trabajo, por permitirme participar como auxiliar y ayudar a formar personas. Quiero agradecer también a las personas que me han ayudado en este camino, a Pedro Soto, Víctor, Omar, Mario, a la gente de IDIEM por facilitar el corte de las probetas y ensayos. He aprendido mucho de ustedes, espero mantener el contacto a futuro.

Contents

List of Tables

List of Figures

Chapter 1

Introduction

1.1. Background

Concrete is one of the most used materials in the construction field. Its mechanical and chemical characteristics give concrete a high compression strength but low tensile strength. Most failures and deterioration of concrete structures are due to the material brittleness. As a result, the construction industry has sought a material with high resistance tension strength for decades, which can provide the concrete a greater tensile strength. As a result of that search, investigators found that adding steel bars to concrete increases its traction strength without compromising its compression behavior. This compound material is called 'Steel Reinforced Concrete' (SRC). From then on, A630-420H (i.e. $f_u = 630$ MPa & $f_y = 420$ MPa) is the steel most commonly used to reinforce concrete, which has excellent mechanical properties both compression and tension, and its capacity to withstand an 8% strain, providing concrete a greater flexural potential.

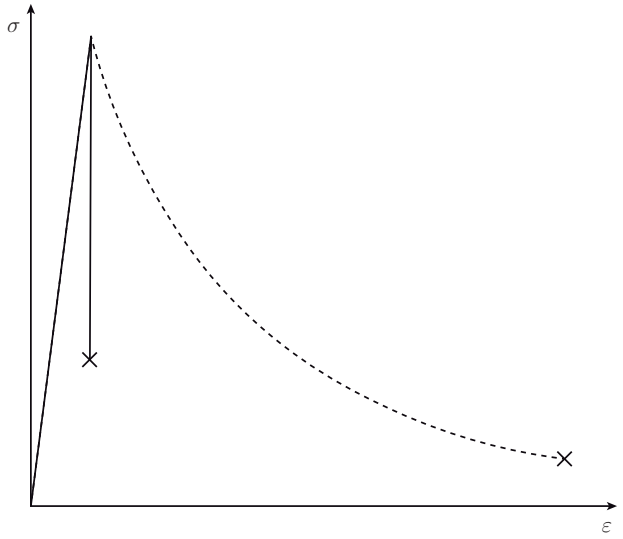

Figure 1.1: Stress-Strain Curve comparison between plain concrete (solid line) and Fiber Reinforced Concrete (dashed line).

Over the years, many researcher have sought for elements that improve both chemical and mechanical concrete properties. Thus far, the most effective way to increase concrete

ductility and tension without considering reinforcing steel is fiber reinforcement. Fibers have a good interaction with the concrete matrix and have exceptional mechanical properties, and can increase the concrete strain, showed in Fig. 1.1 where the plain concrete backbone curve is compared with the fiber reinforced concrete curve. Plenty of investigation projects had helped characterize its influence in concrete response. These studies have found that fiber has a high Young's modulus with members under tension and high deformation resistance.

Polyvinyl-alcohol (PVA) is a water-soluble synthetic polymer, which belongs to the class of water-soluble non-ionic polymers (Thong et al., 2016). It is non-hazardous, and it is considered safe to handle and environmentally friendly. This fiber presents suitable characteristics as an FRC as it has high strength modulus and elastic modulus compared to other fibers, such as polypropylene fiber, nylon fiber, polyethylene fiber. The mechanical behavior of PVA-FRC can be influenced by different factors (i.e., fiber distribution, fiber length, fiber geometry, orientation, etc.). Therefore, it is important to follow a rigorous procedure in the specimens' confection process. FRC is recently widely used for industrial pavements, in small prefabricated elements, in shotcrete, and lately in conventional or segmented tunnels (Cadoni et al., 2009).

It has been demonstrated that flexural strength increases as the fiber content increases. With just a small percentage of fiber content within the matrix, the toughness increases, and on the other side, with a larger amount of fibers, the tensile strength also increases. The main effect of fibers in the concrete matrix has been noticed in the post-cracking zone, where fibers work as a bridge across the fracture zone so that it is possible with a high amount of fiber content reach a multiple-cracking stage of the cementitious element (Pan et al., 2015).

The present study performs an experimental program on the behavior of concrete reinforced with PVA micro-fibers. The purpose of the testing is to obtain stress-strain behavior in tension and compression and assessing the behavior of four concrete beams with PVA reinforced concrete. Sixty-three concrete cylinders were tested in compression (American Society of Testing and Materials., 2015) and six beams were tested under flexural loading (American Society of Testing and Materials., 2010), to determine the tensile concrete capacity. Micro-fibers' properties reinforced concrete elements such as compression strength, flexural strength, load–deflection, first crack toughness, strain-softening behavior, and ductility were determined. Other four beams with traditional reinforcement were also tested to observe the impact of PVA in flexural and shear response.

1.2. Motivation

Thus far, there are not many investigations assessing the response of PVA-FRC in the coarse aggregate concrete matrix. By contrast, most research work has investigated the effectiveness of PVA-FRC on the mortar. The purpose of this research is to characterize the mechanical properties of PVA fiber reinforced concrete and provide information on the influence of aggregate size and quantity of PVA fibers on the response of beams as a structural element. Finally, extrapolate the data to formulate advice on the use of PVA fibers on grater structural elements, such as walls and frame structural systems under seismic actions, whose response (ductility) can be improved by adding fibers.

1.3. Objectives

1.3.1. Main Objective

Study the influence of PVA-FRC microfiber as a coarse aggregated concrete reinforcement through compression and flexural tests. With this, it seeks to calibrate a panel finite element method for a pushover analysis.

1.3.2. Specific Objectives

- Characterize the PVA fiber reinforced concrete (PVA-FRC).
- Calibrate a panel finite element to model analytically a pushover analysis.
- Validate the calibration with flexural and shear beam testing, subducted to a four-point bending test.

Chapter 2

Literature Review

The studies of PVA-FRC fiber as a mortar reinforcement are numerous, the literature review will focus on resuming what have been done, in material testing and finite element analysis.

The review will also address:

- Concrete and its interaction with PVA-FRC fiber.
- Types of fibers and its different concrete responses.
- Concrete testing and tensile strength.

These points follow the order in which they are described above, as a basic understanding of the precursor data is needed to develop the next one.

2.1. FRC and concrete

2.1.1. Reinforced concrete and its properties

Concrete is a mixture of material made by a careful mixing of cement, sand, gravel, and water, in addition to other aggregates, such as accelerants and retardant additives, which allows concrete to take several shapes and dimensions as the structure needs. Most of the concrete mixture consists of fine and coarse aggregates, sand, and gravel, respectively. Cement and water interact chemically bounding the aggregates particles into a solid mass. Concrete has several properties which can vary changing its component proportions appropriately. Concrete possesses excellent resistance to water. Unlike wood and ordinary steel, the ability of concrete to withstand the action of water without serious deterioration makes it an ideal material for building structures to control, store, and transport water. One of the first known concrete applications in structure members is the construction of retaining walls and aqueducts in Ancient Rome (Mehta and Monteiro, 2006).

Main concrete properties depend mostly on the adequate proportions of its main components, the form in which its constituents material blends together, and on environmental conditions such as humidity and temperature in which the mixture is stored from the moment

it is placed in the forms until it is fully hardened. This last process mentioned is called curing.

The factors that make concrete a universal building material are so pronounced that is has been used, in more primitive kinds and ways than at present, for thousands of years, starting with lime mortars (cement mixed with fine aggregates) from 12,000 to 6,000 BCE in Crete, Cyprus, Greece, and the Middle East (Nilson et al., 2010). The facility with which, while plastic, it can be poured and made to fill forms or molds of almost any practical shape is one of these factors. Its primary constitutive material such as sand, gravel, and water is usually available at low cost locally or at a short distance from the construction site. Concrete has a high compression strength, which makes it suitable for casting members subjected primarily to compressions, such as columns and arches. On the other hand, because concrete is a mixture of fine and coarse particles, it is a relatively brittle material whose tensile strength is small compared with its compressive strength.

Most structural elements exposed to moisture, such as foundations, footings, piles, beams, and columns, are frequently built with reinforced concrete. Concrete is commonly reinforced with steel bars to work together with concrete to support tensile strength. This material mixture is SRC. Some considerations that favor the use of SRC over other construction material of choice are:

- Fire resistance: this characteristic is perhaps the most important safety aspect. Since an adequate concrete cover on the reinforcement steel bar is required for structural integrity.
- Maintenance: Concrete does not corrode, does not require surface treatment, and its strength increase with time.
- Water resistance: Concrete does not decrease its strength in contact with water.

Due to SRC's importance as a construction material, numerous research has been made aiming to measure both the response and properties variation quantitatively, appropriately varying the admixture proportion and the additives.

2.1.2. Fibers as reinforcement

The use of fibers to strengthen materials with brittle conditions goes back to ancient times. Approximately 3,500 years ago, sun-baked bricks reinforced with straw were used to build the fifty-seven meters high hill of *Aqar Quf* and, at the same time, improving its response (Bentur and Mindess, 2007). Table 2.1 shows the mechanical properties of some fibers used in FRC, extracted from Bentur and Mindess (2007).

Table 2.1: Typical properties of fibers (Bentur and Mindess, 2007).

Fiber	Diameter (μm*)	Specific gravity	Modulus of elasticity (GPa)	Tensile strength (GPa)	Elongation at break (%)
Steel	5–500	7.84	200	0.5-2.0	0.5-3.5
Glass	9–15	2.6	70–80	2-4	2-3.5
Asbestos					
Crocidolite	0.02–0.4	3.4	196	3.5	2.0-3.0
Chrysolite	0.02–0.4	2.6	164	3.1	2.0-3.0
Polypropylene	20–400	0.9–0.95	3.5–10	0.45-0.76	15-25
Aramid (kevlar)	10–12	1.44	63–120	2.3-3.5	2-4.5
Carbon (high strength)	8–9	1.6–1.7	230–380	2.5-4.0	0.5-1.5
Nylon	23–400	1.14	4.1–5.2	0.75-1.0	16.0-20.0
Cellulose	—	1.2	10	0.3-0.5	—
Acrylic	18	1.18	14–19.5	0.4-1.0	3
Polyethylene	25–1000	0.92–0.96	5	0.08-0.60	3-100
Wood fiber	—	1.5	71	0.9	—
Sisal	10–50	1.5	—	0.8	3.0
Cement matrix (for comparison)	—	1.5–2.5	10–45	0.003-0.007	0.02

*μm = 10^{-6} meter.

Since the first use of asbestos fibers, a wide variety of other types of fiber have been used combined with mortar to strengthen its brittle conditions: Steel fibers (Hoff, 1986; Brandt, 2008), carbon fiber (Jeon et al., 2015), glass fibers (Arslan, 2016), PVA fibers (Pan et al., 2015; Toutanji et al., 2010), natural fibers (Fiore et al., 2015) like coconut husk, sisal, and sugar cane bagasse.

The cost of steel fiber (Brandt, 2008) and durability are the main concerns in recognizing SFRC as a suitable material for the structural application (Khan and Ayub, 2016). These limitations of SFRC led to achieving ductility in the traditional concrete by using PVA fibers. The use of PVA fibers has an advantage over steel fibers in slip-hardening response (Holschemacher and Höer, 2008); it is durable against corrosion, it has a lower cost due to the lower density, and requires less cement/binder as compared to the same content volume of steel fibers. PVA fibers like steel and glass fibers are most promising in tensile strength, Young's modulus, and fiber elongation. In comparison to other synthetic fibers, it has been demonstrated that PVA fibers have a strong bond with the cement matrix compared to PP (Horikoshi et al., 2006) and found that the PVA fibers were ruptured whereas PP fibers were removed out the matrix (Horikoshi et al., 2006).

Due to these advantages, PVA fibers have been used commonly in ECC, which has a limited structural application to tensile members and thin sheets due to a lower toughness for the lack of coarse aggregates (Li et al., 1998).

In 2008, Holschemacher and Höer (2008) investigated the PVA-FRC with regular size aggregates under bending and single fiber pull-out test. It obtained that the use of PVA fiber is beneficial in terms of ductility and load-carrying capacity of structural concrete. Consequently, PVA fiber has the potential to be used in place of steel fibers.

2.2. PVA fiber reinforced concrete

PVA references to Polyvinyl-alcohol, which is the first synthetic colloid prepared by Herrmann & Haehnel in the year 1924. PVA is manufactured by polymerization of vinyl acetate monomer into polyvinyl acetate (PVAc), followed by hydrolysis of the acetate groups of PVAc to PVA (Thong et al., 2016). It is non-hazardous, and it is considered safe to handle and environmentally friendly. This fiber presents suitable characteristics as an FRC as it has high strength modulus and elastic modulus compared to other types of fibers, such as polypropylene fiber, nylon fiber, polyethylene fiber. The mechanical behavior of PVA-FRC can be influenced by different factors (i.e., fiber distribution, fiber length, fiber geometry, and orientation). Therefore, it is essential to follow a rigorous procedure in the specimens' confection process. PVA chemical nomenclature is C_2H_4O.

Many researchers proved that FRC improves the tensile behavior of concrete. Furthermore, with just a little percentage of fiber content within the matrix, the toughness increases, and on the other side, with a more considerable amount of fiber, the tensile strength also increases. The main effect of fiber in the concrete matrix has been noticed in the post-cracking zone, where fibers, work as a bridge across the fracture zone, so it is possible with a high amount of fiber content reaching a multiple-cracking stage of the cementitious element (Cotterell and Mai, 1995).

PVA is one of the major polymers used in the industry, and therefore massive amounts of PVA are produced yearly. Its lower cost compared to other fibers, about 1/8 of high-modulus PE fiber (Felekoglu et al., 2015), is one of the reasons for PVA fibers to be studied extensively as a more economical alternative.

Figure 2.1: Kuraray RF 4000 PVA fibers (Khan and Ayub, 2016).

Some investigations imply that PVA fiber content higher than 4% can develop an outstanding ductility reaching a strain-hardening state, in which, at high strains, the specimen can increase the lower-strain strength. Nonetheless, the higher PVA content inside the matrix produces some problems: workability decreasing, and extensive particle agglomerations.

PVA fiber has been limited investigated in matrices containing coarse aggregates. Thus, there is limited literature available related to the modeling, and consequently, its mechanical properties. Conversely, all the literature available, except few pieces of literature, studies the influence of PVA fibers in fine aggregate matrices, as ECC.

2.2.1. Pullout test

In order to study PVA fiber's real influence in the concrete matrix, it is essential to assess its interfacial bond properties. An excellent method to directly measure this is the pullout test. This test consists of pulling a single fiber out of its surrounding matrix.

According to Holschemacher and Höer (2008), PVA fiber in ECC shows a slip-hardening response. Therefore, it can be expected that all concrete mixes containing PVA fibers will exhibit a similar response when a pullout test is performed. Consequently, the PVA fiber bond strength is lesser than its rupture strength, allowing PVA fiber to have a slip-hardening response (Khan and Ayub, 2016). The general profile of a single fiber pullout curve can be decomposed into three major regimes. Initially, a stable fiber debonding process occurs along with the fiber/matrix interface Fig. 2.2. The load resisted by the fiber will increase up to Pa. The fiber embedded end le will not move. The debonded length ld will increase up to ld = le. The displacements can be found corresponding to the elastic stretching of the debonded fiber. After reaching Pa, the load will be decreased from Pa to Pb. This drop in the load shows that the bond between fibers and matrix vanishes.

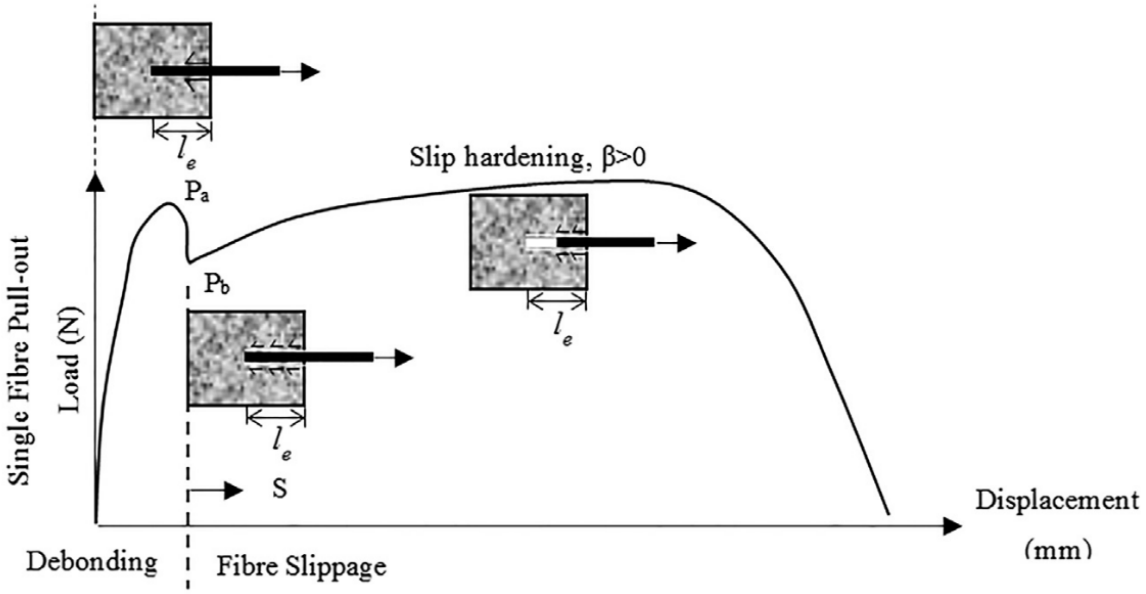

Figure 2.2: Profile of single fiber pullout response (Khan and Ayub, 2016).

Redon et al. (2002) performed an investigation with the objective of determining interfacial parametric values for use in micromechanical models of ECC, as well as extracting knowledge on fundamental processes governing the bridging behavior of PVA fibers in ECC. Two types of PVA fibers were tested, oiled and uncoated, with different dimensions and mechanical properties. Its investigation demonstrated that within certain restrictions, lowering the interfacial bond values can be achieved using an oil coating. Also, the oiling agent had very little influence on the slip-hardening effect.

2.2.2. Fiber's Distribution

Fiber dispersion uniformity inside an ECC matrix impacts the tensile strain-hardening behavior and magnitude of tensile stress capacity, which determines the fiber bridging strength, complementary energy, and degree of multiple-crack saturation. Li and Li (2013) investigated the dispersion of PVA fibers. It points out that the processing method such as mixer type, mixing speed, time and sequence, and mixing personnel's experience level can influence the rheological properties of the ECC mortar (ECC before adding fibers), which may strongly affect fiber dispersion uniformity, the size distribution of air voids in the cementitious matrix, and bonding properties at the fiber/matrix interface in the hardened state. Meanwhile, Felekoglu et al. (2015) provides that the relation between fiber bridging stress and crack width and, in particular, fiber bridging strength strongly depends on the fiber distribution characteristics. For a specimen subjected to uniaxial tension, poor fiber distribution will lead to a reduced effective fiber dosage at the 'weakest' cross-section within the specimen. An inappropriate effective fiber dosage will lead to a lower fiber bridging strength at the weakest section. Thus fiber bridging capacity exhausts earlier. If fiber distribution at the 'weakest' cross-section within the specimen is known, it is possible to check and assess the multiple cracking potentials of composites. Using the same ECC mixture is possible to change significantly the response of PVA-FRC (Fig. 2.3), in this case, each specimen were produced used a gravity mixer and with the same capacity.

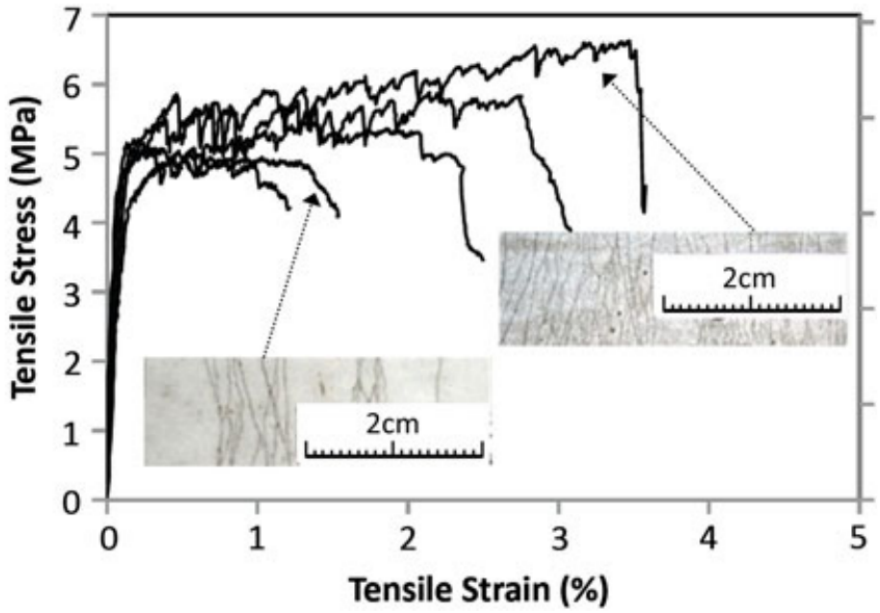

Figure 2.3: An extreme case of variation in tensile stress versus strain curves of ECC with same mix proportion (Li and Li, 2013).

2.2.3. Aggregate Size

Almost all the PVA investigations made along the years use ECC mixture as its matrix for FRC. Current ECCs are designed with a limited amount of very fine aggregates. Specifically, high aggregate content and the presence of coarse aggregates in a paste tend to increase the matrix toughness, which delays crack initiation and prevent steady-state flat-crack propagation, resulting in a loss of tensile ductility of ECC (Sahmaran et al., 2012). Moreover, Sahmaran et al. (2012) also points out that the introduction of larger particle size larger than the average fiber spacing leads to the balling of fibers and results in poor fiber dispersion uniformity. Average particle gradations and median diameters used in most FRC investigations with ECC are shown in Fig. 2.4.

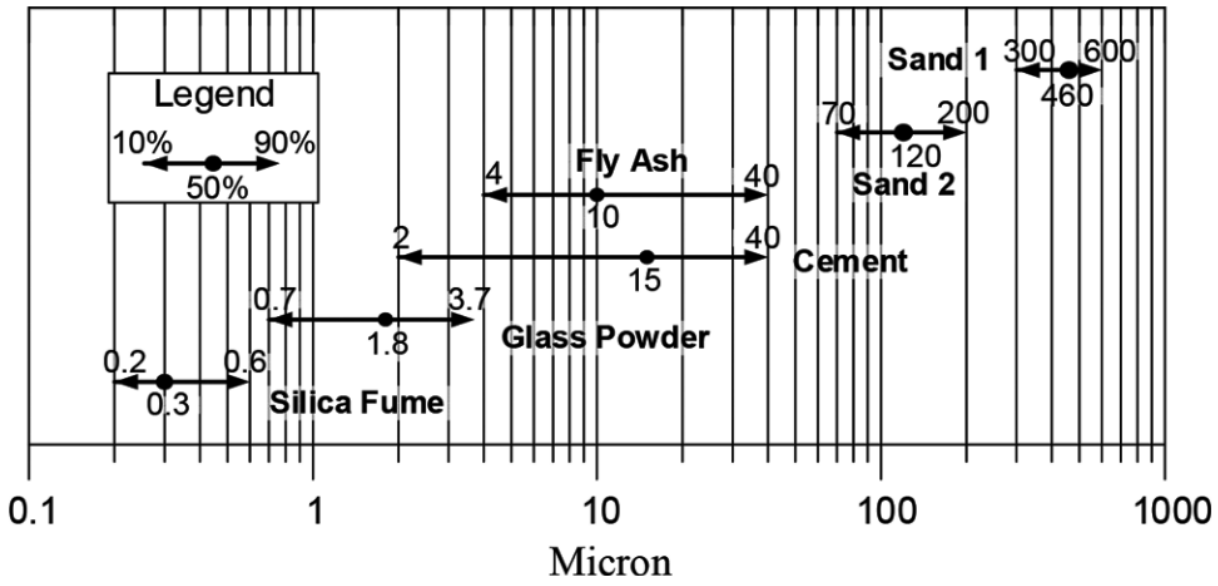

Figure 2.4: Particle gradation and median diameter of used materials (Aghdasi et al., 2016).

It is known, as mentioned before, that the higher the aggregate content, the higher is the matrix toughness. However, researchers recommend that the size of the aggregates be as small as possible (Sahmaran et al., 2012). Sahmaran et al. (2012) led a investigation noticing that PVA works great with fine size aggregate matrices, such as ECC, and mortar. Due to the bad interaction between the fiber and cementitious particles. The higher the particle size, the bigger the air void content inside the matrix and PVA tends to produce voids in the matrix, leading to diminishing the specimen strength.

Table 2.2: Aggregate Size summary.

Author	Maximum Aggregate Size
Mechtcherine et al. (2011a)	0.06 - 0.2 mm
Sahmaran et al. (2012)	0.4 - 1 mm
Li et al. (1998)	10 mm
Hossain et al. (2013)	10 mm
Khan and Ayub (2016)	10 – 20 mm
Holschemascher and Höer (2008)	16 mm
Ayub et al. (2019)	19 mm

Because of the many investigations developed using ECC mixture, it is imperative to assess the real PVA-FRC behavior using bigger aggregate size, as real structural members do. Table 2.2 summarizes the maximum aggregate size that some authors have used in its research, emphasizing the lack of investigation on coarse aggregate size mixtures.

2.2.4. Compressive Strength

To characterize the real behavior of PVA-FRC, it is mandatory to understand the compressive and tensile behavior. For many years, researchers have used ECC as a bonding matrix with PVA. The uniaxial compressive test is a standardized test that is used to obtain the complete compressive stress-strain relations and other related mechanical parameters, such as maximum compressive strength (f'$_c$), strain at the peak, maximum strain, and concrete Young's modulus. There are norms available for testing procedures, such as ASTM C39 (American Society of Testing and Materials., 2015), which covers the determination of the compressive strength of cylindrical concrete specimens with 1:2 ratios (diameter: length). This section will briefly cover the literature available to assess the compressive strength of PVA-FRC both, fine coarse aggregate (mortar and ECC) and the investigation developed by Khan and Ayub with coarse aggregate matrices.

Hossain et al. (2013) investigated the influence of PVA fiber on the SCC matrix, the results obtained are detailed in Table 2.4, in which the addition of PVA fiber did not improve or significantly diminished the compressive strength compared to the control mix. A maximum strength reduction of about 15% was observed for 0.5% volume PVA content.

Table 2.3: Mix used by Wang et al. (2020).

Mix No.	Composite cement	Water	Sand	Superplasticizer
M1	1.0	0.25	0.2	0.0150
M2	1.0	0.35	0.3	0.0075
M3	1.0	0.55	0.8	0.0

In 2020, Wang et al. published a work where hybrid-fiber-reinforced ECC were tested. Its main purpose was to investigate additional steel fiber's effect on the compressive behavior of traditional PVA-FRC with different mortar mixtures. Details are shown in Table 2.3. However, for this investigation concern, Wang et al. compares plain concrete's response with different matrix strength to 1.7% PVA-FRC matrices. Fig. 2.5 (a) - (c) show the results obtained by doing a compressive strength testing on PVA-FRC cylindrical specimens to mixtures M1 - M3, respectively. The results obtained by Wang et al. also shows that the addition of PVA fiber did not improve nor significantly diminished the compressive strength.

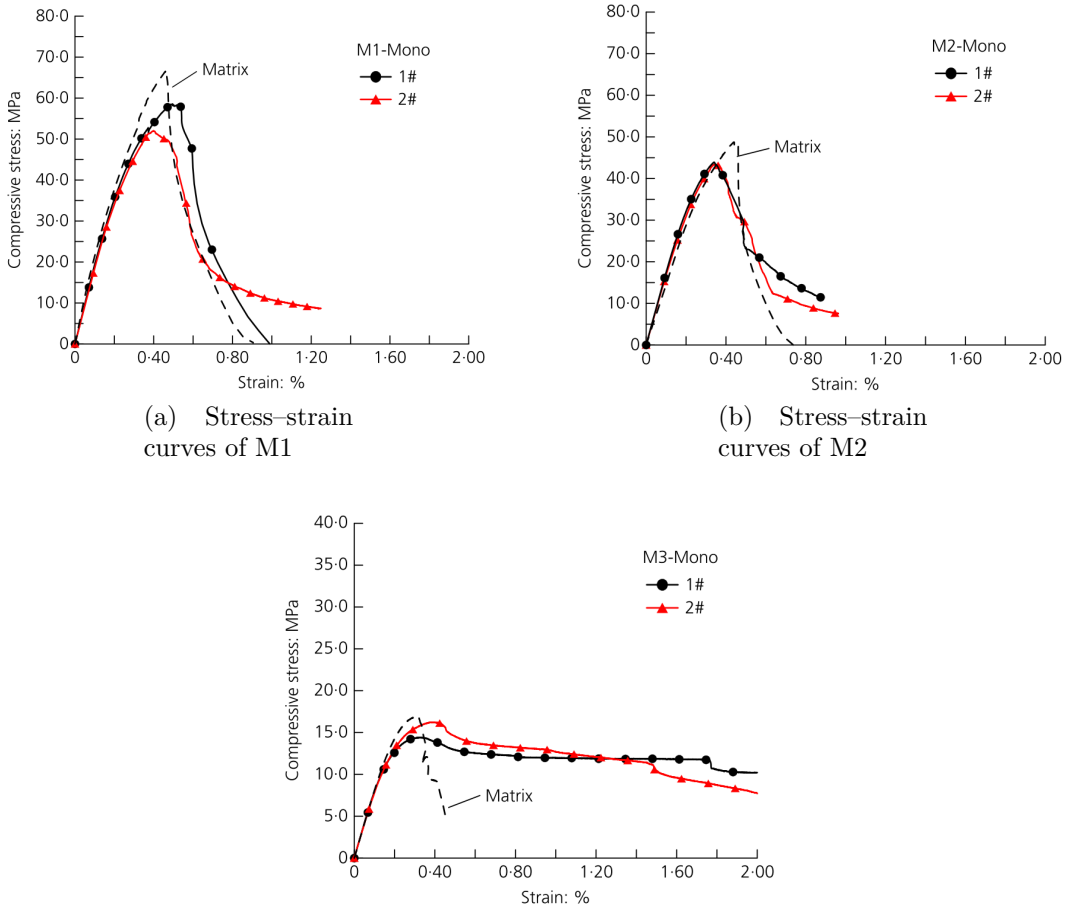

(a) Stress–strain curves of M1

(b) Stress–strain curves of M2

(c) Stress–strain curves of M3

Figure 2.5: Comparison of uniaxial compressive stress–strain relations of PVA-FRC with different matrix's strengths (Wang et al., 2020).

Dashed lines in Fig. 2.5, represents the stress-strain curves of each no-fiber-content matrix. The stress-strain curves shown can be divided into two stages: an ascending stage up to the peak stress and a subsequent descending stage further called a residual strength stage. On the first stage, the stress-strain curves behave elastically up to the end of the initial linear segment, approximately 60% of peak compressive strength, after which the curves deviate from linear behavior and change to a non-linear behavior until the peak stress f'_c (i.e., compressive strength). When the descending stage is concerned, the no-fiber-content concrete falls suddenly after the peak point, showing apparent brittle failure. However, the fiber-reinforced mixtures drop slightly with increasing strain after the maximum stress due to the confinement effect by fiber bridging, shown in Fig. 2.6.

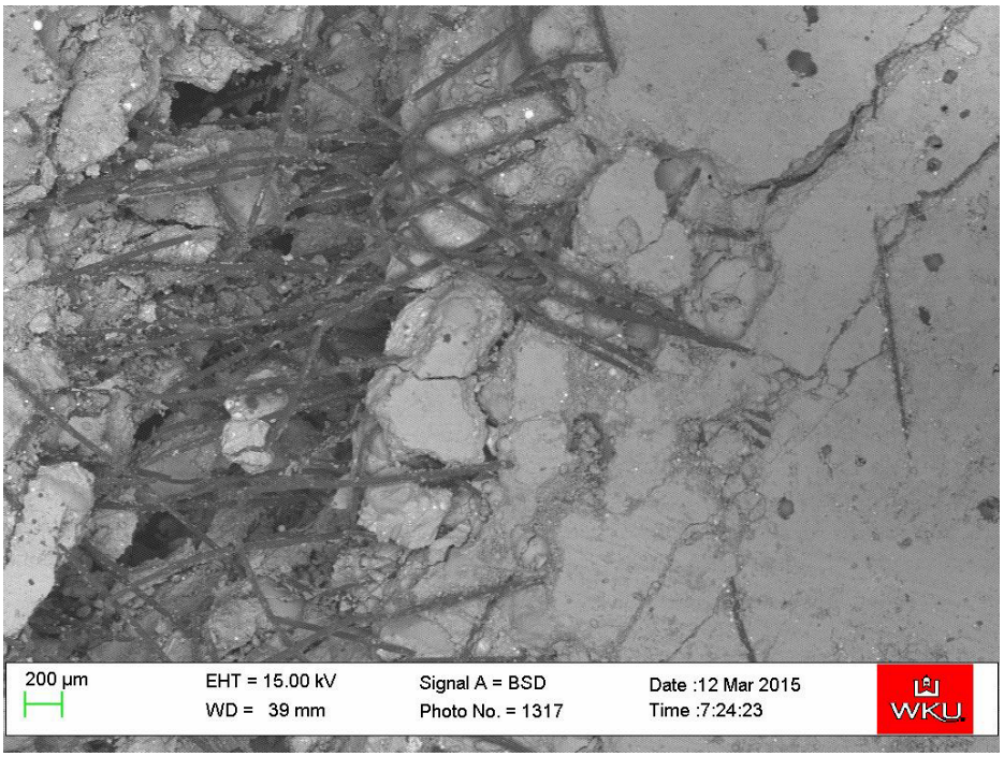

Figure 2.6: Fiber crack bridging effect (Annam, 2015).

There are few researching projects of FRC with coarse aggregates containing PVA fibers, as the work developed by Khan and Ayub in the year 2016. Its main objective was to assess the direct tensile response of FRC with coarse aggregate content and PVA with 30 mm length, and then develop a model validated with experimental testing. Three cylinders of the size 100 x 200 mm were cast for compressive testing, and PVA fiber was added as 0, 1, 2, and 3% by volume (i.e., P0, P1, P2, and P3, respectively) to the concrete mix. The compressive strength of each specimen is shown in Fig. 2.7 and the strain at peak stress along with the maximum stress plotted in Fig. 2.8.

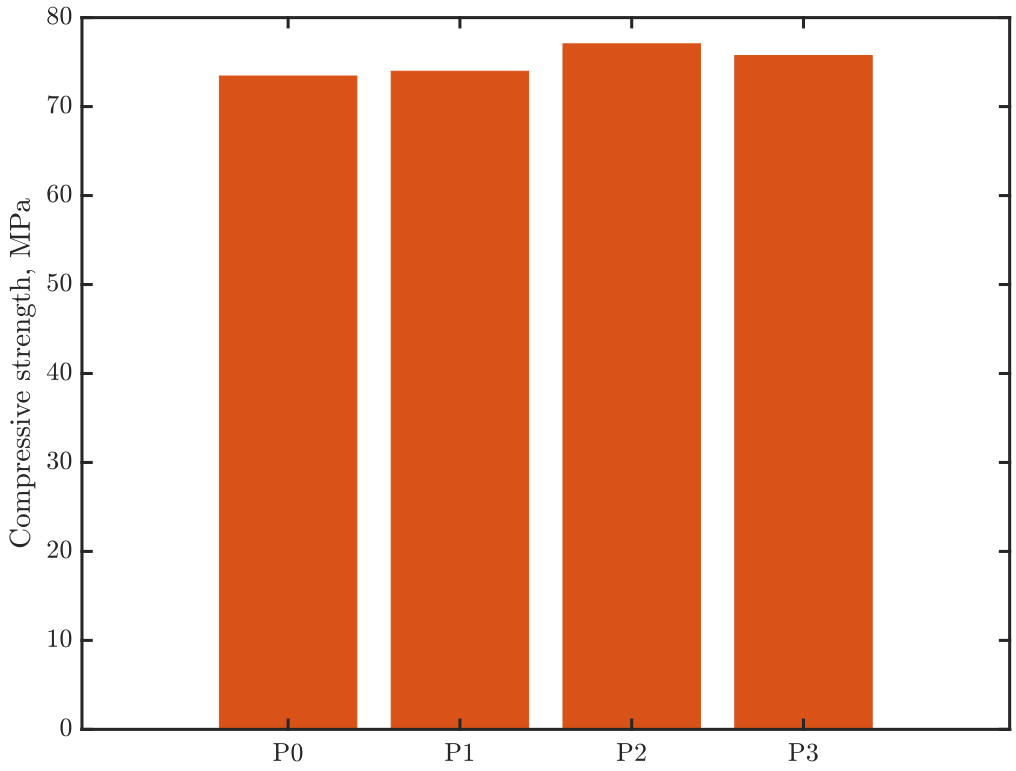

Figure 2.7: Compression test results of specimens tested by Khan and Ayub (2016) at 28 days.

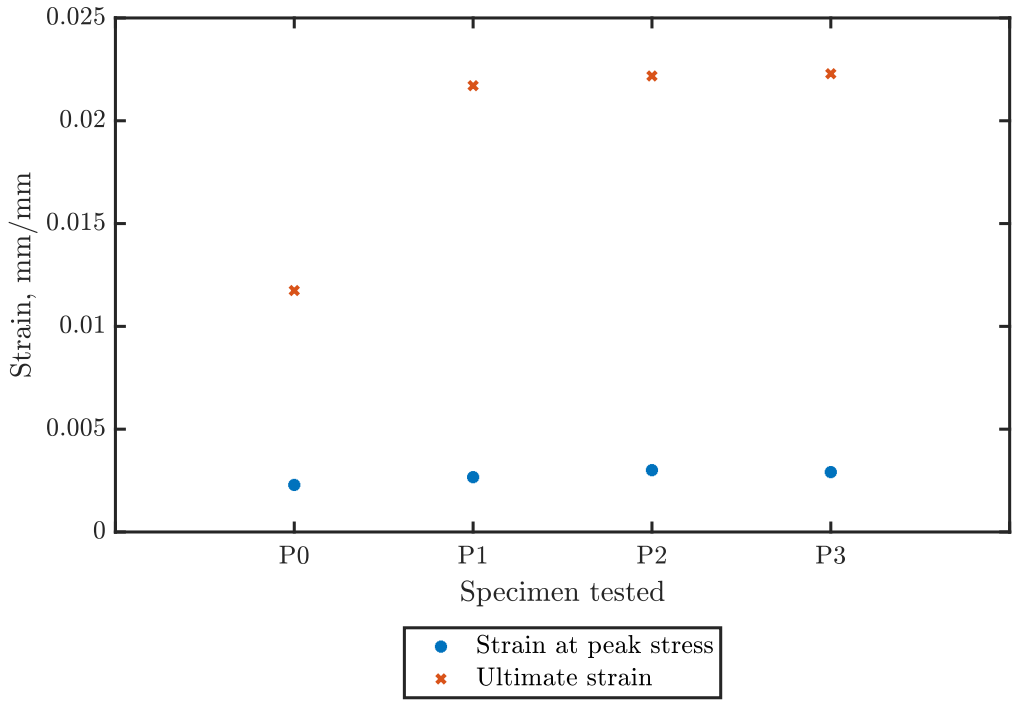

Figure 2.8: Strain at maximum stress peak and ultimate strain of specimens tested by Khan and Ayub (2016) at 28 days..

Following the same investigation line, Ayub, along with Khan in the year 2019, developed

a complete analytical model for compressive FRC containing the maximum size of coarse aggregate of 19 mm and reinforced with 1–3 % PVA fiber volume. The PVA fiber used in this investigation was Kuraray RF4000, with a length of 30 mm. As they did in the previously mentioned investigation (Khan and Ayub, 2016), three mixes of FRC designated as Mix 'P', Mix 'S', and Mix 'M' were prepared to obtain the compressive strength. The first mix 'P' was prepared by using 100% cement, the other two Mixes 'M' and 'S' replaced 10% of cement with Malaysian metakaolin and silica fume, respectively. For this investigation, the results obtained in the 'P' series are the important. The results of the compressive strength of PVA-FRC was obtained by testing cylinders of size 100 x 200 mm; the curves are shown in Fig. 2.9. It is worth noticing that the addition of PVA fibers in the mixture increases the strain at peak and the residual strain compared to the no-fiber-content specimen without decreasing the peak compressive strength significantly.

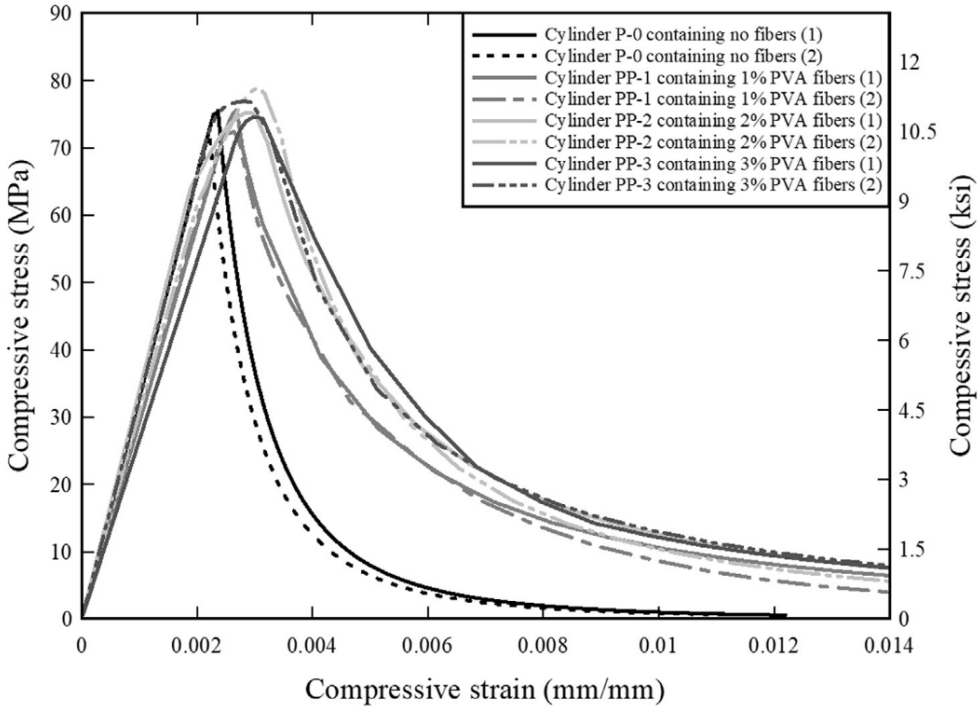

Figure 2.9: Experimental stress–strain curves of PVA-FRC of Series 'P' (Ayub et al., 2019).

2.2.5. Tensile Strength

Concrete is mainly known for its compressive strength capacity. As explained in the previous section, concrete with PVA fiber reduces its concrete capacity compared to a no PVA concrete specimen. However, PVA fiber has an incredible impact on the tensile strength of the concrete specimen; moreover, the fiber acts as a 'bridge' inside the crack, incrementing the strain capacity along with a lower increment of the tensile strength on high deformation stages. Assessing the tensile strength of concrete has not been intensely studied for the scientific community's low interest to know the concrete tensile capacity. Nevertheless, the academy uses two types of experimental setups to assess the tensile capacity of concrete: a direct tensile test using dogbone and cylindrical shape specimens, and an indirect tensile test

or splitting tensile test (American Society of Testing and Materials., 2011) with cylindrical shape specimens—more details on the following sections.

2.2.5.1. Indirect Tensile Test

Splitting test or Brazilian tensile test or indirect tensile test method are the common names that refer to this test. The correct test execution guidelines are given in the ASTM standard 'Splitting Tensile Strength of Cylindrical Concrete Specimens' (American Society of Testing and Materials., 2011). This method consists of applying a compressive force along the cylindrical shape concrete specimen's length until failure occurs along the two opposing diametral planes. This loading induces and indirect tensile stress on the transversal plane of which the compressive force is applied. The tensile failure occurs in the transversal plane rather than a compressive failure because the load application areas are in a state of triaxial compression.

This method is commonly used to measure concrete tensile strength due to its simplicity and applicability to freshly cylindrical shape concrete specimens or core examples of hardened concrete extracted by drilling. The load is applied to two small contact arcs across 1.5 mm thick cardboard or wood strips as shown in Fig. 2.10. The main purpose of these wood strips is to distribute the load and prevent the local concentration of stresses due to geometric irregularities in the specimen's surface.

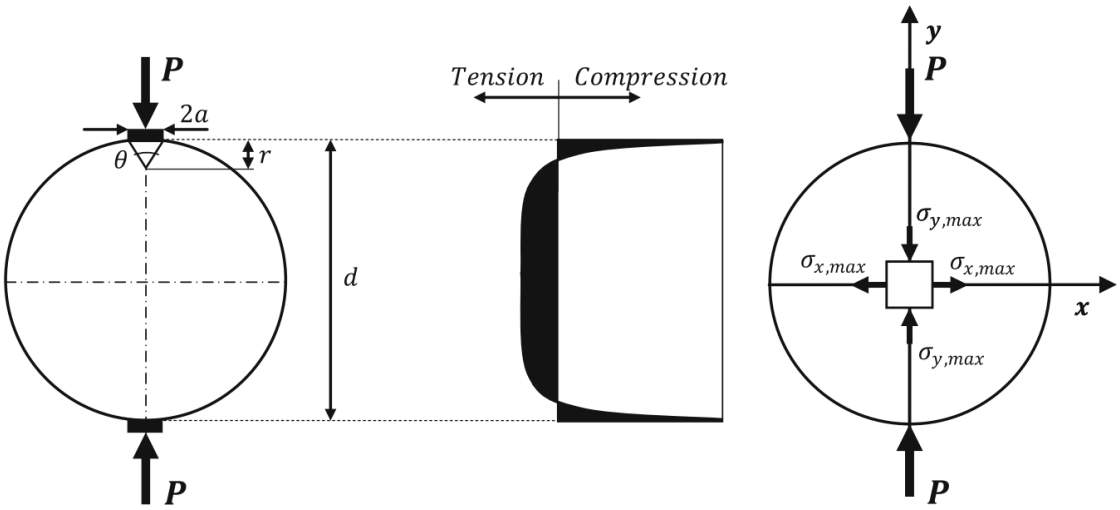

Figure 2.10: Parameters used for determining the stresses in a cylinder subjected to diametral compression; Distribution of horizontal stresses (σ_x) in the loading plane and point of maximum stresses produced by the loads concentrated on two diametrically opposite generatrices (Carmona and Aguado, 2012).

Many researchers have used this testing setup to assess the tensile strength capacity and residual strength of PVA-FRC. Hamoush et al. led an investigation in 2010, which assessed the influence in the tensile response of specimens made from concrete with PVA micro-fibers PVA content used on that research was 3% volume of cement. The average strain values were determined from the data collected from both sides of the tested discs. Three discs of each combination were tested, and the resulted averages are plotted and shown in Fig. 2.11. The

results showed that when concrete is in tension, the stress-strain relationship is linear up to the tensile strength, then it dropped abruptly to failure. On the other hand, the measured tensile stress-strain relation of the microfiber reinforced concrete specimens show remarkable strain capacity (over 0.65%) and peak crack-bridging stress of about 3.79 MPa (550 psi).

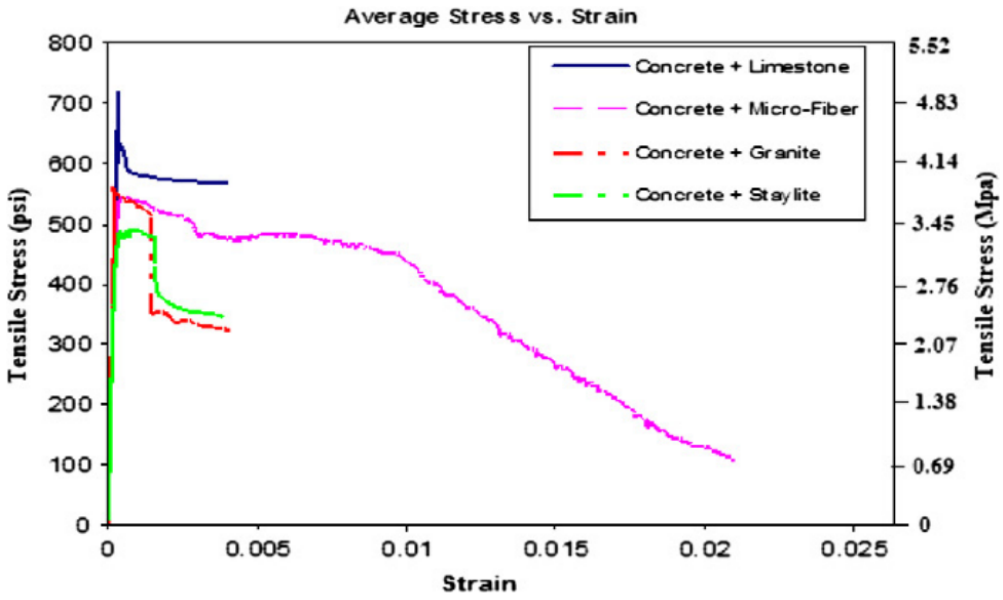

Figure 2.11: Stress–strain under tension obtained by Hamoush et al. (2010).

Meanwhile, Hossain et al. (2013) investigated the influence of different types of fibers, among which is PVA fiber, on Self-Consolidating Concrete (SCC). SCC is a high-performance concrete placed and compacted under its weight with little or no vibration effort. In what PVA fiber concerns, the researcher developed nine types of PVA-SCC mixtures from 0% volume content to 0.5% content. The results of both the compressive and splitting tests are tabulated in Table 2.4 and the visualization of the mixtures which al three tests were performed are shown in Fig. 2.12.

Table 2.4: Hardened properties of PVA concrete mixtures performed by Hossain et al. (2013).

Mix no.	Mix designation	Comp. strength 14 days (MPa)	Comp. strength 28 days (MPa)	Splitting strength 28 days (MPa)
1	0Fiber	38	44	2.7
2	0.05PVA	35	38	3.0
3	0.07PVA	34	37	n.p.
4	0.1PVA	n.p.	n.p.	n.p.
5	0.125PVA	32	38	3.9
6	0.15PVA	35	42	n.p.
7	0.2PVA	n.p.	41	3.6
8	0.3PVA	36	40	n.p.
9	0.5PVA	37	46	n.p.

*n.p.: not performed.

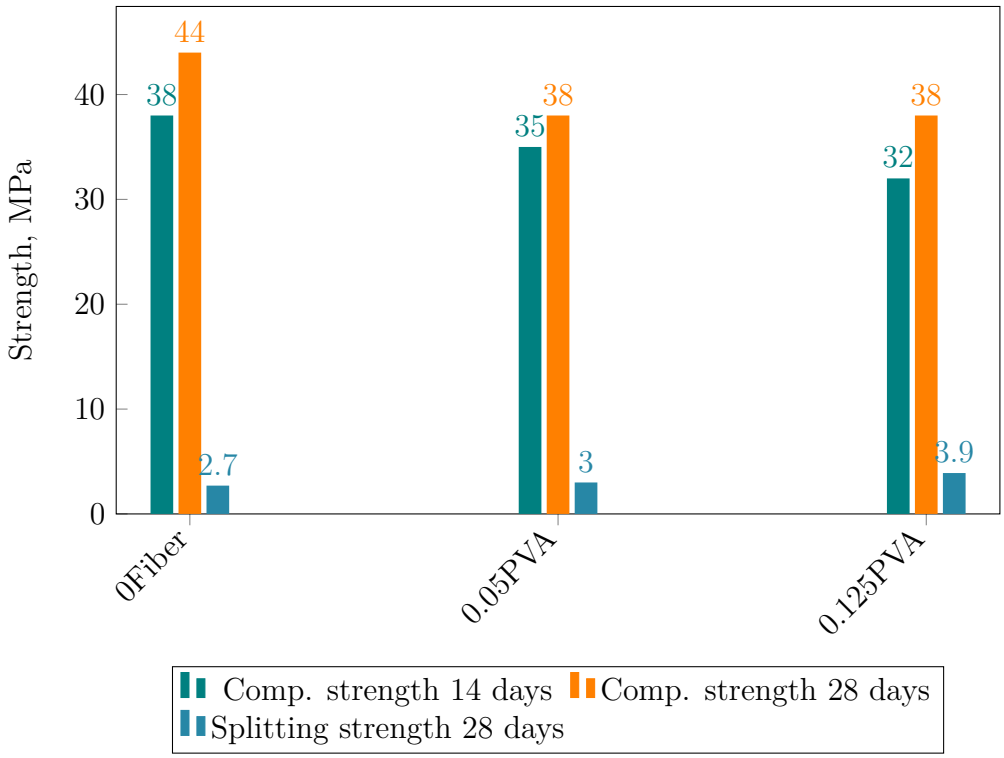

Figure 2.12: Data of Table 2.4 of splitting tests performed.

The tensile splitting methodology for FRC provides a relatively simple alternative to the more complex direct tensile testing approach. Direct tensile testing yields more detail on the post cracking behavior of the composite material. However, if only a measure of the tensile strength is required, for instance as an input to fracture mechanics models, the tensile splitting methodology will suffice.

2.2.5.2. Direct Tensile Test

Studies have shown that the direct tensile testing method is the most reliable way to assess the concrete tensile strength than splitting tensile and flexural testing methods (Swaddiwudhipong et al., 2003; Choi et al., 2014). Nonetheless, it is a difficult test to perform in the laboratory due to the bonding material used to glue the specimen to the testing machine, and also, the torsion plane generated while the testing machine accommodates the eccentrical loading. The author of this investigation could not found a reliable procedure to perform a direct tensile test in the laboratory. However, many researchers have used standard procedures such as dogbone and cylindrical shaped specimens. Nevertheless, the concrete tensile strength and residual strength are sensitive to the loading rate and cross-section dimensions, and those are the main factors in which many researchers have different responses. More on that will be discussed in the following section.

The testing procedure consists of attaching the specimen by gluing it to the tensile testing machine on both sides and then and extended to rupture, as shown in Fig. 2.13. Force is measured at the testing machine by a load cell, and the specimen elongation is assessed by strain gauges or Linear variable differential transformers (LVDTs) where this last measures displacement but knowing the initial gap is simple to obtain the strain by just dividing the displacement by the initial gap.

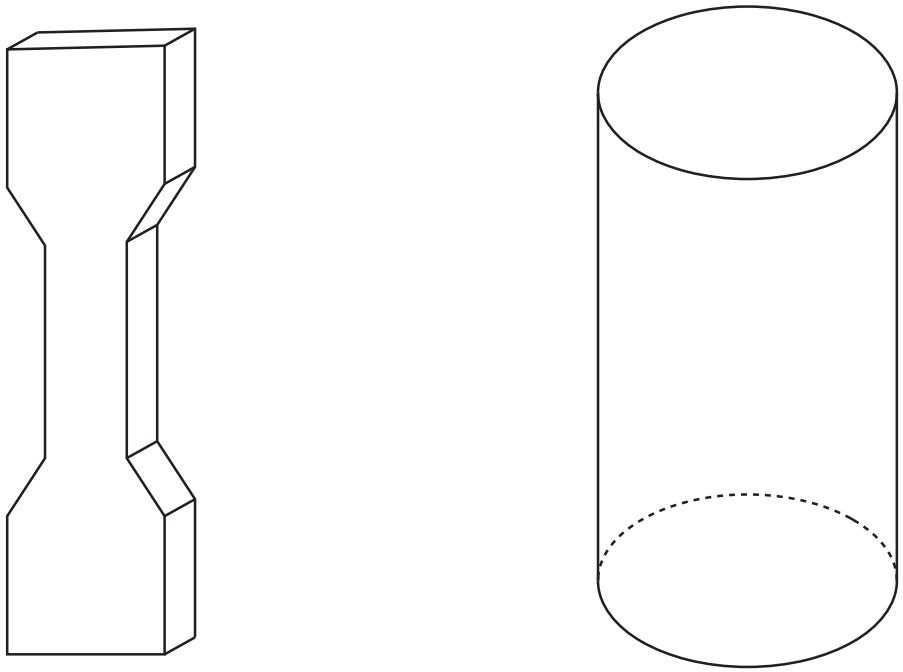

(a) Dogbone specimen (b) Cylindrical specimen

Figure 2.13: Shapes commonly used for direct tensile tests (not a scale).

As mentioned earlier, the concrete tensile strength and residual strength are sensitive to

the loading rate. Mechtcherine et al. (2011a) studied the behavior of SHCC (i.e., Fiber Reinforced ECC) subjected to low and high strain rates. Thus, the direct tensile testing of dogbone specimens was performed at velocities of 0.1, 2, and 180 mm/min, respectively. Associated with these velocities, the specimens with the gauge length of 2mm have strain rates of $8.3 \cdot 10^{-4}$, $1.7 \cdot 10^{-2}$, and 1.5 s^{-1}, respectively. Consequently, Mechtcherine et al. (2011a) showed that at higher strain rates, higher the stress capacity, but lower the capacity. On the other hand, from Fig. 2.14 it is possible to conclude that increasing the strain rate increases the peak stress, but the residual capacity decreases at a lower strain compared with a lower strain rate test. The strain hardening phenomenon of PVA-ECC specimen after the initial cracking was much significant at strain rates of 25 s^{-1} and 50 s^{-1} but with only one crack.

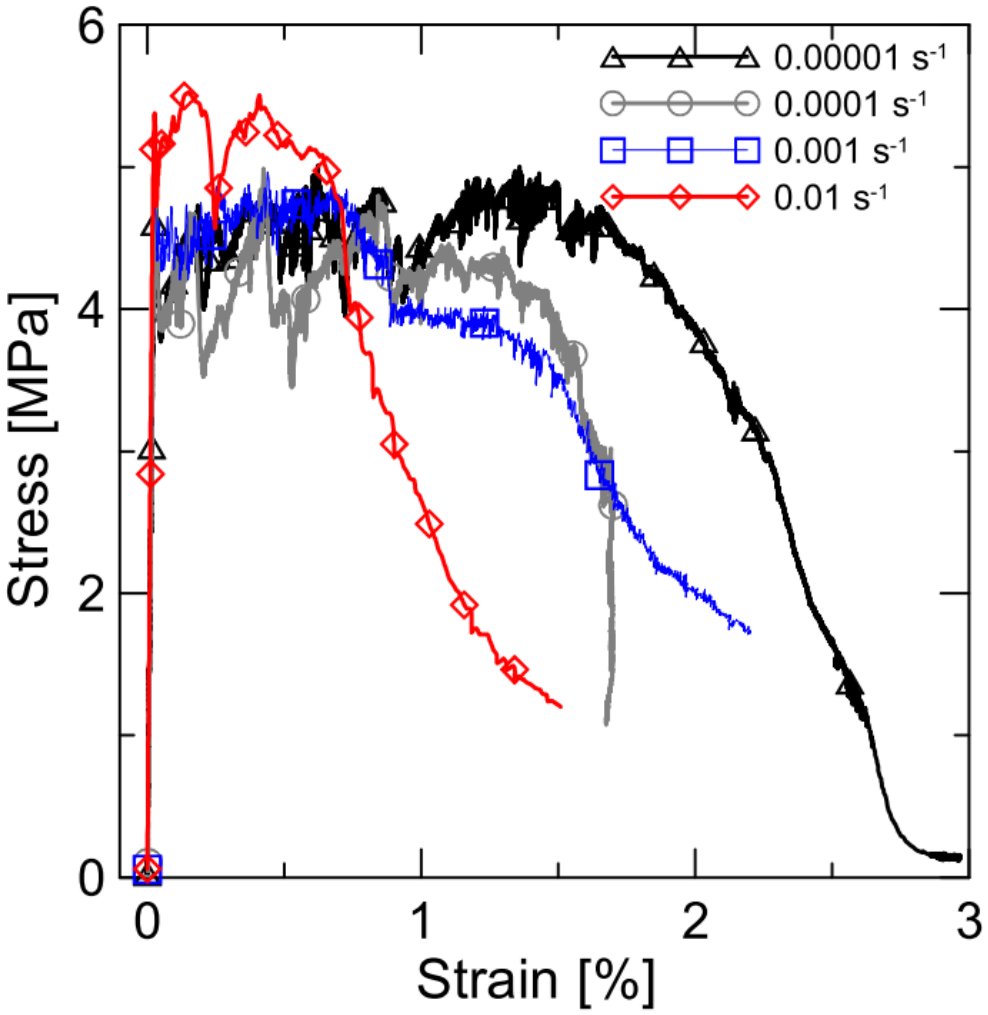

Figure 2.14: Tensile stress-strain responses of SHCC (Mechtcherine et al., 2011a).

Khan and Ayub (2016) in its investigation, apart of the compressive test (Fig. 2.7) also performed direct tensile testing of specimens with a cross-section area of 70 x 70 mm, as shown in Fig. 2.16. It is noticeable that the strain capacity with PVA FRC can reach up to 1%, shown in Fig. 2.15, and the stress capacity is approximately 10% f'$_c$.

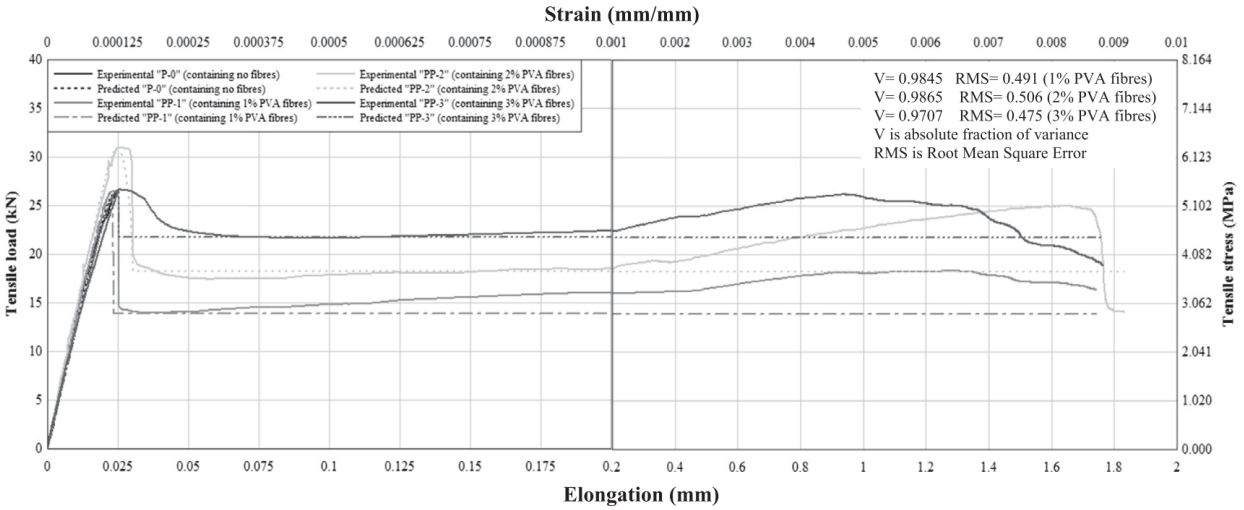

Figure 2.15: Experimental tensile stress-strain and load-elongation curves of concrete of series 'P' containing PVA fiber (Khan and Ayub, 2016).

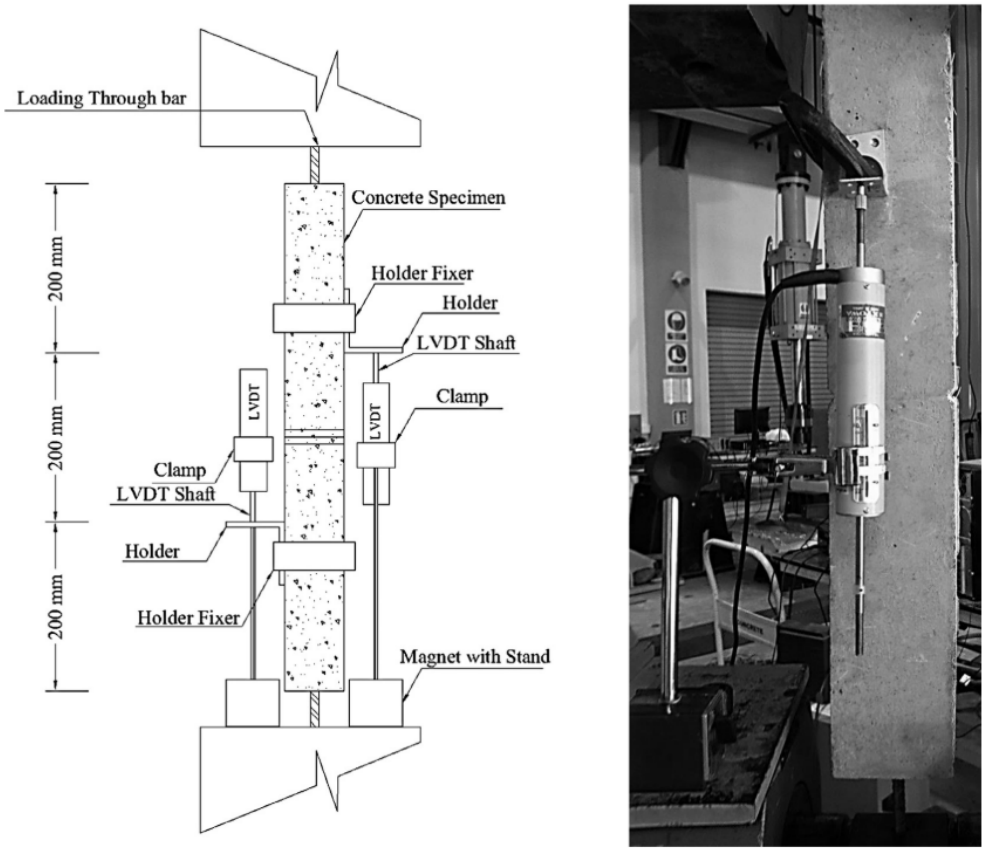

Figure 2.16: Dimension of specimen, gauge length and testing arrangement (Khan and Ayub, 2016).

Specimen Shape Response

The following section resumes the work developed by Yu et al. in 2018, where summarizes the essential information of factors that influence the tensile properties of ECC, focusing for our investigation in the specimen geometry and size, and strain rates.

Yu et al. (2018) studied the influence of the fiber reinforcing index, which its denominated as $V_f L_f / d_f$ on the tensile property. V_f is the fiber volume fraction, L_f is the fiber length, and d_f is the fiber diameter. It concluded that the tensile properties increased while the crack spacing and crack width decreased significantly with increasing the fiber reinforcing index.

Geometry has a notable influence on the tensile property of PVA-ECC. The comparison of the typical tensile response of both geometries is shown in Fig. 2.17. The peak tensile strength and strain capacity of cylindrical specimens were lower than those of dogbone specimens. This response difference can be attributed to three factors: the geometry-induced difference in tensile properties, i.e., the variations in initial imperfections (such as air voids and shrinkage cracks), fiber dispersion, and alignment; and the border conditions (Yu et al., 2018).

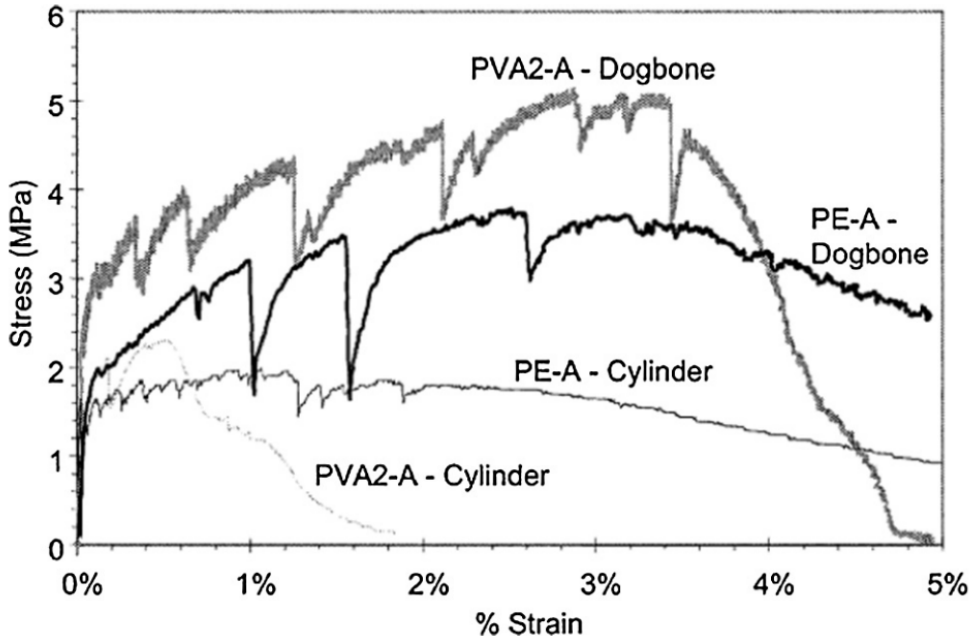

Figure 2.17: Tensile response of specimens with different geometries (Yu et al., 2018).

Mechtcherine et al. (2011b) also mentioned that the tensile ductility of cylindrical specimens with a diameter of 75 mm was smaller than that of the dogbone shaped specimens with a cross section of 24 x 40 mm. It is remarkable that even a notch in the cylindrical specimen change its tensile behavior as shown in Fig. 2.18.

Summarizing the work developed by Yu et al. (2018) and Mechtcherine et al. (2011b): First, fiber properties have a decisive effect on the tensile performance of ECC; second, the size and geometry significantly change the tensile response; and third, high loading rate leads to a noticeable change in the tensile properties of ECC.

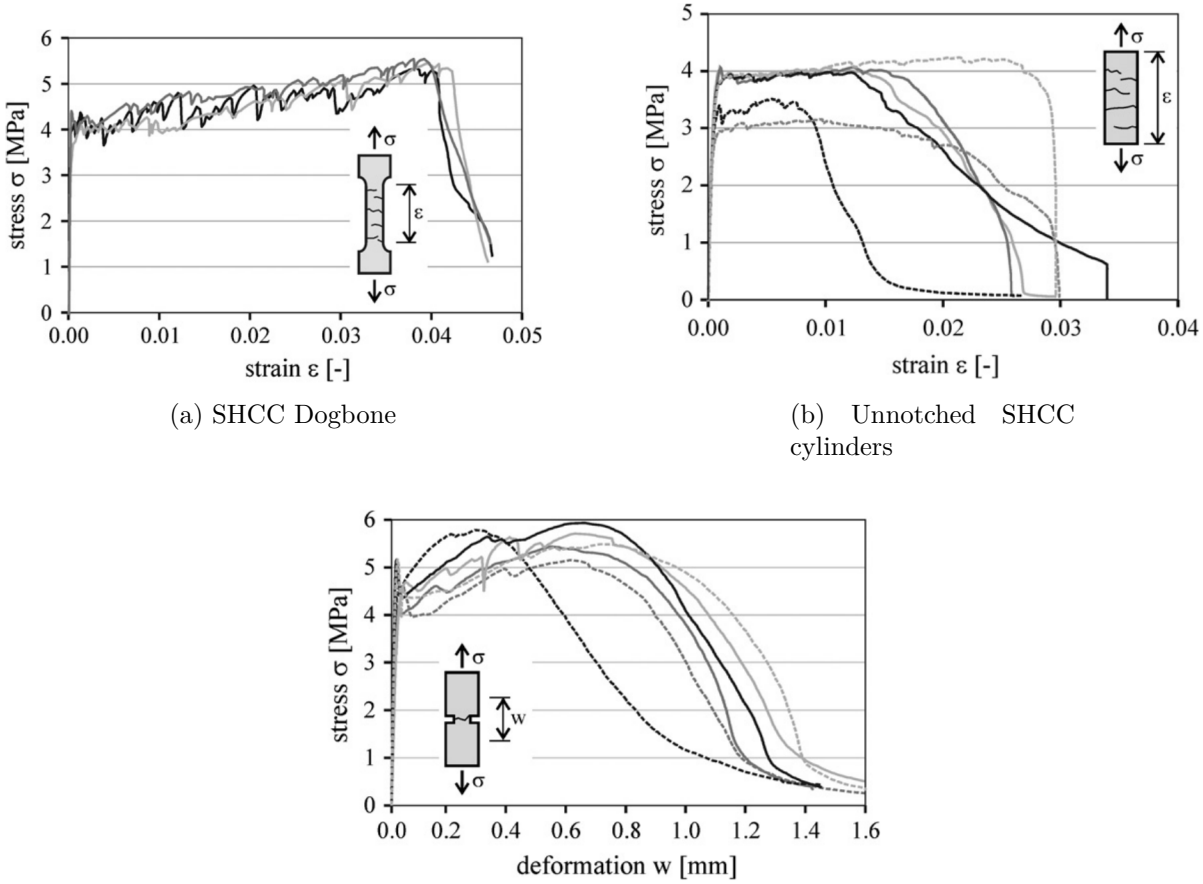

(a) SHCC Dogbone

(b) Unnotched SHCC cylinders

(c) Notched SHCC cylinders

Figure 2.18: Differences of stress-deformation curves obtained from uniaxial tension tests from three different specimens (Mechtcherine et al., 2011a).

2.3. Water-cement ratio

Water-to-cement (w/c) ratio is especially important in the concrete mix design. Abrams' law states that "the strength of a concrete mix is inversely related to the mass ratio of water-to-cement" (Sear et al., 1996).

Allahverdi et al. (2010) confirms the important role of w/c-ratio on the effectiveness of the polymer, so that relatively low w/c ratios can even provide inverse effect, as shown in Fig. 2.19. Its research varied the w/c ratio from 0.28 to 0.32. The lower w/c ratio of 0.28, the addition of polymer not only does not improve flexural strength but also slightly decreases the flexural strength. Increasing the w/c ratio from 0.28 to 0.30 resulted in significant improvement in flexural strengths, especially at p/c ratios around 0.016.

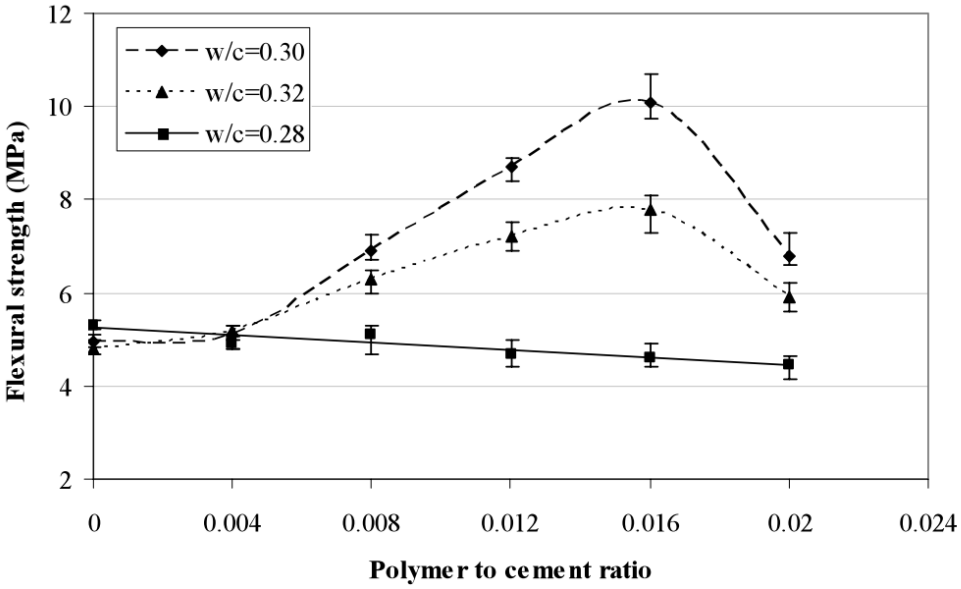

Figure 2.19: Flexural strength of cement pastes modified by polyvinyl alcohol at different w/c and polymer-to-cement ratios (Allahverdi et al., 2010).

Sasmal and Avinash studied the response of flexural PVA members when the water-cement ratio is varied from 0.3 to 0.4. It concluded that flexural strength increases with PVA fiber, but higher flexural strength does not automatically enhance ductility. This is understood from the results where specimens with a higher water to cement ratio (0.4) showed better post-peak behavior than 0.35 and 0.3 w/c, but the flexural strength was lesser for 0.4 w/c from 0.35 and 0.3 (Sasmal and Avinash, 2016).

2.4. 2D Digital Image Correlation

A non-contact technique to measure material deformation is Digital Image Correlation (DIC). DIC uses image registration algorithms to track the relative displacements of materials points between a reference image and a current image (undeformed and deformed image, respectively), as explain by Blaber et al. (2015). Ncorr is an open-sourced code developed by Blaber et al. (2015), which performs DIC analysis extracting displacement and strain data using nonlinear optimization methods, multithreaded computation analysis, and the ability to process large-deformations images.

Ncorr allows the user to set the analysis area of all pictures, reduce the number of analysis points by using what the author calls "Subset Radius," which groups pixels inside the radius and performs the analysis as a whole point, in order to reduce the computational load. The software programmed in MATLAB® determines the relative position of each point, using the Inverse Compositional Gauss-Newton (ICGN) method as the nonlinear correlation coefficient optimizer. Then, to estimate the strain field, Ncorr uses the Green-Lagrange strains, which are obtained by using the four displacement gradients Eq. 2.1 - 2.3.

$$E_{xx} = \frac{1}{2}\left(2\frac{\partial u}{\partial x} + \left(\frac{\partial u}{\partial x}\right)^2 + \left(\frac{\partial v}{\partial x}\right)^2\right) \tag{2.1}$$

$$E_{xy} = \frac{1}{2}\left(\frac{\partial u}{\partial y} + \frac{\partial v}{\partial x} + \frac{\partial u \partial u}{\partial x \partial y} + \frac{\partial v \partial v}{\partial x \partial y}\right) \tag{2.2}$$

$$E_{yy} = \frac{1}{2}\left(2\frac{\partial v}{\partial y} + \left(\frac{\partial u}{\partial y}\right)^2 + \left(\frac{\partial v}{\partial y}\right)^2\right) \tag{2.3}$$

The steps followed to perform the analysis are described in Appendix B. At the end, it is possible to obtain the displacement and strain fields at any correlatively image, and noticing the strain distribution variation.

Chapter 3

Analytical Model

This chapter will go through the analytical model's details, such as material calibration and the interaction model used. The computational model was developed using OpenSees software and the materials available in its library. Chapter 5 will apply the concepts explained in the following Chapter to calibrate and run the computational model.

3.1. Materials

Materials properties vary depending on the location inside the section and the addition of fiber into the mixture. The following section explains the materials used to perform the analysis and the assumptions taken to include the material's properties variation inside the section to assess those changes.

3.1.1. Concrete

PVA fiber addition into the mixture changes concrete's mechanical properties, as shown in the Literature Review. It may increase its strain capacity and slightly decrease the compressive strength. Concrete also changes its properties by being inside the stirrups due to the expansion restriction that stirrups do. To assess that behavior, the model included both cases, the unconfined and confined concrete. This last one was obtained using Saatcioglu and Razvi (1992) expressions.

3.1.1.1. Unconfined concrete

The tensile concrete backbone curve is obtained by the investigation developed by Belarbi and Hsu (1994), which is to determine the constitutive laws of concrete in tension. To achieve that, Belarbi and Hsu tested seventeen reinforced concrete panels under pure tension. Those panes were reinforced with steel bars in the direction of the applied tensile stress. The completion of the tests resulted in a calibrated expression to represent the concrete tensile response Eq. 3.1, where the expression is separate into two, the linear represents the pre-cracking stage and the second the post-cracking stage, f_{cr} (Eq. 3.2) and ε_{cr} (Eq. 3.3) are the peak concrete tensile stress and the strain at peak stress, respectively. Finally, β (Eq. 3.4) is a parameter which controls the residual stress at high strains. Fig. 3.1 shows the stress-strain curve proposed by using Belarbi and Hsu expressions.

$$\sigma_c(\varepsilon_c) = \begin{cases} \frac{f_{cr}}{\varepsilon_{cr}}\varepsilon_c & \text{if } 0 \leq \varepsilon_c \leq \varepsilon_{cr} \\ f_{cr}(\frac{\varepsilon_{cr}}{\varepsilon_c})^{\beta} & \text{if } \varepsilon_{cr} \leq \varepsilon_c \end{cases} \tag{3.1}$$

$$f_{cr} = 0.08 f'_c \tag{3.2}$$

$$\varepsilon_{cr} = 0.00008 \tag{3.3}$$

$$\beta = 0.4 \tag{3.4}$$

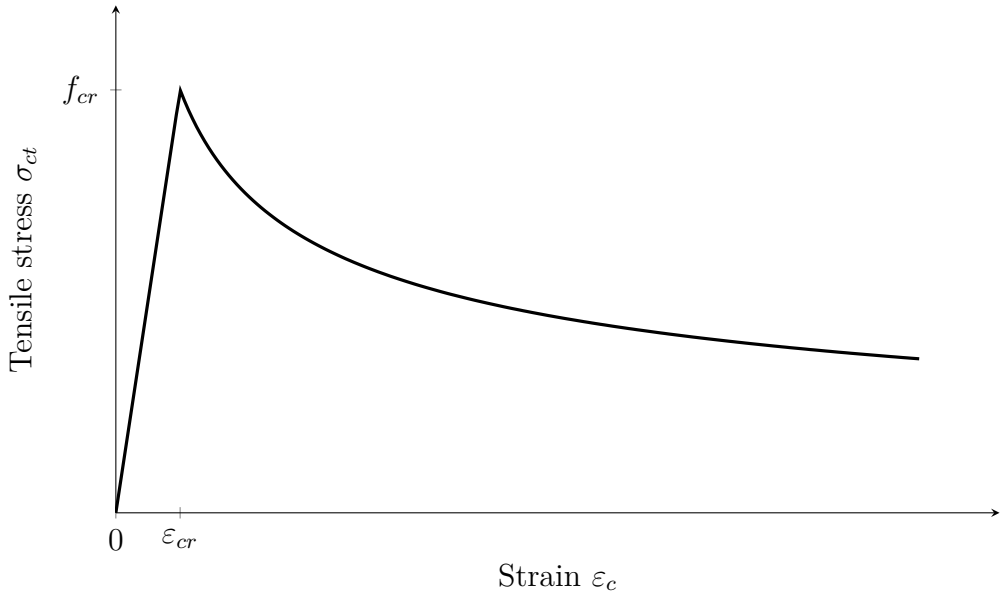

Figure 3.1: Stress-Strain curve using Belarbi and Hsu (1994) expressions.

3.1.1.2. Confined concrete

To include the confined effect produced by stirrups, the model developed by Saatcioglu and Razvi (1992) calculates the concrete confined response based on the unconfined concrete constitutive curve.

Confined stresses

First, the confined compression concrete capacity f_{CC} is defined by the following expression.

$$f_{CC} = f'_{CO} + k_1 f_{le} \tag{3.5}$$

f'_{CO} is the unconfined strength of the concrete member, and k_1 is a function of the Poisson's ratio, which is defined as:

$$k_1 = 6.7(f_{le})^{-0.17} \tag{3.6}$$

Where f_{le} is the equivalent uniform pressure in MPa, so the lateral pressure f_l is:

$$f_{l_{x,y}} = \frac{\sum A_s f_{yt} \sin(\alpha)}{b_{c_{x,y}} s} \tag{3.7}$$

Where α is the angle between the transverse reinforcement and b_c, which is section length in the analysis direction. Also, s is the stirrup separation, A_s, and f_{yt} are the steel transversal section area and yield stress, respectively. However, the equivalent uniform pressure for a rectangular area is:

$$f_{le_{x,y}} = k_2 f_{l_{x,y}} \tag{3.8}$$

Where k_2 is a parameter gathered by Saatcioglu and Razvi (1992) by doing a regression data analysis defined as following:

$$k_2 = 0.26\sqrt{\frac{b_{C_{x,y}}}{s}\frac{b_{C_{x,y}}}{s_{l_{x,y}}}\frac{1}{f_{l_{x,y}}}} \leq 1 \tag{3.9}$$

So the effective lateral pressure for a rectangular section is:

$$f_{le} = \frac{b_{Cx} f_{lex} + b_{Cy} f_{ley}}{b_{Cx} + b_{Cy}} \tag{3.10}$$

Therefore, replacing in Ec. 3.5 the values obtained in Ec. 3.10 and Ec. 3.6 the confined compression concrete capacity is calculated.

Confined strains

First step, is to calculate the confined concrete peak compressive strain ε_1, so it is needed the unconfined concrete peak compressive strain ε_{01} as following:

$$\varepsilon_1 = \varepsilon_{01}(1 + 5K) \tag{3.11}$$

Where K is calculated as following:

$$K = \frac{k_1 f_{le}}{f'_c} \tag{3.12}$$

The following expression can be used to calculate the strain at 85% strength level beyond the peak (ε_{85}) for the confined case:

$$\varepsilon_{85} = 260\rho\varepsilon_1 + \varepsilon_{085} \tag{3.13}$$

Where ε_{085} is the strain at 85% strength level beyond the peak of unconfined concrete and ρ is calculate as:

$$\rho = \frac{A_{Sx} + A_{Sy}}{(b_{Cx} + b_{Cy})s} \tag{3.14}$$

Consequently, the stress-strain relationship of confined concrete is defined by the following expression (Saatcioglu and Razvi, 1992).

$$f = f_{CC}\left[2\left(\frac{\varepsilon}{\varepsilon_1}\right) - \left(\frac{\varepsilon}{\varepsilon_1}\right)^2\right]^{\frac{1}{1+2K}} \tag{3.15}$$

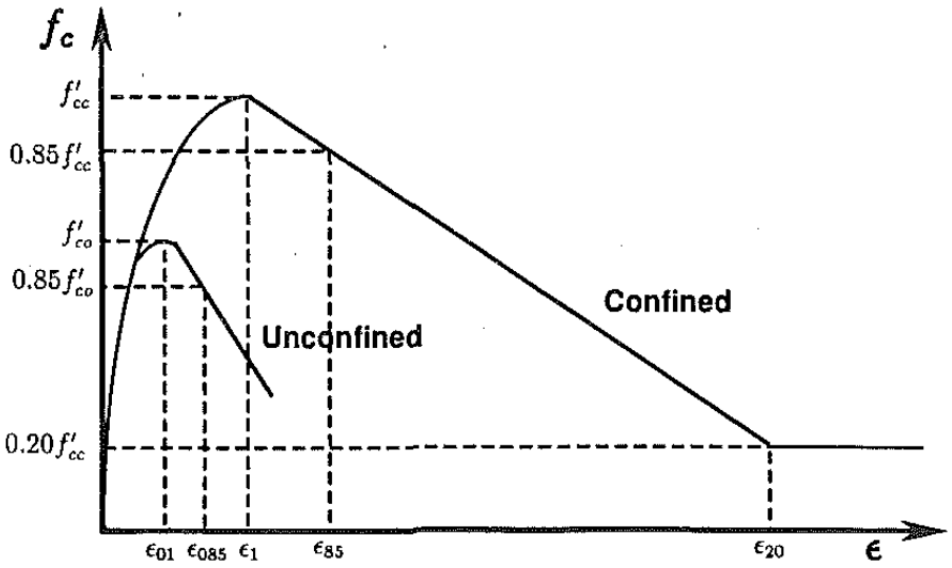

Figure 3.2: Stress - Strain relationship for confined concrete (Saatcioglu and Razvi, 1992).

3.1.2. Steel

In order to characterize the steel reinforcement, a single multi-linear and easy-implementation model will be used. This constitutive model will vary depending on the loading conditions, for tensile loads, the multi-linear model will be adjusted considering the tensile strength test performed previously on the laboratory, assuming that the model is a pushover-type loading (single direction loading), there is no need to use cyclic constitutive models to capture the global element behavior.

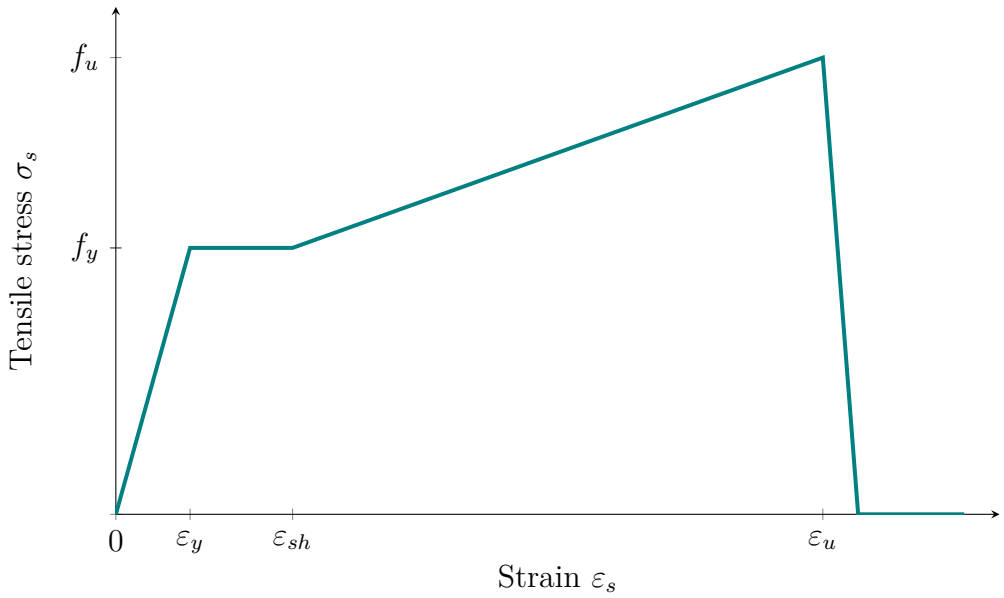

Figure 3.3: Tensile stress-strain curve, considering multi-linear response.

In order to capture the compressive behavior requires incorporating bar buckling to the constitutive law. To achieve that is necessary to base this model in the investigation developed by Massone and Moroder (2009), which is a model that considers concentrated plasticity at four plastic hinges, assuming that two consecutive stirrups act as fixed supports on one side, and a roller support with no rotation in the other, as shown in Fig. 3.4. The investigation found precise correlations between the buckling capacity and the stirrups separation along the beam (L) and the reinforced bar diameter (d). Consequently, considering a bar length value (L/d) of 12.5 as an example, the constitutive compression model obtained is shown in Fig. 3.5.

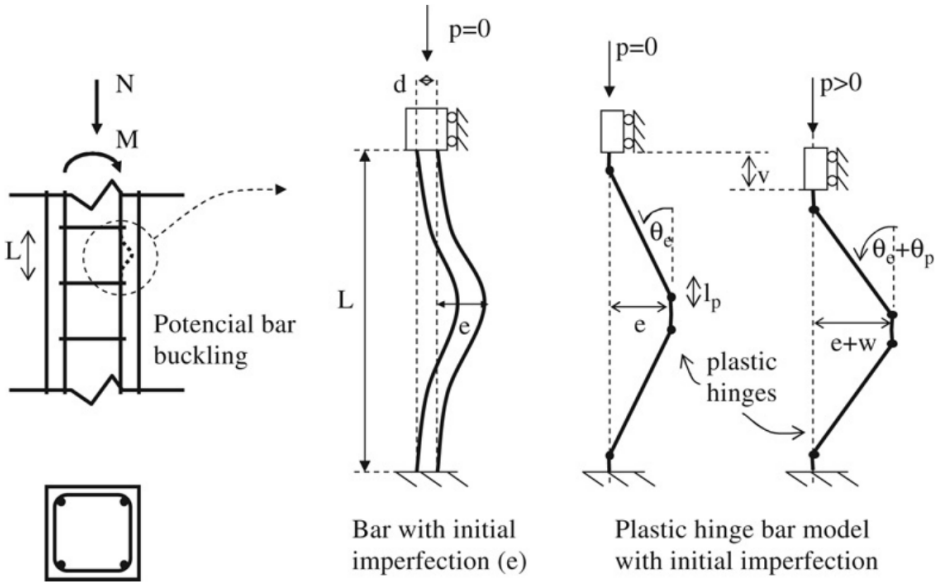

Figure 3.4: Buckling representation of reinforcing bar with initial imperfection (Massone and Moroder, 2009).

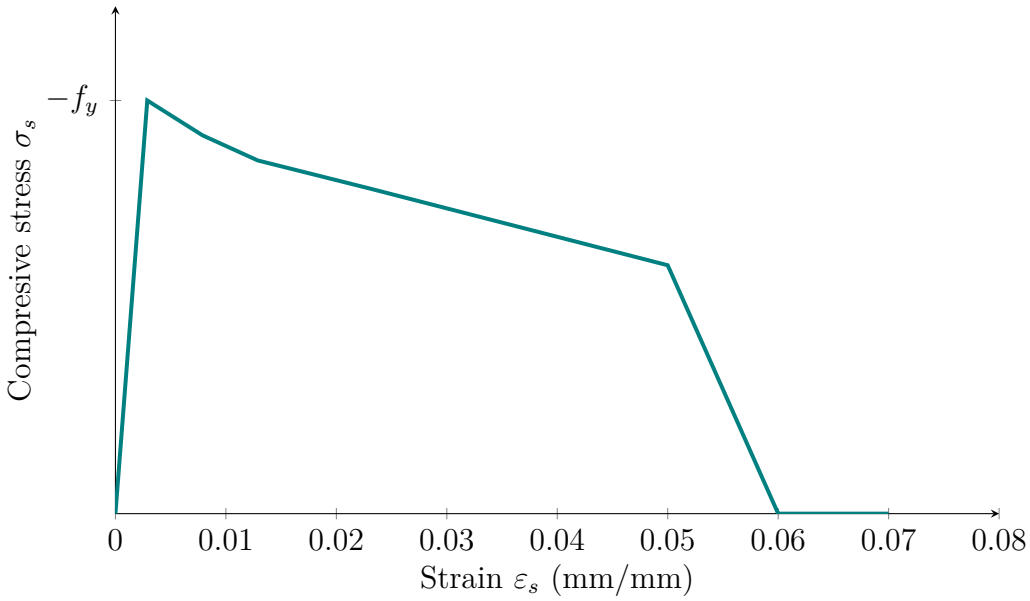

Figure 3.5: Compressive stress-strain curve including buckling effect using Massone and Moroder (2009) expressions.

Belarbi and Hsu (1994) considers a reduction in the yield stress in tension and an increased hardening behavior for steel reinforcing bars embedded in concrete. f_n^* (Eq. 3.16) is the apparent yield stress reduction, and B (Eq. 3.18) is a factor which depends on the ratio of steel area to the net concrete area (ρ), also on concrete cracking stress (f_{cr}) and the real steel yielding stress (f_y).

$$f_n^* = (0.93 - 2B) f_y \approx 0.91 f_y \tag{3.16}$$

$$E_p^* = (0.02 + 0.25B)E_s \tag{3.17}$$

$$B = \frac{1}{\rho}\left(\frac{f_{cr}}{f_y}\right)^{1.5} \tag{3.18}$$

3.2. Beam modeling

Beam tested in this investigation were symmetrical respect with its longitudinal center (Fig. 3.6). Thanks to that feature, modeling half of the beam reduce the number of degrees of freedom (i.e., DOFs). Here and after, 'element' will refer to the number of discretizations along the beam, and 'panel' will refer to the number of discretizations in the transverse section, as shown in Fig. 3.7. The number of elements and panes will depend on both the model convergence issues and tolerance.

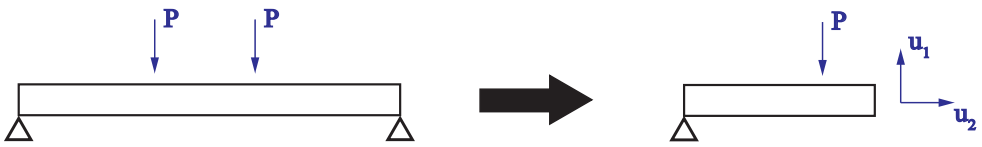

Figure 3.6: Symmetry beam and resulting DOFs.

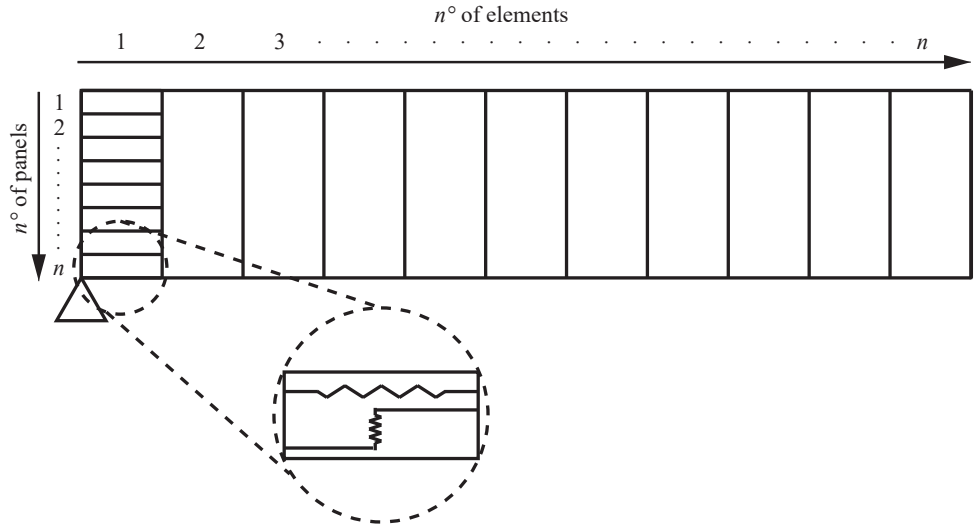

Figure 3.7: Elements and panels arrangement.

3.2.1. E-SFI element

The element used in this model is E-SFI (Efficient Shear-Flexure Interaction) which is an efficient modification made by Lopez C. N. (Massone et al., 2020) of the shear-flexure interaction multiple vertical line element model (SFI-MVLEM) developed by Kolozvari et al. (2015a). This interaction model, removes the internal DOF per panel by incorporating a calibrate expression to calculate the horizontal normal strain (ε_{xx}), reducing both the computational load and processing time.

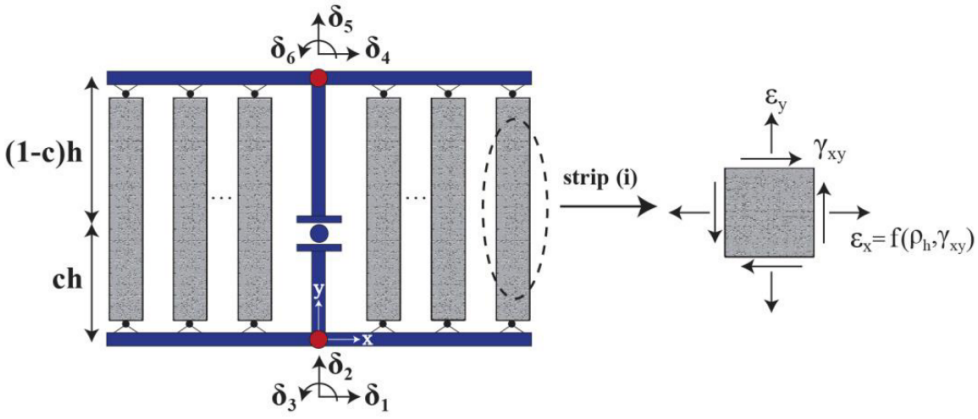

Figure 3.8: E-SFI element, Massone et al. (2020).

In E-SFI element, each uniaxial (macro fiber) element is used to describe the axial/flexural behavior in the original formulation of MVLEM is replaced with an RC panel element subjected to membrane actions, shown in Fig. 3.9. For each RC panel element, axial strain in the longitudinal direction ε_y and shear strain γ_{xy} are calculated from displacements along six nodal DOFs located at the top and the bottom level of a model element (Fig. 3.9), based on assumptions that plane sections remain plane and that shear strains are uniformly distributed along the length of the wall. In addition, using the transverse DOFs assigned to each RC panel element (Fig. 3.9), axial strains in the horizontal direction ε_x are obtained assuming that the resultant horizontal axial stress σ_x (resulting from the contributions from concrete and reinforcing steel) is equal to zero. A cyclic two-dimensional constitutive relationship represents the RC panel behavior described using a constitutive panel model formulation based on the FSAM (fixed strut angle model) developed by Ulugtekin (2010) but also including a shear resisting mechanism along concrete cracks.

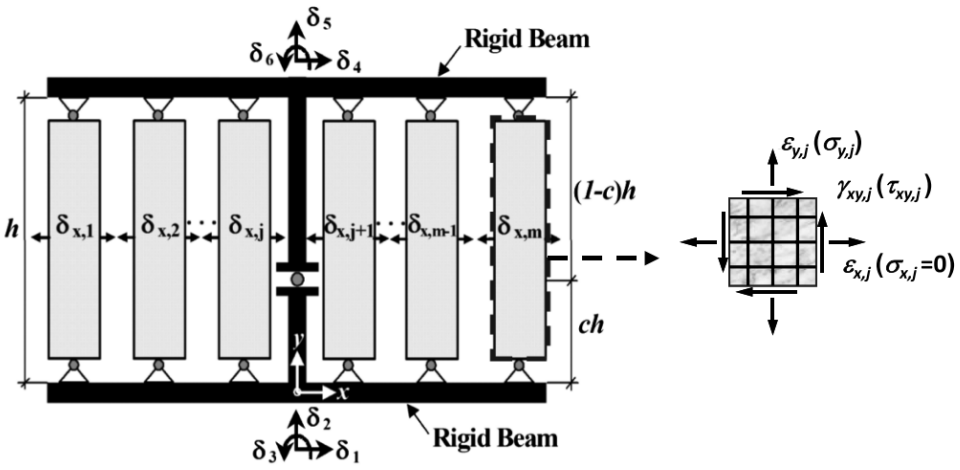

Figure 3.9: SFI-MVLEM element, Kolozvari et al. (2015b).

Chapter 4

Experimental design

To characterize the coarse aggregate concrete with PVA content is necessary to test different mixture arrangements and fully describe its material and the reasoning behind all steps. From the literature review in chapter 2, it can be seen that mortar mixture with PVA addition improves the global behavior of materials and structural members.

This chapter will describe all the steps performed to fully characterize PVA's inclusion in coarse aggregate concrete, from the material used description to the mixture design criteria and the experimental testing with its respective data analysis. The results obtained in this section will work as a base data to calibrate the material used to replicate the test on a computational model in the following chapter.

4.1. Mix design

The following section explains the materials used and the criteria employ to elaborate the plain concrete and PVA-FRC mixture used in the experimental tests to characterize the PVA fiber inclusion into the concrete matrix.

To avoid mixture variation caused by the mixture process. Just one mixture process was adopted and is explained at the end of this section.

4.1.1. Materials

The material used to design the three different mixtures (i.e., coarse aggregate, coarse sand and fine sand) are listed in Table 4.1.

Table 4.1: Materials used to design the mixture.

Material	Type
Cement	ASTM type IP portland-pozzonlan cement (Melon)
Fine Aggregate	No. 4 nominal maximum size sand
Coarse Aggregate	12 mm nominal maximum size gravel
Superplasticizer	Sika® ViscoCrete®-5200 CL
Water	Tap water

4.1.2. Fibers used

Three types of KURALON™ PVA fibers (Fig. 4.1(a - c)) were used on this investigation. The fiber content was chosen based on the research available, and it was measure by the percentage of cement weight and not as specimen volume percentage. The fiber was added to the mixture during the cement paste mixing process.

Oil coated PVA fibers with 12 mm and 15 mm length were tested with fine and coarse aggregate concrete specimens. The mechanical properties are shown in Table 4.2 - 4.4, for fibers 'A' to 'C' respectively. For simple fiber identification, fibers will be noted as a single letter. For example, KURALON™ REC 15/12 mm will be denominated as fiber 'A', as well as the rest of the fibers used in this research (RECS 100L/12 mm as fiber 'B', and RF 600/15 mm as fiber 'C').

(a) REC 15/12 mm

(b) RECS 100L/12 mm

(c) RF 600/15 mm

Figure 4.1: Fibers used provided by KURALON™.

Table 4.2: REC 15/12 mm, fiber 'A' mechanical characteristics.

Specific gravity (g/cm^3)	Diameter (µm)	Length (mm)	Tensile strength (MPa)	Young's Modulus (GPa)	Elongation at break (%)
1.29	40	12	1560	41	6.5

Table 4.3: RECS 100L/12 mm, fiber 'B' mechanical characteristics.

Specific gravity (g/cm^3)	Diameter (µm)	Length (mm)	Tensile strength (MPa)	Young's Modulus (GPa)	Elongation at break (%)
1.29	100	12	1200	28	12.5

Table 4.4: RF 600/15 mm, fiber 'C' mechanical characteristics.

Specific gravity (g/cm^3)	Diameter (µm)	Length (mm)	Tensile strength (MPa)	Young's Modulus (GPa)	Elongation at break (%)
1.29	240	15	1495	42	7.5

4.1.3. Sieve Analysis

As mentioned in the literature review, few investigations aim to determine the response of PVA-FRC with coarse aggregate or concrete mixture. The author found it necessary to create a concrete mixture considering that the final compressive strength is close to what the researchers found on their investigations. Thus, fine (fine sand and coarse sand) and coarse soil (gravel) were needed to design the mix used for this research. Due to laboratory restrictions, it was necessary to buy the different soil types in bags at the local construction supply store.

Nonetheless, before the mix design, it is essential to perform a sieve analysis following ASTM C136 (American Society of Testing and Materials., 2014) in order to determine the particle size distribution of fine and coarse aggregates.

A sieve analysis test is performed to determinate the percentage of different grain sized contained within a soil. The distribution of different grain sizes affects the engineering properties of the soil and with that, the properties of the final mixture.

The procedure consists in:

1. First, it is necessary to homogenize the soil before do the sieve analysis. The best sample splitting method is the cone and quarter technique. This technique consists of pouring all the soil bags into a cone on a clean place, flattening the cone, dividing it into four equal divisions (quartering), and then shovel two opposite quarters. The remaining two quarters are responded into a cone, and the process is repeated until the normative sample size is obtained.
2. Second, record the weight of the given dry soil sample.
3. Ensure that all the sieves are clean, and group them in descending order of sieve apertures (No. 3/4" sieve at top and No. #200 sieve at the bottom, shown in Table 4.5).
4. Carefully pour the soil sample into the first sieve (No. 3/4") and place a pan below it to retain the passing soil. Shake the first sieve over the pan until no soil is left.
5. Weigh and record the weight of each sieve with its retained soil.
6. Repeat the steps 4 to 5 on each sieve in descending order (No. 3/4" to No. #200).
7. Finally weigh and record the weight of the bottom pan with its retained fine soil.

Table 4.5: Aperture size of standard sieves.

Sieve No.	Aperture (mm)	Sieve No.	Aperture (mm)
3/4"	19	#30	0.6
1/2"	12.5	#40	0.475
3/8"	9.5	#50	0.3
#4	4.75	#100	0.15
#8	2.36	#200	0.075
#10	2		

With the gradation and homogenization complete, it is time to perform the sieve analysis following the procedure described before for each type of soil obtained.

4.1.3.1. Fine sand

Fine sand, in this particular case, will act as a fine soil for the mixture design. As mentioned before, to know its granulometry, a sieve analysis was performed. The results are shown in Table 4.6. In addition, the gradation curve is shown in Fig. 4.2.

Table 4.6: Fine sand aggregate sieve analysis test results.

Sieve Size	Sieve Size (mm)	Retained Weight (g)	Individual Retained (%)	Cumulative Retained (%)	Cumulative Passing (%)
3/4"	19	0	0.0	0.0	100.0
1/2"	12.5	0	0.0	0.0	100.0
3/8"	9.5	15	0.8	0.8	99.2
No. 4	4.75	7	0.4	1.2	98.8
No. 8	2.36	9	0.5	1.7	98.3
No. 10	2	3	0.2	1.8	98.2
No. 30	0.6	39	2.1	3.9	96.1
No. 4	0.475	87	4.7	8.6	91.4
No. 50	0.3	250	13.4	21.9	78.1
No. 100	0.15	905	48.4	70.3	29.7
Pan	–	555			
Total	–	1870			
Total Original	–	1875		Fineness Modulus	1.09

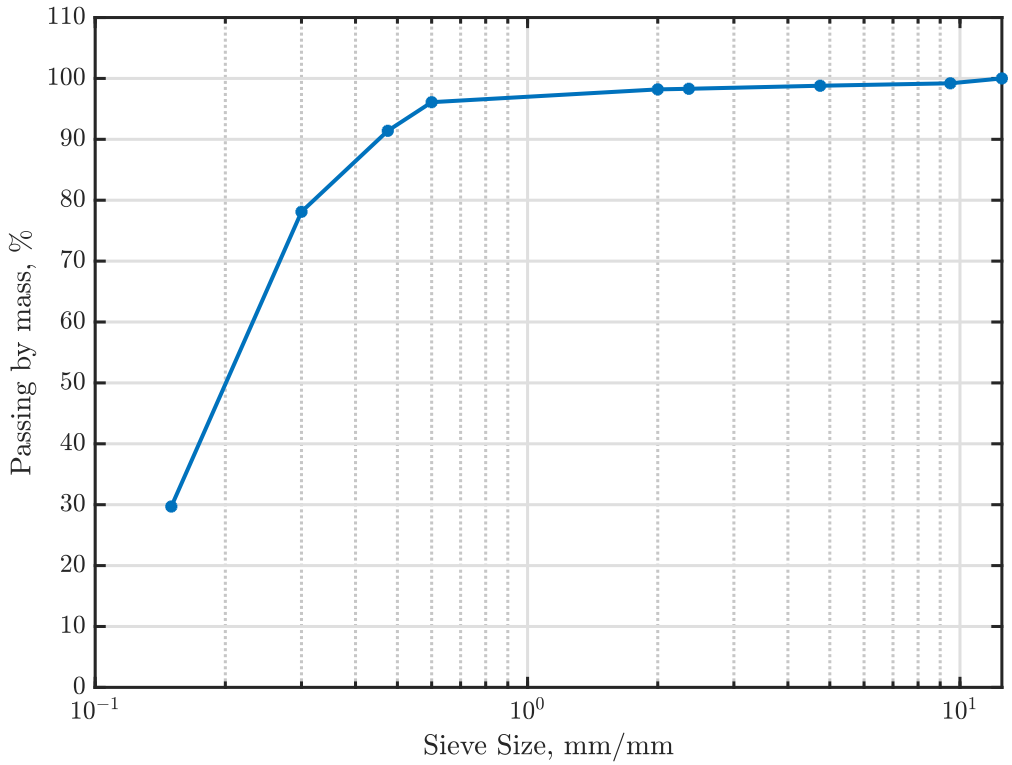

Figure 4.2: Fine sand aggregate gradation curve.

4.1.3.2. Coarse sand

As done with fine sand, the sieve analysis results performed to coarse sand are shown in Table 4.7. The gradation curve is also shown in Fig. 4.3. It is worth noticing that coarse sand also adds gravel particles to the mixture due to the sand's bad gradation bags.

Table 4.7: Coarse sand aggregate sieve analysis test results.

Sieve Size	Sieve Size (mm)	Retained Weight (g)	Individual Retained (%)	Cumulative Retained (%)	Cumulative Passing (%)
3/4"	19	0	0.0	0.0	100.0
1/2"	12.5	0	0.0	0.0	100.0
3/8"	9.5	45	2.3	2.3	97.7
No. 4	4.75	183	9.2	11.5	88.5
No. 8	2.36	173	8.7	20.3	79.8
No. 10	2	36	1.8	22.0	78.0
No. 30	0.6	241	12.1	34.1	65.9
No. 40	0.475	145	7.3	41.4	58.6
No. 50	0.3	235	11.8	53.3	46.8
No. 100	0.15	623	31.4	84.6	15.4
Pan	–	306			
Total	–	1987			
Total Original	–	1995		Fineness Modulus	2.67

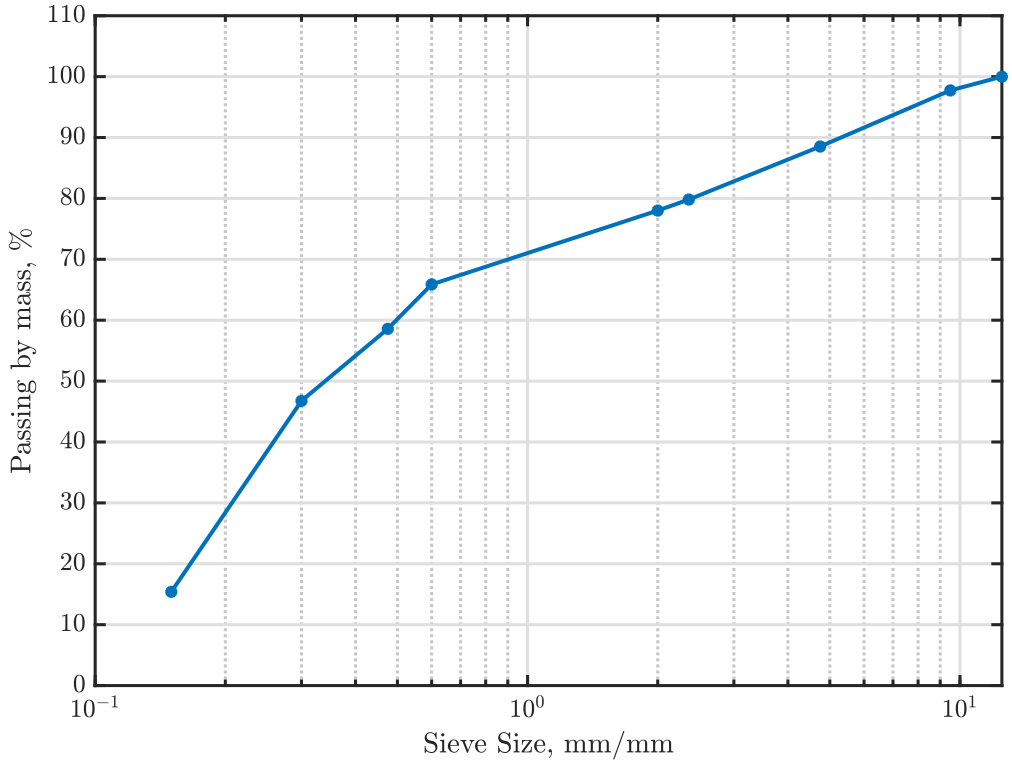

Figure 4.3: Coarse sand aggregate gradation curve.

4.1.3.3. Gravel

Finally, the sieve analysis result of gravel is shown in Table 4.8. Gravel only adds coarse particles to the mixture, as shown in Fig. 4.4. Adding gravel to the mixture is crucial in order to accomplish the objectives of this study.

Table 4.8: Coarse aggregate sieve analysis test results.

Sieve Size	Sieve Size (mm)	Retained Weight (g)	Individual Retained (%)	Cumulative Retained (%)	Cumulative Passing (%)
3/4"	19	28	0.3	0.3	99.7
1/2"	12.5	3925	41.6	41.9	58.1
3/8"	9.5	2675	28.4	70.3	29.7
No. 4	4.75	2538	26.9	97.2	2.8
No. 8	2.36	220	2.3	99.5	0.5
No. 10	2	9	0.1	99.6	0.4
No. 30	0.6	35	0.4	100.0	0.0
No. 40	0.475	0	0.0	100.0	0.0
No. 50	0.3	0	0.0	100.0	0.0
No. 100	0.15	0	0.0	100.0	0.0
Pan	–	0			
Total	–	9430			
Total Original	–	9454		Fineness Modulus	6.96

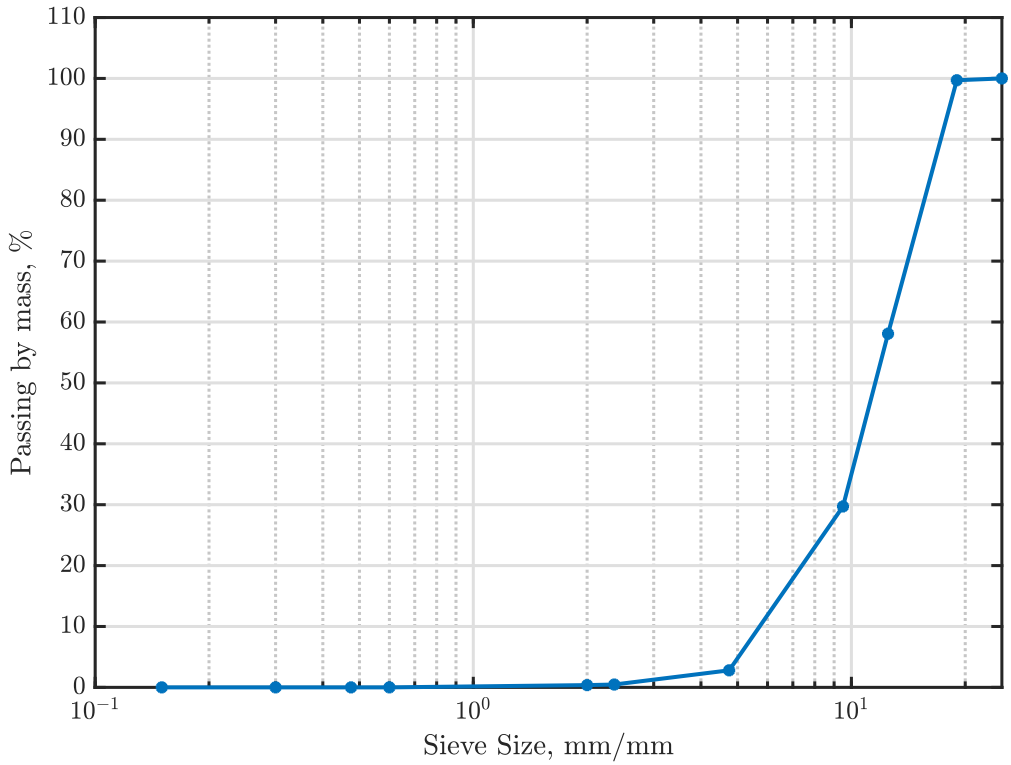

Figure 4.4: Coarse aggregate gradation curve.

4.1.3.4. Mixture Sieve curve

The primary consideration to develop the aggregate proportions is the gradation of the final mix. A well-gradated curve holds particles of a broad range of sizes and has a good representation of all particle sizes from the No. 4 to No. 200 sieves. Thus, it has a linear slope shape on the semi-log graph.

In this investigation, an aggregate proportion of 0.47:0.30:0.23 (gravel:coarse-sand:fine-sand) was acceptable for the coarse aggregate mixture. The gradation curve for each mixture used in this research is shown in Fig. 4.5. Table 4.9 tabulates the aggregate amount used on each mixture and the specific tag to name the mixture.

Table 4.9: Mixtures proportions used.

Mixture name	Tag	Maximum aggregate size (mm)	Aggregate (kg/m^3)		
			Gravel	Sand	
				Coarse	Fine
Gravel	GA	12.5	980	637	477
Coarse sand	CSA	4.75	0	1197	897
Fine sand	FSA	0.475	0	0	2094

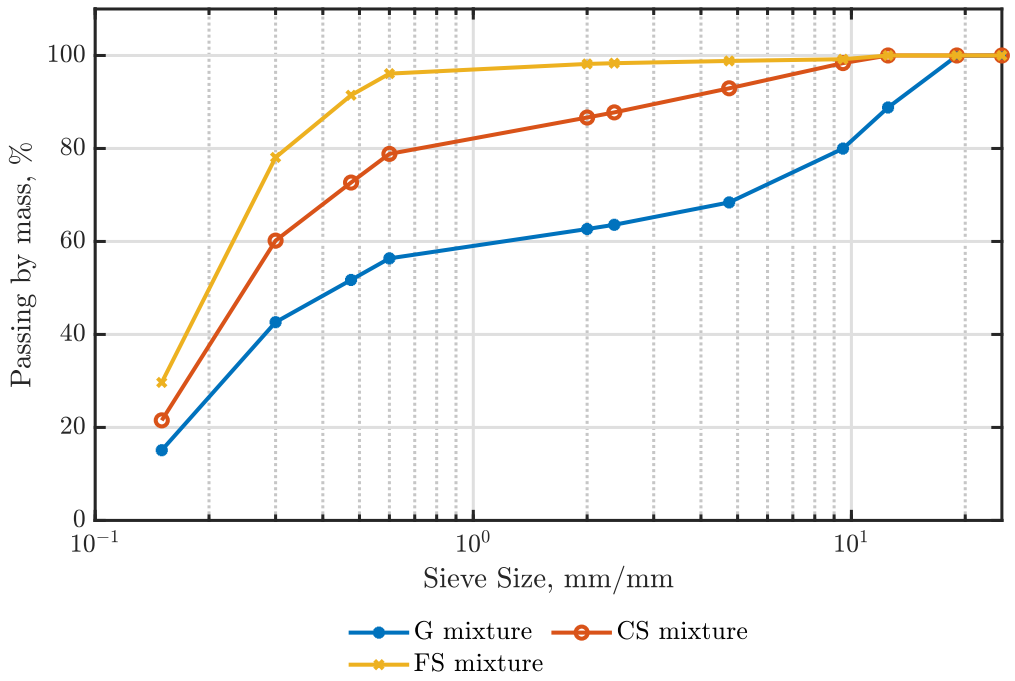

Figure 4.5: Gradation curves for each mixture.

4.2. Tensile test of steel reinforcement bars

The steel used in this research is manufactured in Chile by CAP (*Compañía Siderúrgica Huachipato*), which corresponds to A630-420H steel, it has a nominal tensile strength f_u of 630 MPa and yield strength f_y of 420 MPa, among other requirements, such as resistance to creep and minimum elongation before failure.

Tensile tests were performed on 8 mm diameter bars ($\phi 8$ bars) to obtain the steel mechanical properties. The steel will be used as a beam reinforcement on the beam pushover test.

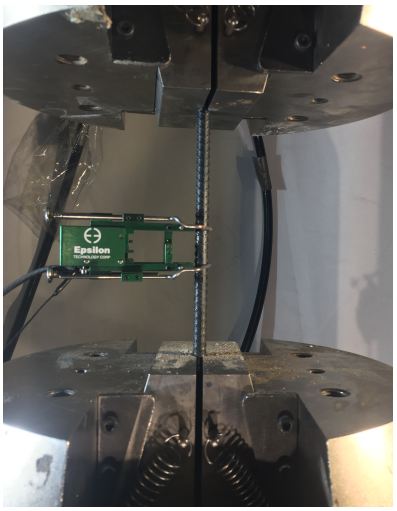

Figure 4.6: Steel bars tensile test setup.

Tests were performed at a strain rate of 5 mm/min on specimens with a length of approximately 150 mm, which corresponds to a quasi-static test. Displacement readings are measured with both the internal dial of the INSTRON® universal machine and the axial extensometer model 3542 from Epsilon Tech® (Fig. 4.6). The extensometer is disconnected at a strain of 0.07 approximately because it is not designed to withstand an impact caused by the steel failure. Fig. 4.7 shows the stress-strain curve of a $\phi 8$ steel, combining the extensometer's reading and the universal machine dial.

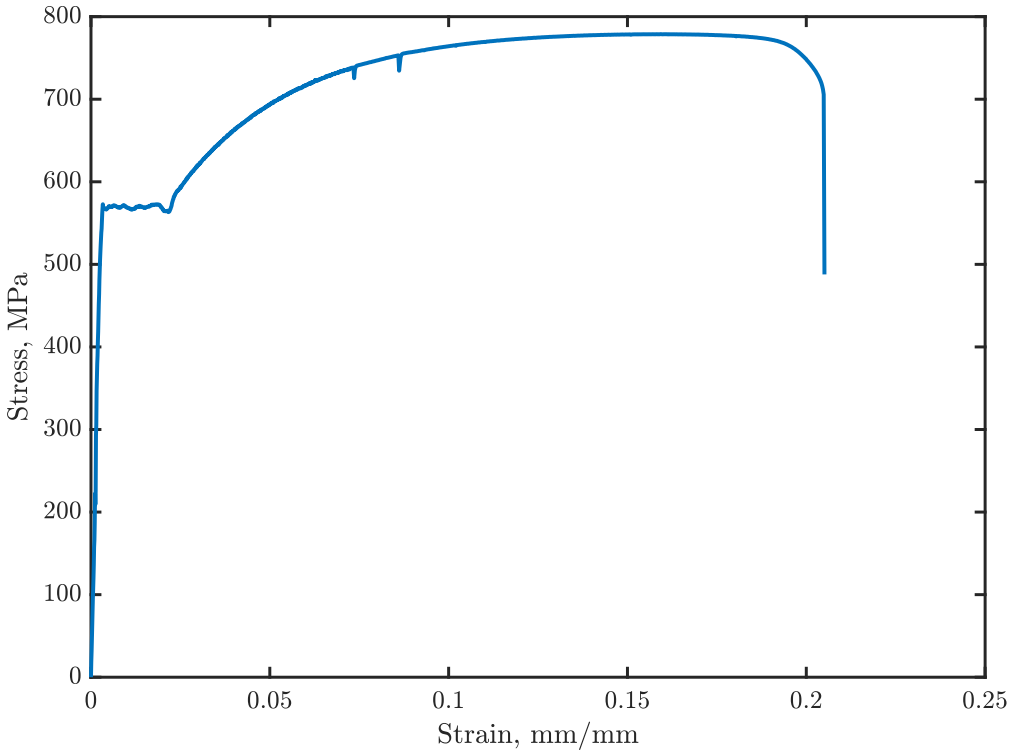

Figure 4.7: Tensile test of $\phi 8$ rebars.

The yielding stress and the ultimate steel stress are tabulated in Table 4.10.

Table 4.10: Steel mechanical properties.

f_y (MPa)	ε_y (-)	E_s (GPa)	f_u (MPa)	ε_u (-)
572.8	0.003321	172.478	782.1	0.2051

4.3. Mixing procedure

Due to the small amount of mixture used during each test, a portable concrete mixer (Fig. 4.8(b)) could not be used because it can potentially absorb a great amount of water, changing the mixture characteristic and adding variability at every mixture load. Therefore, a paint mixer (Fig. 4.8(a)) with sufficient power was used instead, along with a 20 liters bucket as a container.

(a) Paint mixer.

(b) Portable concrete mixer.

Figure 4.8: Mixers used on this investigation.

A mixture procedure for a small amount of material ought to be made. The following list enumerates the steps followed to make the mixture used in the tests.

1. Weight the necessary materials (concrete, PVA fibers, sand, gravel, water, and superplasticizer) depending on the mixture, and place them in separated containers.
2. Mix the cement with the sand and gravel (if needed), in a separate container.
3. Place the paint mixer in the bucket, then pour 1/4 of water into the mixing bucket and add half of the mixture made in the step before.
4. Add another 1/4 of water, and then add the rest of the mixture made in Step 2. On top of the mixture, pour the water left.
5. Turn on the paint mixer and mix the ingredients slowly for 3 minutes to obtain a homogeneous mixture (if the mixture does not need PVA fibers, jump to Step. 7).
6. Slowly add the fiber as the mixer is still on. Keep mixing for another 2 minutes.
7. Mix for one last minute until obtain a homogeneous mixture.

With the homogeneous mixture, the following procedure was elaborated to pour the mixture into both cylindrical and beam casting.

1. Pour the mixture until to fill 1/3 of the casting height.
2. Introduce a steel bar back and forth 25 times in a spiral shape from inside out.
3. Hit the casting from outside 25 times with the steel bar in order to vibrate the mixture inside. Distribute each hit on the perimeter.
4. Repeat the procedure until the casting is full.
5. With a scrapper, scrape the surface to get rid of the exceeding material.

The procedure described before works for both cylindrical and beam specimens. Although, for the beams, due to a large amount of material needed, a portable concrete mixer (Fig. 4.8(b)) was used instead of the paint mixer. Therefore, all the materials were placed into the mixer simultaneously, and the fiber was slowly incorporated into the mixture.

4.4. Test results

4.4.1. Preliminary tests

The purpose of the preliminary tests is to obtain results that provide a first approach on the behavior of PVA-FRC, assess the SP inclusion, and test the direct tensile setup proposed by Nicolas Vasquez in its research (Vasquez, 2019).

During the first preliminary test, was concluded that concrete workability decreases with the addition of PVA fibers. It was also found that the addition of SP improves the mixture workability and it has a little impact on the concrete strength. In addition, SP also increases the matrix stiffness because it accelerates the curing process. Specimens showed low variability on equal mixtures. Therefore, during this test, the mixing procedure was elaborated. The mixing procedure is described in Section 4.3.

The second preliminary test's main purpose was to find the right amount of superplasticizer needed in the mixture and use the direct tensile setup used by Nicolas Vasquez in its research (Vasquez, 2019) to assess the PVA-FRC. PVA fiber 'A' was used in this test, its mechanical properties can be found in Table 4.2. The cement paste consistency in specimens with 1.23% fiber content and superplasticizer is shown in Fig. 4.9.

Figure 4.9: Concrete paste with PVA fiber.

The direct tensile test results were inconsistent between equal specimens. Some specimens failed in planes should not have failed (e.g., at the epoxy gluing in the borders), shown in Fig. 4.10(b). Only two specimens had the expected failure, one of each mixture. Thus, the

results among them are not comparable because both had different failure planes; one torsional due to the border condition applied by the testing machine, and the other as expected, a horizontal plane in the middle (Fig. 4.10(a)). Consequently, all specimens showed that PVA fiber was correctly distributed along the transversal section.

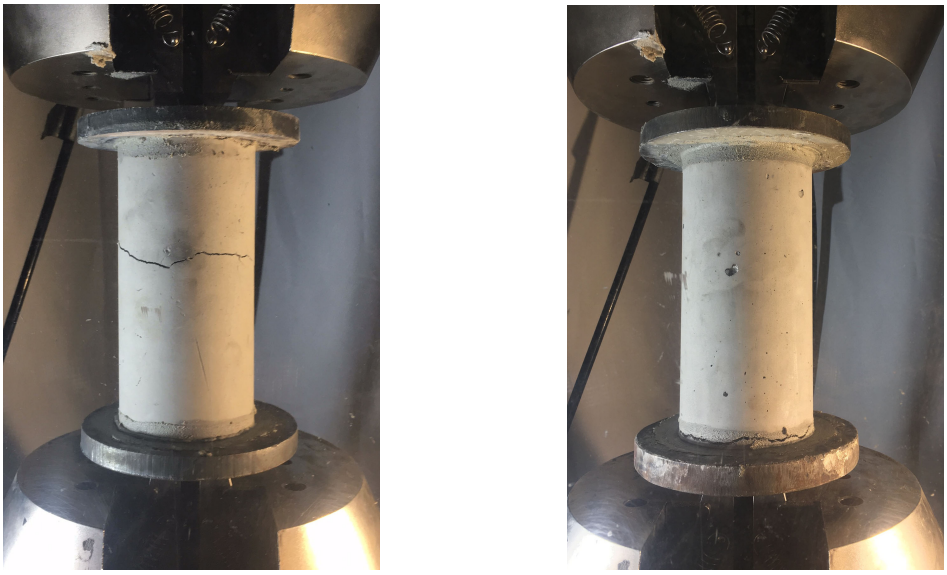

(a) Expected failure

(b) Failure due to border conditions

Figure 4.10: Mixture consistency.

In conclusion, due to the direct tensile test demands a high time consumption in its execution and the fact that the results are not consistent, the test was discarded for further testing, and the author had to find another way to assess the residual strength of coarse aggregate PVA-FRC. On the other hand, all further specimens tests will have a w/c-ratio of 0.4 and SP.

The preliminary test's results detailed are shown completely in Appendix A.

4.4.2. Results

The preliminary tests helped determine the mixture dosage and mixing process and the correct testing protocol to perform the following testing. This section will explain the testing procedure, beginning from the dosage used to the testing setup, and the main results of each specimen.

Following the same procedure as before, three specimens were cast for each mixture, although only two specimens were tested, having a total of forty-two specimens for the compressive strength test, and the other specimen was cut into three disks to perform the indirect tensile test. In this time, all three fiber types were used. As fiber 'A' was used at each preliminary test, and considering the great number of specimens to test, fiber 'A' will only be used with a coarse aggregate mixture (GA). All three mixtures will be used for the rest fibers ('B'

and 'C'), i.e., coarse aggregate (GA), coarse sand (CSA), and fine sand (FSA). All mixtures will use a water-to-cement ratio of 0.4. The fiber content used will be 0%, 0.62%, and 1.23%. The matrix detail is shown in Table 4.11.

Table 4.11: Testing matrix.

Specimen tag	Aggregate type	PVA content (%)
Fiber A mixtures		
M01	GA	0
M02	GA	0.62
M03	GA	1.23
Fiber B mixtures		
M04	GA	0
M05	GA	0.62
M06	GA	1.23
M07	CSA	0
M08	CSA	0.62
M09	CSA	1.23
M10	FSA	0
M11	FSA	0.62
M12	FSA	1.23
Fiber C mixtures		
M13	GA	0
M14	GA	0.62
M15	GA	1.23
M16	CSA	0
M17	CSA	0.62
M18	CSA	1.23
M19	FSA	0
M20	FSA	0.62
M21	FSA	1.23
For all concrete mixtures		
Water = 318 kg/m^3		
Cement = 796 kg/m^3		
Superplasticizer (SP) = 1500 ml/m^3		

4.4.3. Concrete compression test

Specimens of 100 mm diameter x 200 mm height were tested at a deformation rate of 0.5 mm/min, allowing for a very representative PVA concrete backbone curve at the pre-peak stage and after the peak (residual strength stage). Each specimen is tested until a 20% compressive strength (f'_c) after the peak. Each specimen was cast and cured for approximately

fifty days. The curing days for each specimen are tabulated in Table 4.12. Then, the tests were performed immediately after the curing/exposure finalization.

Table 4.12: Specimens' curing days.

Specimen	Casting date	Test date	Curing days
M01	17-10-2019	11-12-2019	55
M02	17-10-2019	11-12-2019	55
M03	17-10-2019	11-12-2019	55
M04	17-10-2019	11-12-2019	55
M05	17-10-2019	11-12-2019	55
M06	18-10-2019	11-12-2019	54
M07	18-10-2019	11-12-2019	54
M08	18-10-2019	11-12-2019	54
M09	18-10-2019	11-12-2019	54
M10	04-11-2019	23-12-2019	49
M11	04-11-2019	23-12-2019	49
M12	04-11-2019	23-12-2019	49
M13	04-11-2019	23-12-2019	49
M14	05-11-2019	23-12-2019	48
M15	05-11-2019	23-12-2019	48
M16	05-11-2019	23-12-2019	48
M17	05-11-2019	23-12-2019	48
M18	06-11-2019	23-12-2019	47
M19	06-11-2019	23-12-2019	47
M20	06-11-2019	23-12-2019	47
M21	06-11-2019	23-12-2019	47

The universal machine cell load obtains the load, and the deformation was assessed by two LVDTs attached opposite to each other to the specimens by an external ring slightly drilled to the specimen surface, as shown in Fig. 4.11. These rings helped determine the specimens' deformations at the center section with a length of 2/3 its height.

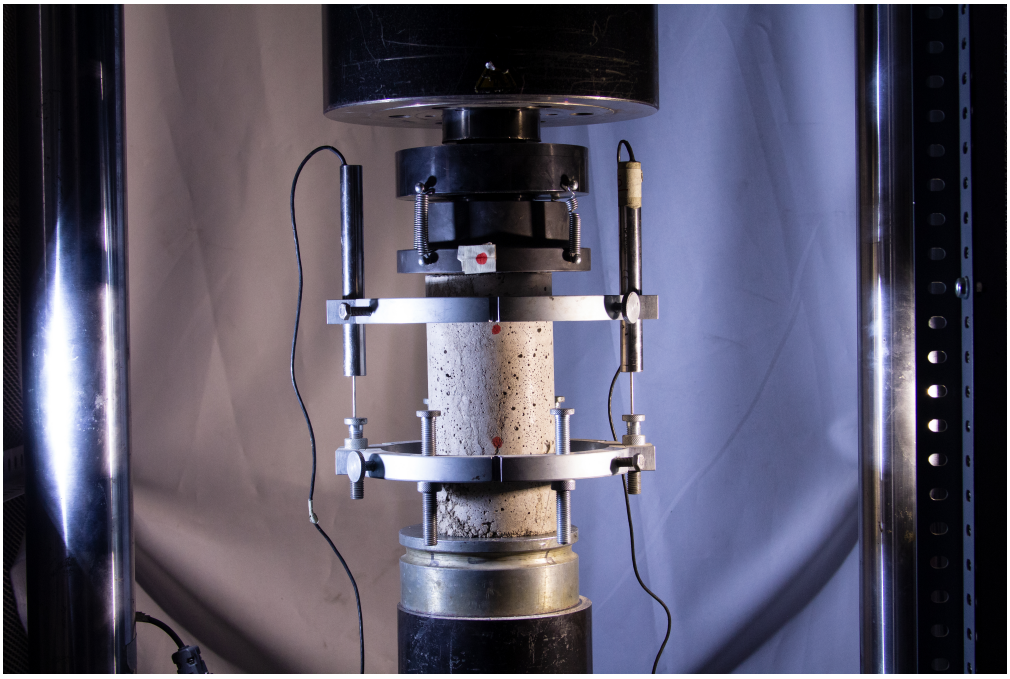

Figure 4.11: Compression test setup.

Both LVDTs were useful to assess the specimens' pre-peak displacement. However, after the peak, some threaded rod started to lose at the nonlinear stage, and the rings began to rotate respected the still attached rods. Therefore, the displacement measurements were not trustful, and some rings even fell from the specimen, caused by the stresses' distribution inside the specimen. One way to address the problem was to use the displacement measurement from the internal testing machine dial to obtain the specimen's residual displacement.

Fig. 4.12(a) illustrates the stress-strain curve obtained using the LVDTs displacement measurement. Thus, in order to obtain reliable relation, the pre-peak data was used, as shown in Fig. 4.12(b), the data left was discarded due to the rotation of the external rings which in some cases fell from the specimen. Therefore it will not be considered in the analysis.

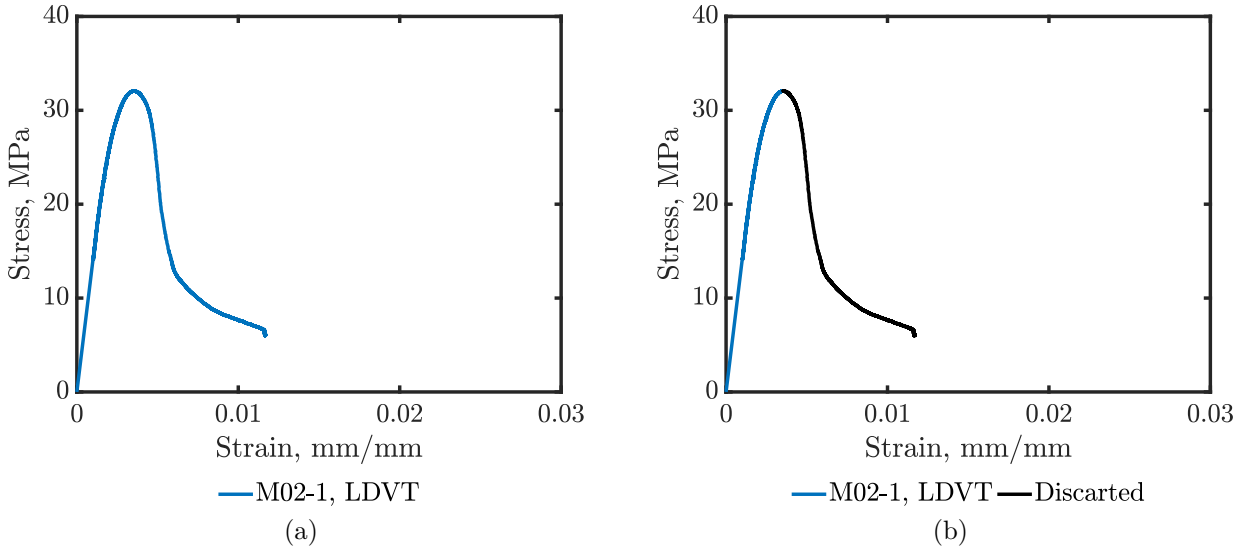

Figure 4.12: (a) Example of data extracted by LVDT, and data used (b).

On the other hand, for the INSTRON® internal dial measurement, only the post-peak stress-strain curve was used, the linear data was discarded. The procedure is shown in Fig. 4.13.

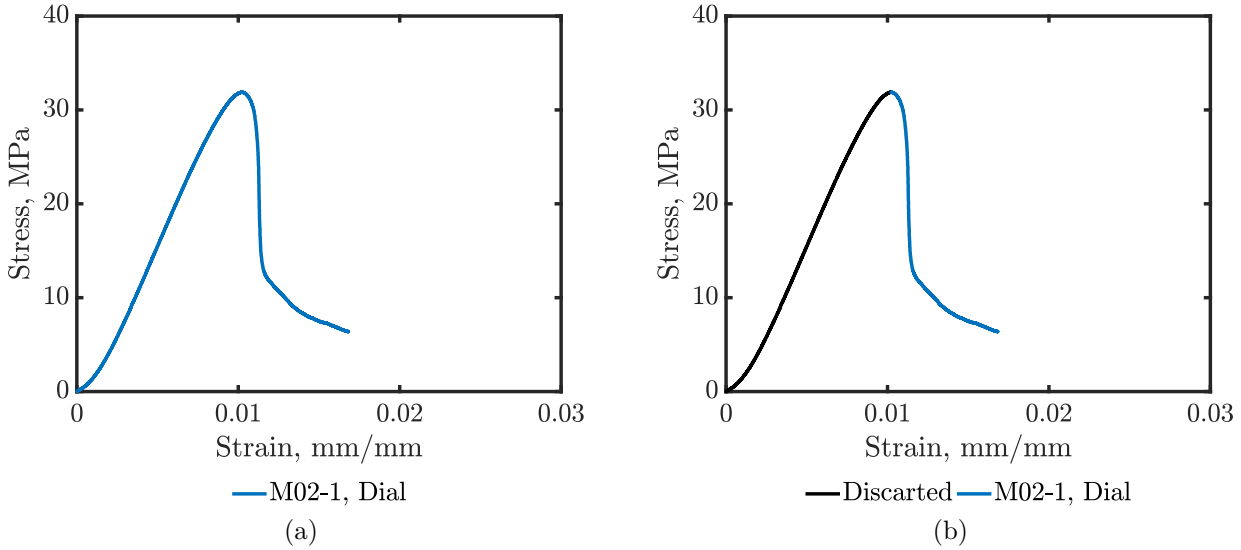

Figure 4.13: (a) Example of data extracted by INSTRON® dial, and data used (b).

The procedure described before was applied to each specimen mixes pair. Consequently, there are two curves for each mixture. Each curve had a different response, and to finally have only one curve for each mixture, it was needed to calculate a simple average between the curves. However, there was a problem with this, as each test were performed at a different time step, it is not straight forward to obtain the average curve. Thus, each stress-strain curve was converted to the same strain step taking the maximum strain of both specimens

and divided it into 'n' steps, and then, each curve was linearly interpolated to use the same strain vector. The final curve for each specimen and the average curve are exemplified in Fig. 4.14 for the M02 case.

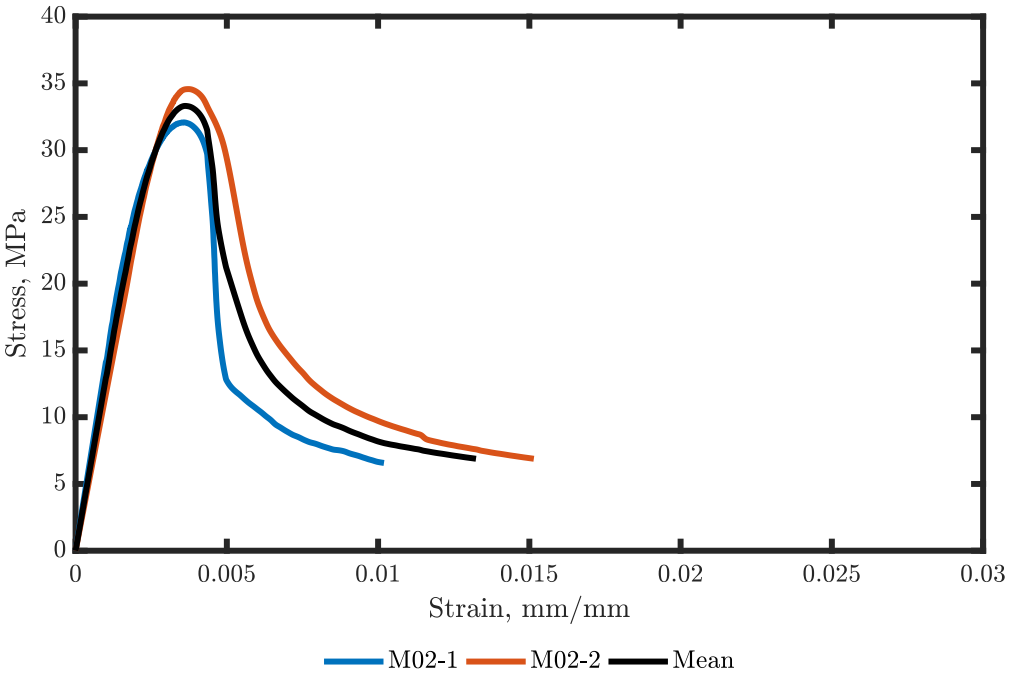

Figure 4.14: Mean of different sampling rate data (M02-1 & M02-2).

Table 4.13 shows the error dispersion values after obtaining the mean curve of different sampling rate specimen data. From the table, it can be noticed that the difference between stress-strain data of similar mixtures is at much 6 MPa in the worst case (M01) but on average, the difference varies from 0.5 to 4 MPa. In conclusion, consecutive specimen testing has low variability.

Table 4.13: Test's error dispersion values.

Specimen	Mean (MPa)	Standard deviation (MPa)	Median (MPa)
M01	3.049	3.239	2.057
M02	2.321	1.957	1.618
M03	2.649	1.270	2.760
M04	0.294	0.167	0.301
M05	1.638	1.863	0.851
M06	1.184	0.813	1.026
M07	0.880	0.827	0.721
M08	2.159	1.193	1.812
M09	2.585	2.017	1.820
M10	1.218	1.198	0.930
M11	0.392	0.268	0.358
M12	0.605	0.627	0.284
M13	1.672	1.703	1.179
M14	1.043	0.484	1.027
M15	1.053	0.930	0.900
M16	0.508	0.452	0.364
M17	0.732	0.786	0.515
M18	1.943	2.973	0.317
M19	1.188	1.200	0.850
M20	0.710	1.611	0.180
M21	1.001	0.642	1.130

The compression testing results are shown in Figs. 4.15 - 4.17, where each figure summarizes the different mixtures tested, and each subfigure within compares the response of each fiber varying its fiber content by color; blue, red, and yellow are 0%, 0.62% and 1.23% fiber content, respectively.

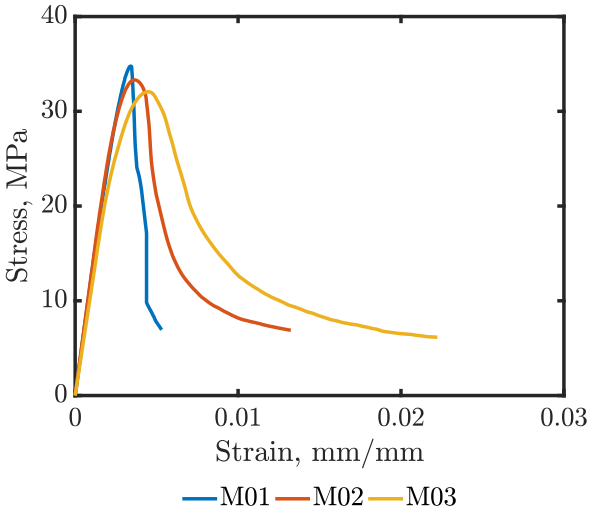

(a) Fiber 'A'.

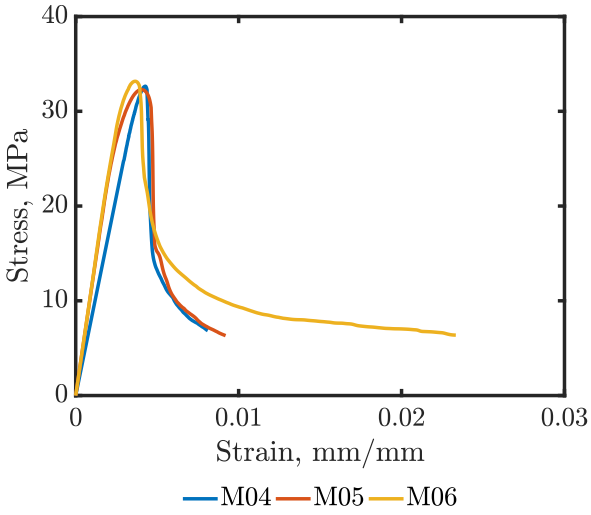

(b) Fiber 'B'.

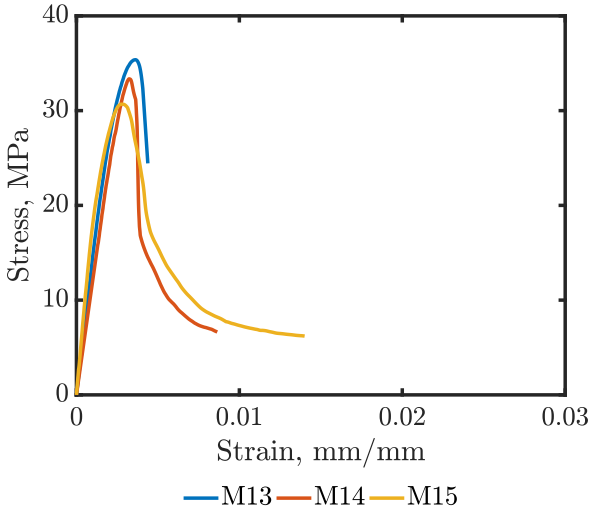

(c) Fiber 'C'.

Figure 4.15: Compression test results for mixture No. 1.

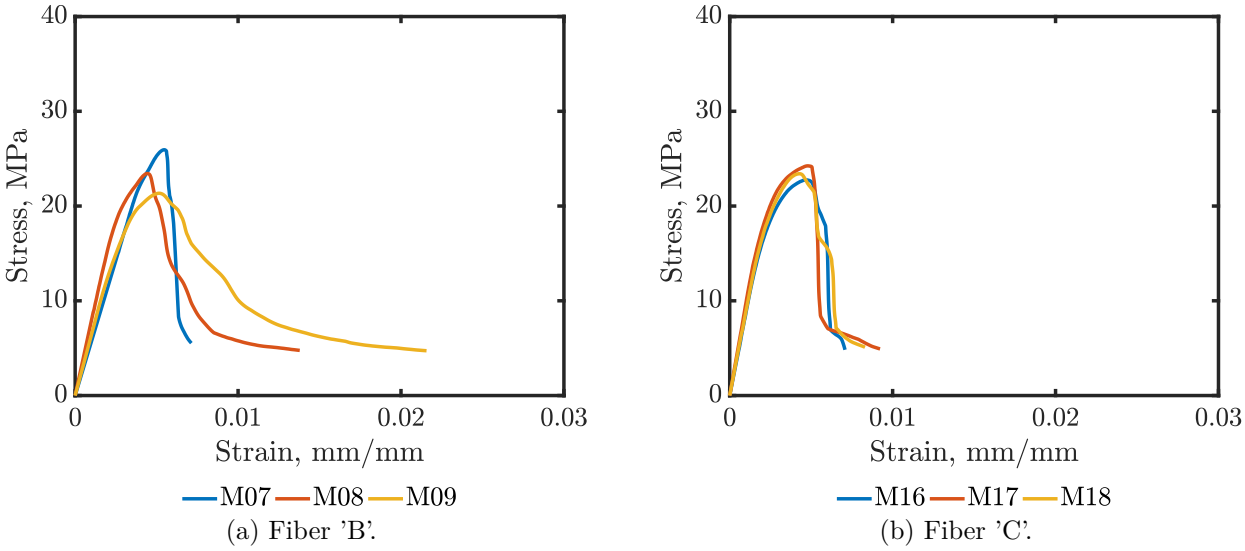

(a) Fiber 'B'. (b) Fiber 'C'.

Figure 4.16: Compression test results for mixture No. 2.

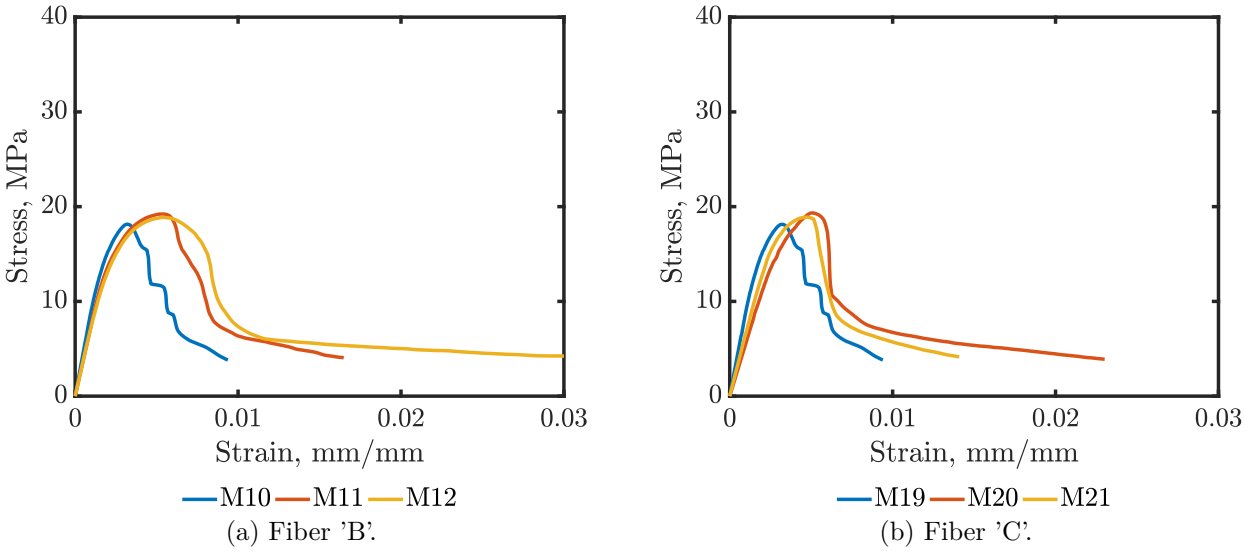

(a) Fiber 'B'. (b) Fiber 'C'.

Figure 4.17: Compression test results for mixture No. 3.

The specimens presented a shear-type failure. In Fig. 4.18, the failure mode of the specimens made with fiber 'A' and mixture '1' are shown. It can be deduced that the failure shape in specimens with fiber is contained, also presents more deformation in the perpendicular direction to the loading direction (vertical), showing that the fiber distribution within the specimen helps visually to the specimen confinement by forming bridges along the transversal cracks (Fig. 4.18(b)).

(a) M01 (b) M02 (c) M03

Figure 4.18: Compression failure M01 - M03, fiber 'A', mixture No. 1.

Summarizing, it can be observed that the plain concrete specimens have a fragile response after the peak stress (blue curve on each subfigure in Figs. 4.15 - 4.17), having an abrupt stress decrease. On the other hand, specimens with different fiber content showed slowing stress decreasing rate after the stress peak; in other words, those specimens had a ductile failure presenting a residual strength after the peak; it also showed an increased strain capacity compared to plain concrete, reaching strain up to approximately 2.4% in coarse aggregate matrices (Fig. 4.15(b)), and up to 3% approximately in fine aggregate matrices (Fig. 4.17(a)).

Additionally, following the mixing procedure employed in this research for coarse aggregate matrices, the compressive stress reduction by incorporate fiber into the mixture was, on average, approximately 8% compared to a plain concrete matrix for the worst case (Fig. 4.16(a)). However, in most cases, the addition of PVA fiber to the mixture increased the compressive strength capacity up to 2% (Fig. 4.16(b) and 4.17(b)). The compressive stress reduction reached in this research validates the information about this phenomenon found in the literature review.

The main testing variables' data, such as compressive peak stress, strain at peak stress, maximum strain, and stress at maximum strain, are shown in Table 4.14.

Table 4.14: Compression test data summary for each specimen.

Specimen	Peak Stress (MPa)	Strain at peak (-)	Stress at max strain (MPa)	Max. Strain (-)
M01	34.80	0.00341	6.90	0.00531
M02	33.30	0.00362	6.90	0.01324
M03	32.10	0.00450	6.10	0.02223
M04	32.60	0.00427	6.90	0.00810
M05	32.30	0.00402	6.30	0.00920
M06	33.20	0.00364	6.40	0.02333
M07	25.90	0.00547	5.50	0.00713
M08	23.40	0.00443	4.80	0.01379
M09	21.30	0.00516	4.70	0.02157
M10	18.10	0.00317	3.80	0.00937
M11	19.20	0.00531	4.10	0.01649
M12	18.90	0.00538	3.80	0.03390
M13	33.40	0.00465	6.90	0.00860
M14	33.40	0.00324	6.60	0.00864
M15	30.70	0.00280	6.20	0.01401
M16	22.80	0.00471	4.80	0.00708
M17	24.20	0.00478	4.90	0.00923
M18	23.40	0.00428	5.10	0.00830
M19	18.10	0.00319	3.80	0.00940
M20	19.30	0.00509	3.90	0.02301
M21	18.90	0.00470	4.20	0.01408

4.4.4. Indirect tensile test

Indirect tensile tests or splitting tests were performed on both plain concrete and PVA fiber concrete disks. These disks were 100 mm in diameter and had a 50 mm width to obtain a dimension ratio of 1:2. Testing was performed by the INSTRON® universal machine model 600LX, with displacement control at a 1.0 mm/min. The test assembly is easy, consisted of mounting a steel plate to the bottom and the top of the disks covered by a 1 mm thick plywood, in order to distribute the stresses along the disk's width, then the disk is placed aligned horizontally to both plates and placed in the universal machine.

From Fig. 4.19(a) can be seen that two LVDTs were placed in the transversal direction of loading to measure the transversal displacement of the specimen. This measurement was not successful because when a failure occurs, both half disks rotate. Thus it begins to displace in both planar directions, vertically and horizontally; consequently, using LVDTs, which can only measure displacement in one direction, is not enough to assess the behavior of the residual curve.

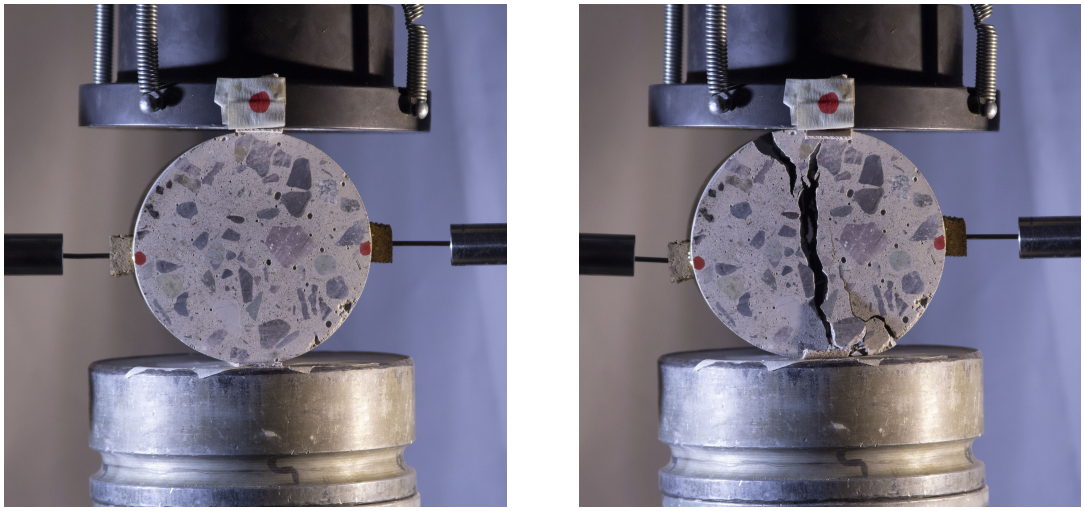

(a) Test Start (b) Test End

Figure 4.19: Indirect tensile test setup.

Other measurement methods were employed to measure the horizontal displacement and the rotation of both half disks. One of those methods was called 'RGB', this method used DIC to find at each camera shoot the relative distance between both red dots painted to the disks surface, (Fig. 4.19(a)). This method had a couple of flaws for this measurement case, one of those was the camera resolution, because the concrete in tensile loading only reaches a strain lower to 1%, calculating the strain showed many errors due to the negligible displacement between shots in the linear stage. The other cause was the camera shooting rate; the software used to process the camera shoots at a constant rate, needed at least five seconds between shots in order to process the image, writing it to the hard disk in the computer and then have the camera ready for the next shoot. Considering the loading rate of 1.0 mm/min, five seconds is an ample strain change within the specimen. Thus the measurement for the linear part showed plenty of 'jumps' at each data point. An example of the data obtained by this method is showed in Fig. 4.20 for specimens M01-M03.

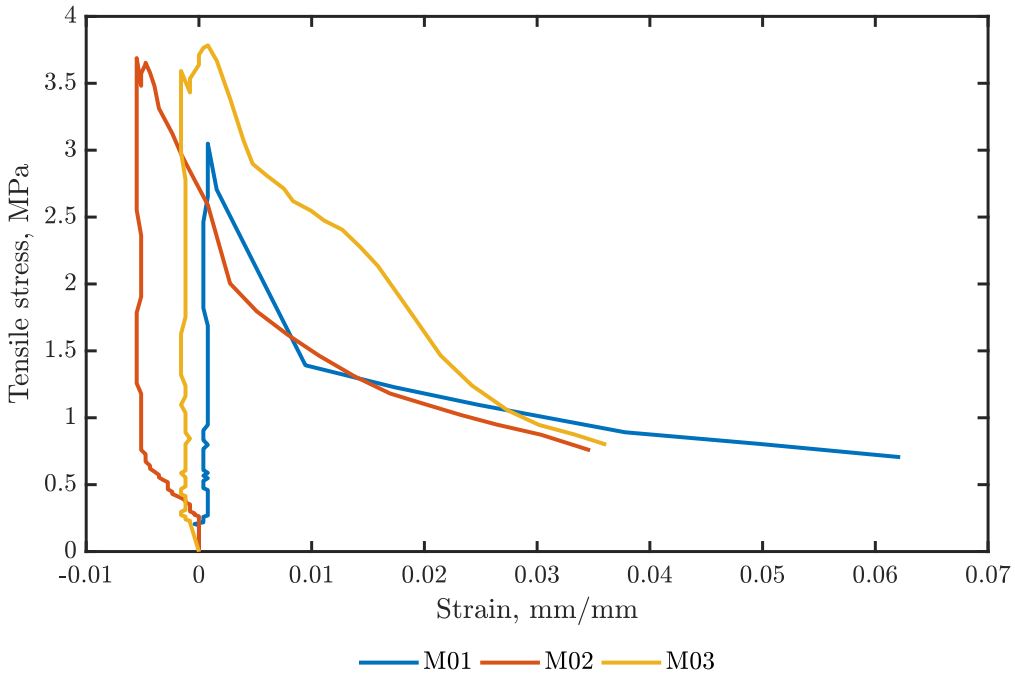

Figure 4.20: Stress-strain curves by using 'RGB' method on indirect tensile tests.

Both methods could not measure the transversal displacement of the disk. Thus, the indirect tensile test was only used to measure each specimen's maximum tensile capacity—the bar graphs on Figs. 4.21 to 4.23 show the maximum tensile strength of the different mixtures tested, and each subfigure within compares the response of each fiber varying its fiber content by color; blue, red, and yellow are 0%, 0.62% and 1.23% fiber content, respectively.

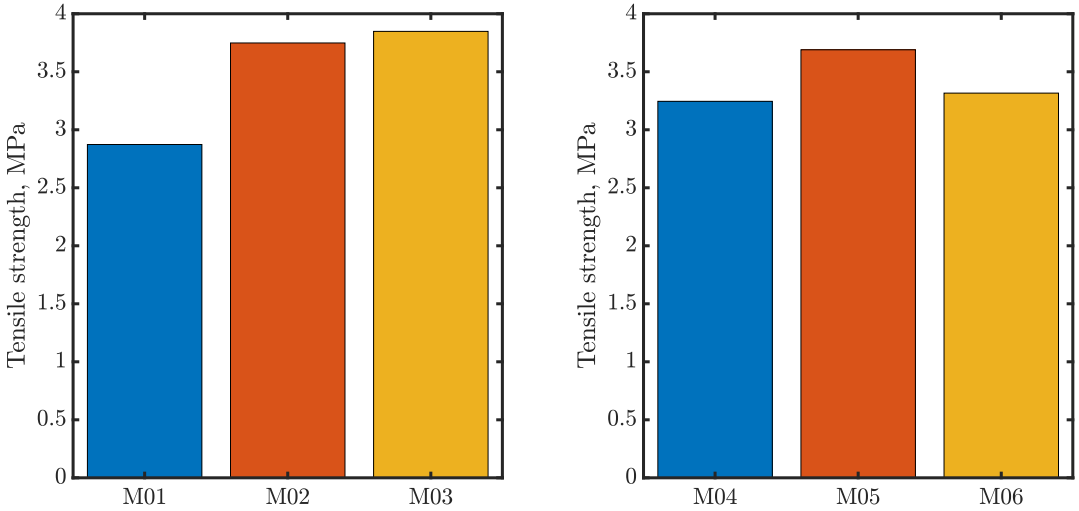

(a) Fiber 'A'.

(b) Fiber 'B'.

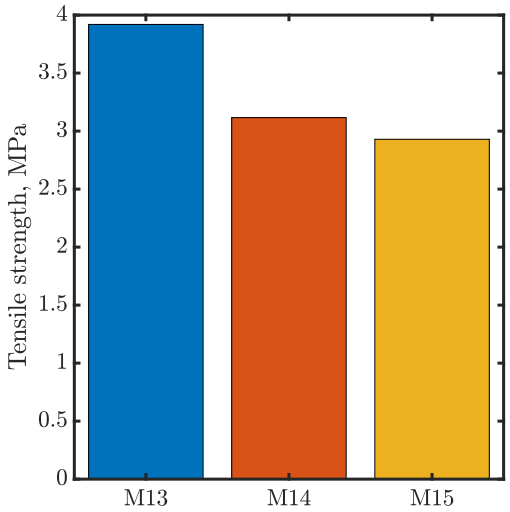

(c) Fiber 'C'.

Figure 4.21: Tensile test results for mixture No. 1.

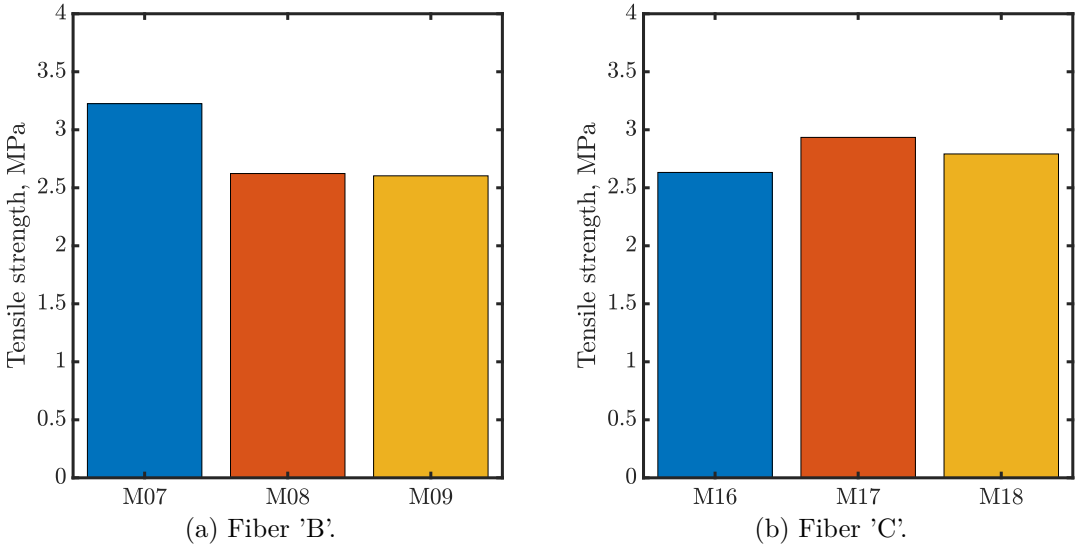

(a) Fiber 'B'. (b) Fiber 'C'.

Figure 4.22: Tensile test results for mixture No. 2.

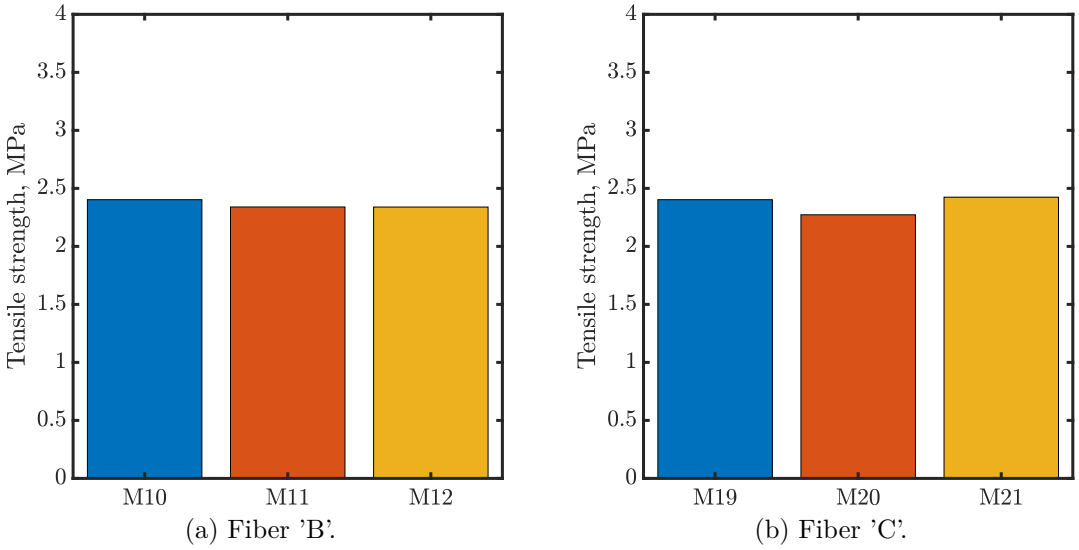

(a) Fiber 'B'. (b) Fiber 'C'.

Figure 4.23: Tensile test results for mixture No. 3.

It can be observed from Figs. 4.21-4.23 that there are negligible differences on the maximum stress capacity between comparable specimens (Fig. 4.23). The literature PVA fiber is known for giving the concrete a higher strain capacity (ductility) than peak strength. Also, in this analysis, the maximum stress peak is extracted to assess the stress capacity ignoring that some data might have two peaks, the first when the crack is reached and the second occurs when the PVA fiber bridging exceeds its pullout capacity. However, PVA fibers can give the concrete matrix a second stress peak by acting as bridges between cracks, improving its capacity compared to a plain concrete matrix. Nevertheless, quantitatively is not enough to make conclusions.

The data extracted is shown in Table 4.15, along with the maximum compressive strength

(f'_c) found in the section before. The indirect tensile percentage of compressive strength varies from 8.2 to 13.2. Analyzing the specimens in groups of three (M01-M02-M03, M04-M05-M06, ..., M19-M20-M21), it can be noticed that the first of each group (plain concrete matrix) has the lower tensile strength of the three in most cases, except in Fig. 4.22(a), where both PVA fibers mixture had lower tensile strength compared to the control specimen. It can be due to many factors; fiber hardness, chemical bond to the mixture, amount of voids inside the mixture, maximum aggregate size. Anyway, fiber 'B' showed the same behavior of mixture No. 2 as mixture No. 3, which concludes that this fiber has a better behavior with coarse aggregate specimens (mixture No. 1) than the other mixtures. Nonetheless, the tensile improvement showed with the coarse aggregate mixture is not stable (Fig. 4.21(b)).

Fiber 'A' was only tested with coarse aggregate specimens to reduce the number of samples because it was tested in the preliminary tests and showed good behavior. Fig. 4.21(a) shows the fiber 'A' and mixture No. 1, as expected, it improved the tensile strength with the increase of fiber content.

The indirect tensile method is not a reliable testing procedure to measure the transversal displacement and the strain within the specimen.

Table 4.15: Indirect tensile strength data summary.

Specimen	Tensile Stress (MPa)	Compressive Strength (MPa)	Tensile/ Compressive (%)
M01	2.87	34.80	8.26
M02	3.75	33.30	11.26
M03	3.85	32.10	11.99
M04	3.25	32.60	9.95
M05	3.69	32.30	11.42
M06	3.32	33.20	9.99
M07	3.23	25.90	12.45
M08	2.62	23.40	11.21
M09	2.60	21.30	12.22
M10	2.40	18.10	13.28
M11	2.34	19.20	12.19
M12	2.34	18.90	12.38
M13	3.92	33.40	11.73
M14	3.12	33.40	9.33
M15	2.93	30.70	9.54
M16	2.63	22.80	11.54
M17	2.93	24.20	12.12
M18	2.79	23.40	11.93
M19	2.40	18.10	13.28
M20	2.27	19.30	11.77
M21	2.42	18.90	12.83

4.5. Beam pushover test

Four beams were tested until failure to assess the influence of fiber content on both, flexural and shear behavior. Two of those beams were designed to fail in flexural mode (Fig. 4.25), and the following two were designed to fail in shear mode (Fig. 4.26). All beams were assembled using1 $\phi 8$ A630-420H steel bars both for stirrups and flexural rebar, the stress-strain curve and its mechanical properties is shown in Fig. 4.7 and Table 4.10, respectively. Just two mixtures were used for all beams: coarse aggregate concrete and 1.23% PVA content concrete with fiber 'A', mechanical properties can be found in Table 4.2. Fig. 4.24 shows the concrete compressive stress-strain curve used, for both cases, plain concrete representing concrete with 0% PVA content and concrete w/PVA which represents concrete with 1.23% PVA content, its main parameters were extracted in the section 4.4.3 and are described in the Table 4.16.

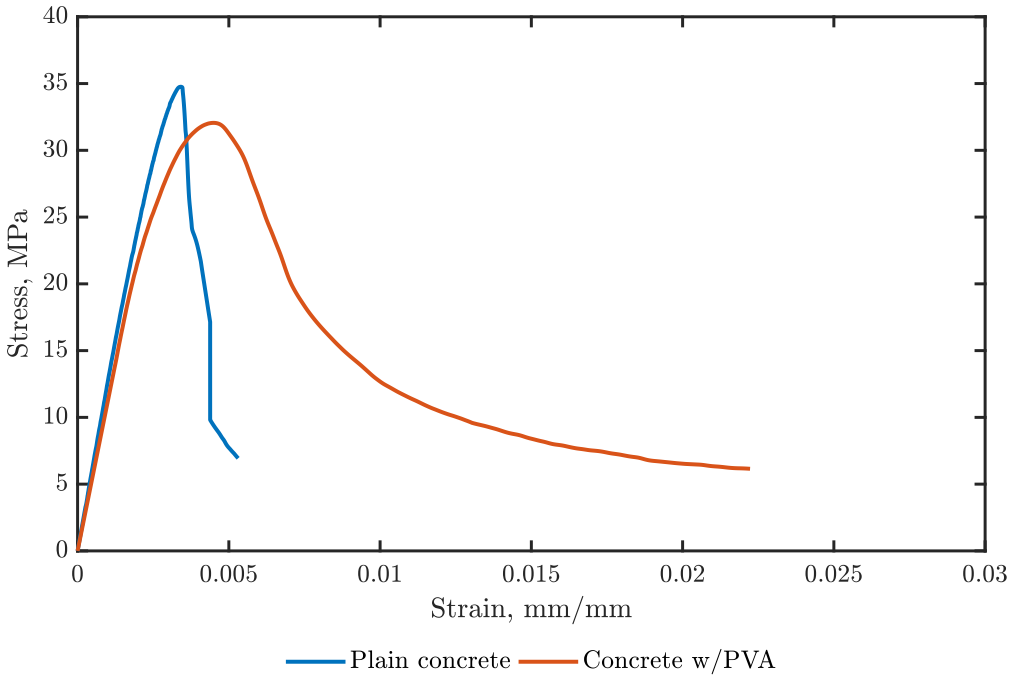

Figure 4.24: Concrete stress-strain curve.

Table 4.16: Concrete's main parameters for pushover mixture.

Specimen	Peak Stress (MPa)	Strain at peak (-)	Stress at max. strain (MPa)	Max. Strain (-)
Plain concrete	34.80	0.00341	6.90	0.00531
Concrete w/PVA	32.10	0.00450	6.10	0.02223

The two long beams are 1900 mm long with a cross-section of 140x200 mm, supported on two simple supports spaced at 1700 mm. On the other hand, the two short beams are

1200 mm long with the same cross-section as the long beams, simple-supported on both ends separated by 1000 mm. Both types of beams have two longitudinal $\phi 8$ steel rebars in the bottom and two $\phi 8$ steel rebars at the top to hold the stirrups. Long beams meet the tensile minimum reinforcement and shear reinforcement, but short beams does not meet the shear reinforcement, due to the lack of stirrups.

The load was applied in two points at 200 mm from the center and monotonically incremented using a rigid beam of 400 mm long to distribute the load.

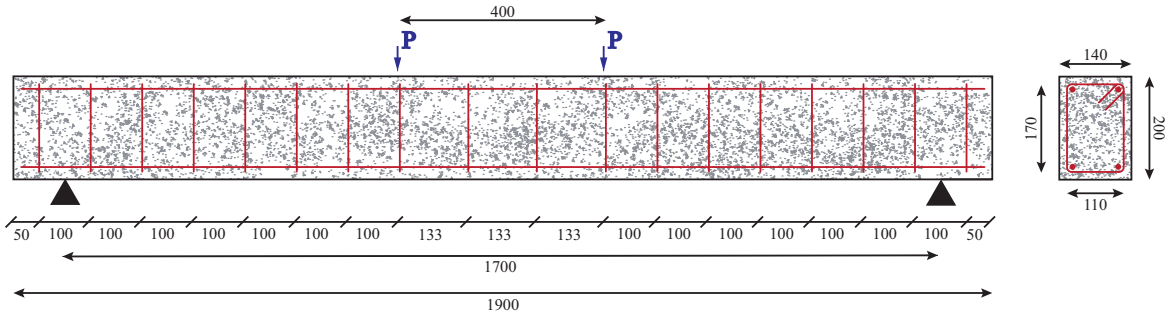

Figure 4.25: Long beam reinforcement blueprint, not a scale.

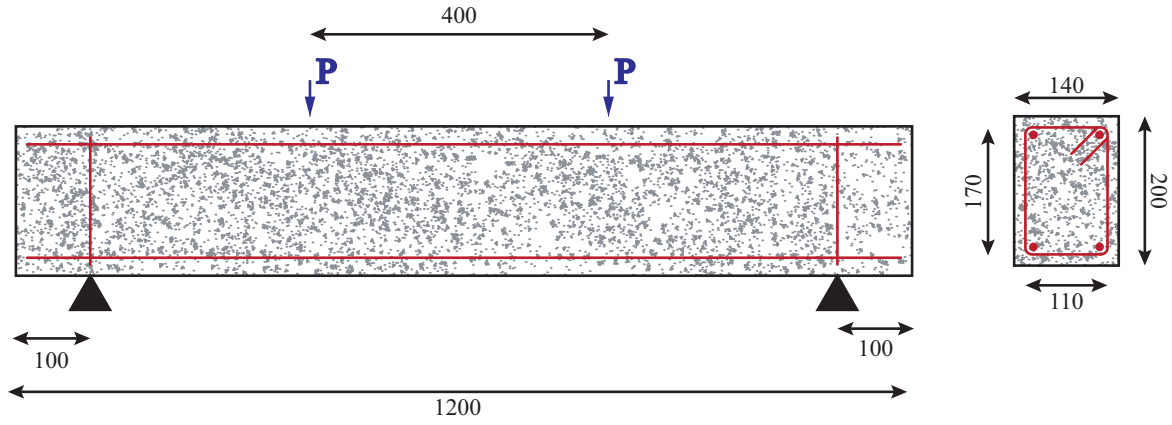

Figure 4.26: Short beam reinforcement blueprint, not a scale.

Figs. 4.28 and 4.27 shows the position of all instruments used for testing. Different instrument arrangements were used, 4.28 was used for short beams and 4.27 was used for long beams. The main difference between both is the placement of the main measurement instrument. On the shear beam, the instrument is placed above the rigid beam where the load is distributed. On the other side, for the flexural beam, its placement is at the center of the beam, 15 cm from the bottom, as shown in Fig. 4.27. The placement criteria was to capture the vertical displacement avoiding interference with the camera shots because those pictures will be used in the following section to perform a DIC analysis.

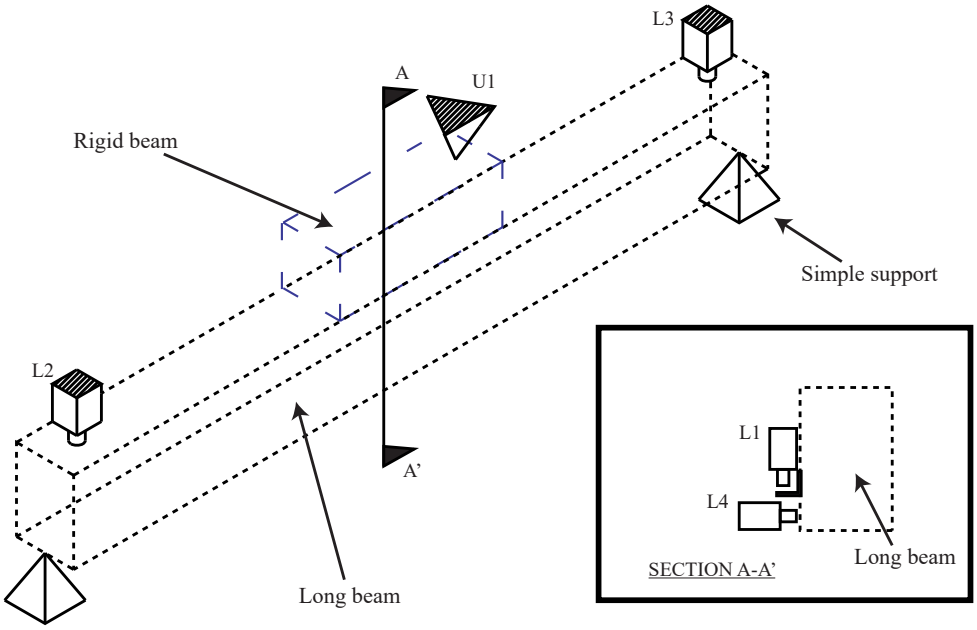

Figure 4.27: Long beam instrument placement, where 'U' represents ultrasonic sensor and 'L' denotes LVDTs.

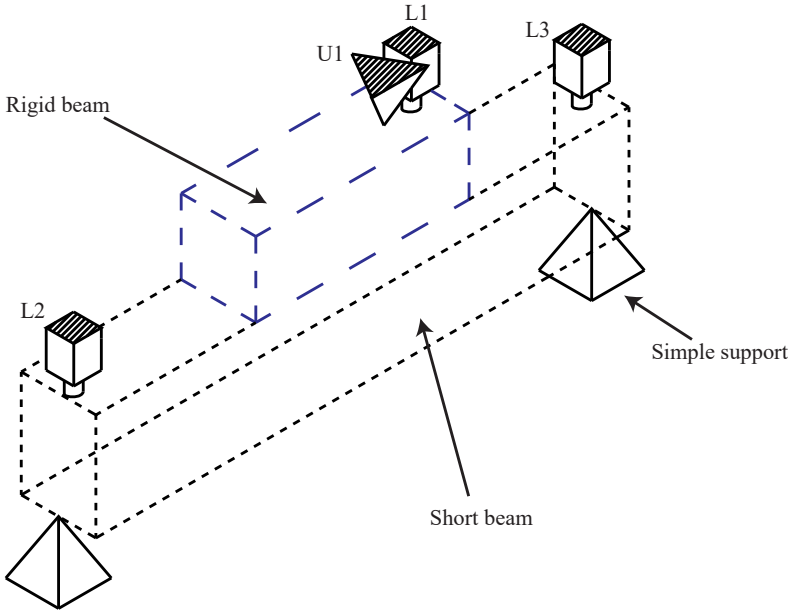

Figure 4.28: Short beam instrument placement, where 'U' represents ultrasonic sensor and 'L' denotes LVDTs.

The final pushover test montage for the flexural beams and shear beams are shown in Figs. 4.29- 4.30.

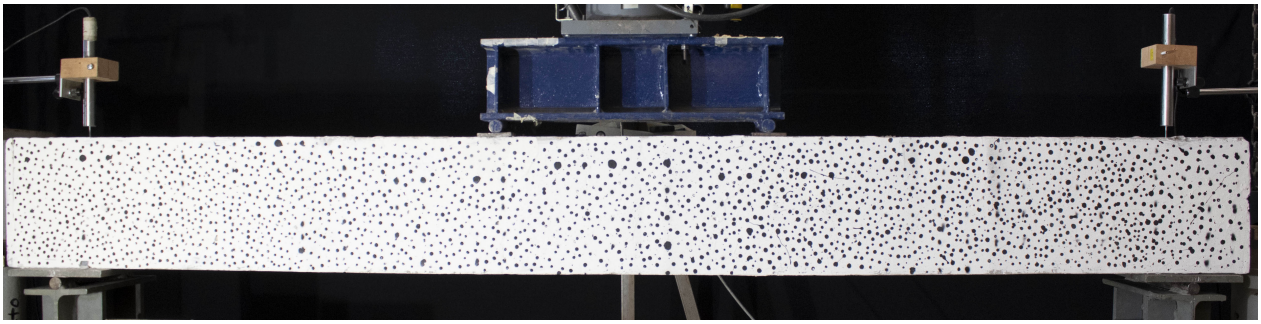

Figure 4.29: Flexural beam setup pushover test.

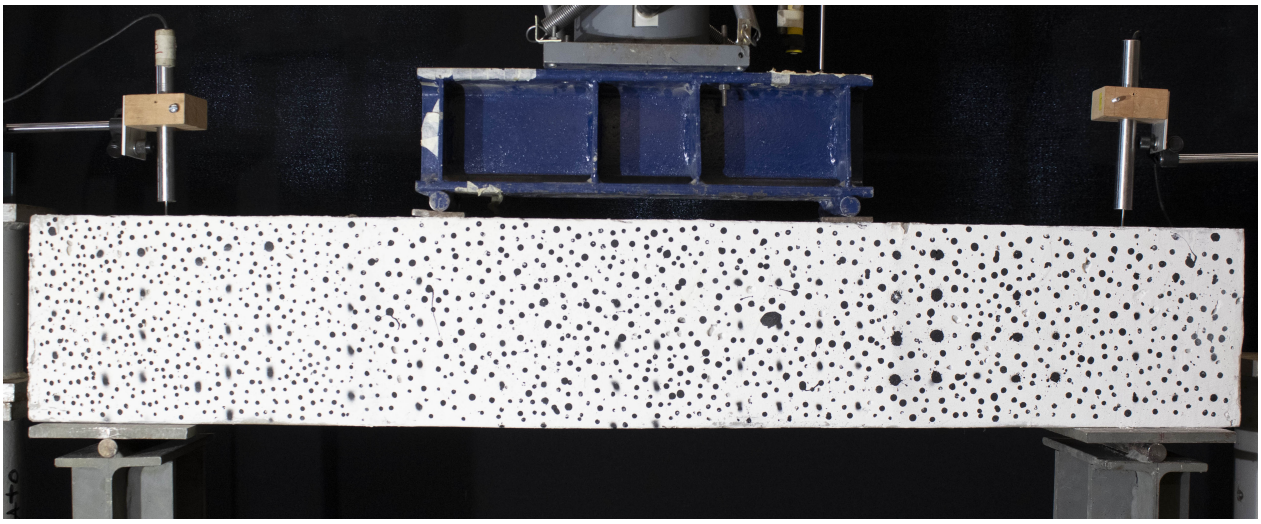

Figure 4.30: Shear beam setup pushover test.

4.5.1. Ultimate and cracking strength

To ensure that the data extracted from the following test is correct, a simple capacity analysis was made following the ACI318-19 procedure (318, 2019). The cracking load and ultimate load extracted from the analysis are tabulated in Table 4.17.

Table 4.17: Cracking and ultimate load, (318, 2019).

Case	Long beam, kgf		Short beam, kgf		Shear strength, kgf
	M_{cr}	M_u	M_{cr}	M_u	V_c
Plain concrete	873.8	2999.3	1893.3	6498.6	4953.0
w/PVA fiber	1173.9	2988.8	2543.6	6475.7	4757.6

4.5.2. DIC beam analysis

DIC analysis was applied to assess both the displacement and strain field along the four beams described in the section before using a nonlinear image tracking algorithm made by Blaber et al. and explained in Chap. 3. The parameters used to perform the DIC analysis using Ncorr and MATLAB® are presented in Table 4.18. There are a difference of six second between shots.

Table 4.18: DIC analysis parameters.

Parameter	Camera
Subset Radius	100
Subset Spacing	20
Diff Norm C/O	1.00E-06
Iteration #C/O	50
Total Threads	4
Step Analysis	Checked
Auto Propagation	Checked
Subset Truncation	Checked
Strain Radius	5
Subset Truncation Strain	Checked

4.5.2.1. Error analysis

It is important to know the intrinsic error produced by using Ncorr to measure the pixel displacement. In this particular case, the error associated with the measurement is the pixel-displacement relationship. There are two ways to reduce the pixel-displacement error: increasing the pixel density on the shot, i.e., the camera resolution; the second way is by reducing the focal distance to the object. In this research, the Canon® EOS Rebel T5 camera was used. It has an 18.0-megapixel image sensor and a focal distance to the object of 1.5 m approximately. The pixel-displacement ratio used on each beam is shown in Table 4.19.

Table 4.19: Pixel-displacement used.

Specimen	mm/px
Short beam 0% FC	0.2349
Short beam 1.23% FC	0.2368
Long beam 0% FC	0.3805
Long beam 1.23% FC	0.3754

*FC: Fiber content.

To measure the error associated with the measurement, it is necessary to take two consecutive images at an undisturbed state, with no outside changes. Both strains and displacement must not have variations. Thus, changes in the strains and displacements values imply an error that must be addressed. After running the analysis, Ncorr shows the beam strain field

in both vertical and horizontal directions. Fig. 4.31 depicts the image obtained by running the error analysis on each beam for vertical displacement. Table 4.20 summarizes the maximum displacement error obtained for each beam and Table 4.21 shows the maximum error associated with each beam.

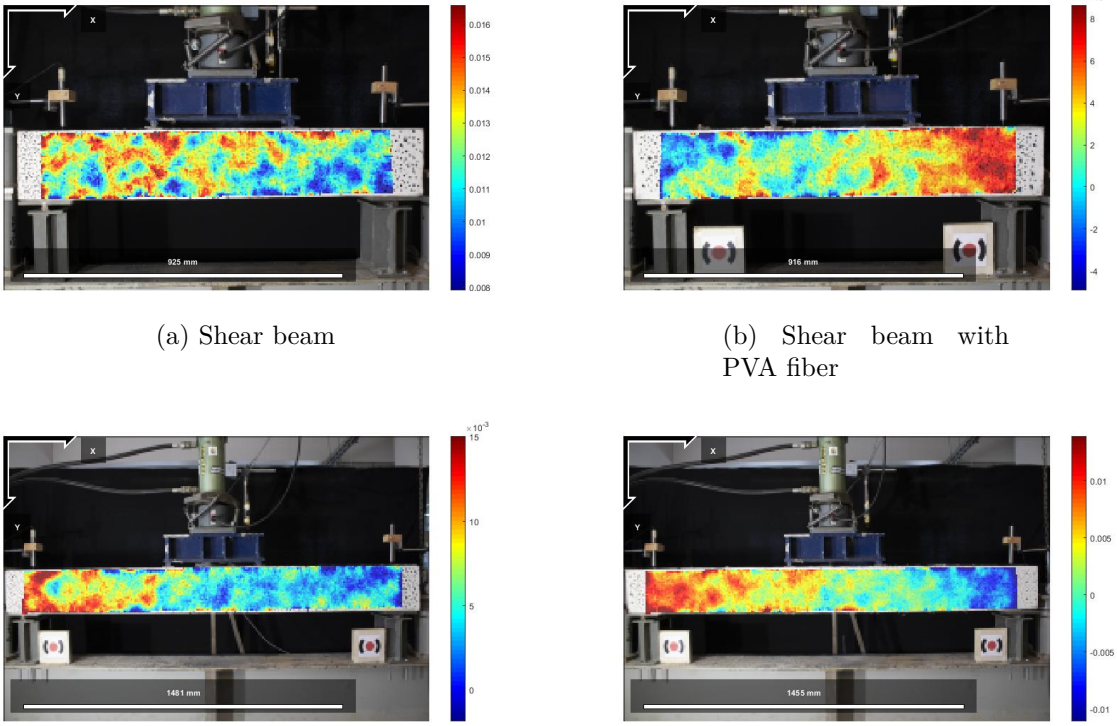

(a) Shear beam

(b) Shear beam with PVA fiber

(c) Flexural beam

(d) Flexural beam with PVA fiber

Figure 4.31: Deflection error for all beams, unit mm.

Table 4.20: Displacement error.

Displacement	Short Beam (mm)		Long Beam (mm)	
	0% PVA	1.23% PVA	0% PVA	1.23% PVA
U	0.0112	0.0231	0.0183	0.0241
V	0.0207	0.0196	0.0255	0.0381

Table 4.21: Strain error.

Strain	Short Beam (-)		Long Beam (-)	
	0% PVA	1.23% PVA	0% PVA	1.23% PVA
ε_{xx}	0.0002	0.0003	0.0002	0.0004
ε_{xy}	0.0002	0.0003	0.0002	0.0002
ε_{yy}	0.0005	0.0004	0.0004	0.0003

As it can be noticed by the data listed before, the magnitude of the maximum displacement error obtained by the analysis is approximately 0.038 mm (Table 4.20). Nonetheless, the displacement data will be use in further analysis to fix the P-Δ diagrams with the data obtained by the DIC.

4.5.2.2. DIC strain data

With the error addressed in the section before, the DIC analysis is performed following the steps listed in Appendix B. Ncorr provides both displacement and strain matrices at each frame to obtain the displacement and strain at any given time. The strain fields not found in this section are shown in Appendix D.

4.5.2.2.1. Shear beam

Figs. 4.32 and 4.33 show the strain field obtained by using a DIC analysis provided by Ncorr. In the shear beam with plain concrete, it can be noticed that as the load increases, that the shear cracks increases as well (Fig. 4.32), changing the behavior of flexural cracks developed at first load steps (Fig. 4.34). The peak ε_{xx} strain in Fig. 4.34 is due to the shear crack failure because the pixels surrounding it tend to move, and the consecutive images capture it. However, it does not represent the material strain field at the failure.

The shear failure of the short beam with plain concrete (Fig. 4.32) was expected due to the beam design with no stirrups and a shear length of 300 mm, which is the length between the support and the loading rigid beam, and $d = 160$ mm, defined as the length to the steel rebars. However, the flexural failure seen on short beam with 1.23% PVA content was not expected (Figs. 4.33 and 4.35).

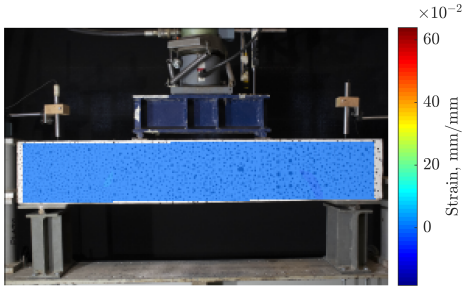

(a) Deflection = 6.7 mm.

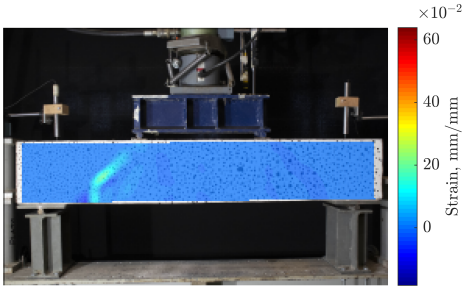

(b) Deflection = 27.9 mm.

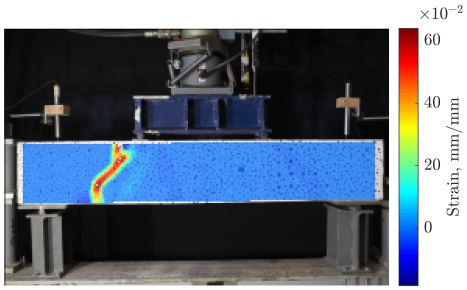

(c) Deflection = 37.6 mm.

Figure 4.32: Shear strain ε_{xy} development over time, short beam with plain concrete.

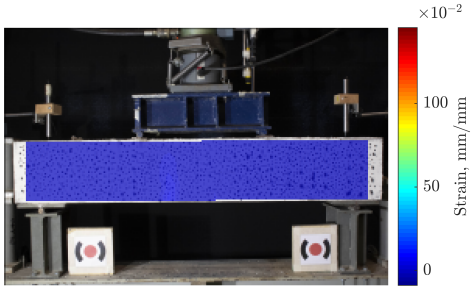

(a) Deflection = 5.6 mm.

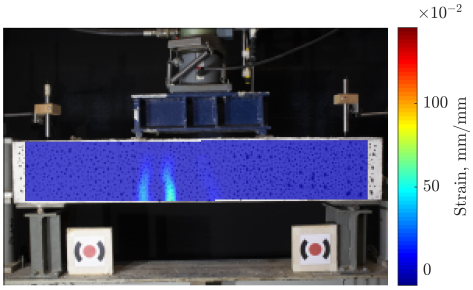

(b) Deflection = 37.3 mm.

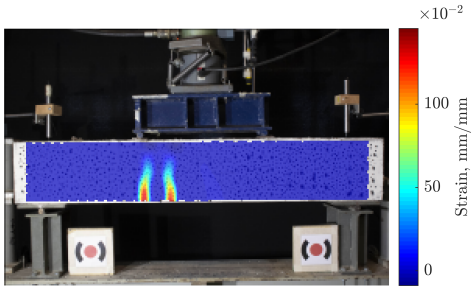

(c) Deflection = 72.8 mm.

Figure 4.33: Longitudinal strain ε_{xx} development over time, short beam with PVA.

Due to the failure mode, Fig. 4.32 shows the ε_{xy} strain field because it can clearly show the crack development. On the other hand, Fig. 4.33 shows the ε_{xx} or longitudinal strain field because it illustrates better the longitudinal crack development. It can be observed that at early deflections, both short beams showed cracks that tented to develop a flexural behavior (Figs. 4.34 and 4.35). However, the flexural failure only developed in the short beam with 1.23% PVA content, concentrating the cracks in only two points, closing the remaining cracks (Fig. 4.35 at deflection = 72.8 mm).

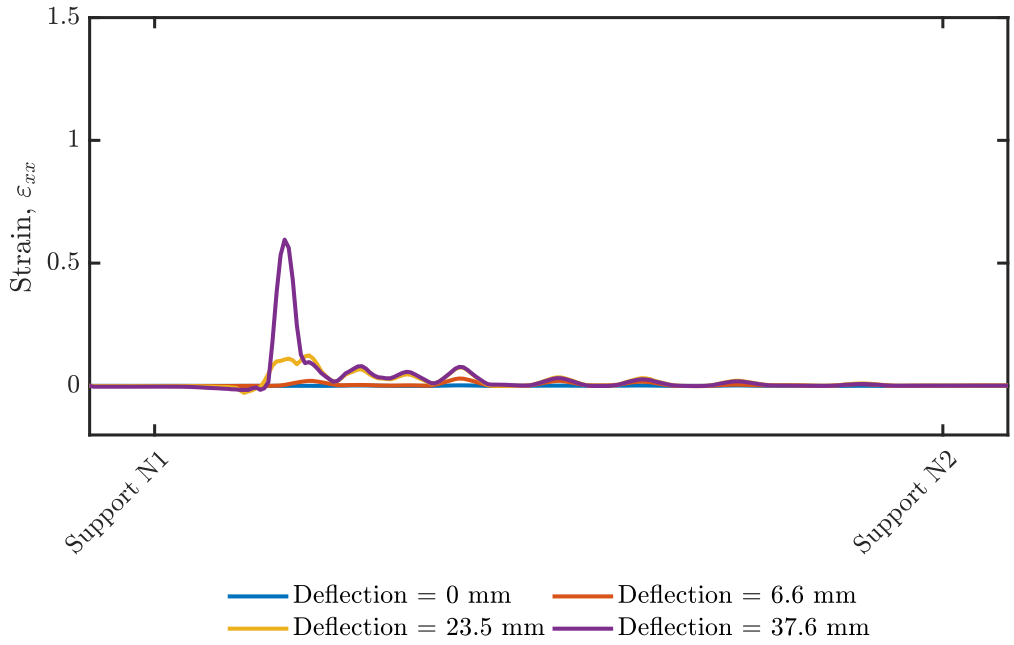

Figure 4.34: Longitudinal strain ε_{xx} plane at the most tensioned plane over time, short beam.

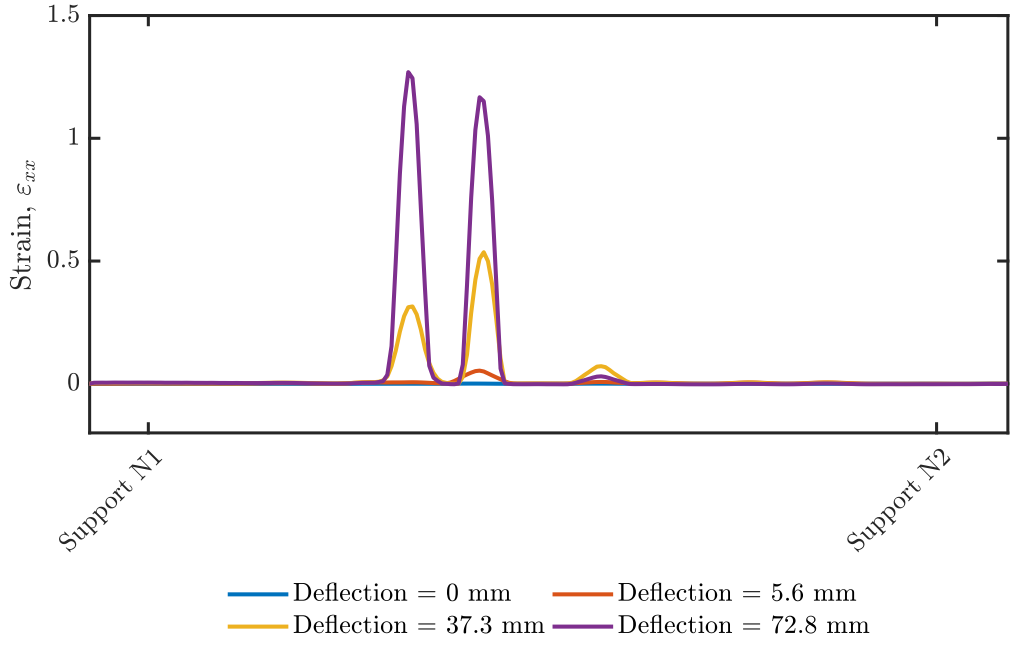

Figure 4.35: Longitudinal strain ε_{xx} plane at the most tensioned plane over time, short beam with PVA.

4.5.2.2.2. Flexural beam

Figs. 4.36 and 4.37 show the strain field obtained by using a DIC analysis provided by Ncorr. Both beams, in this case, failed in the flexural mode as designed. However, the long beam with no PVA fiber presented a greater vertical displacement than the long beam with PVA fiber content, and also, it had a greater plastic hinge or crack distribution (Figs. 4.36

and 4.37). Thus, in this particular case, PVA fiber incorporation might not increase the displacement capacity on flexural members' element. However, it does increase the member's load capacity, shown in Fig. 4.44.

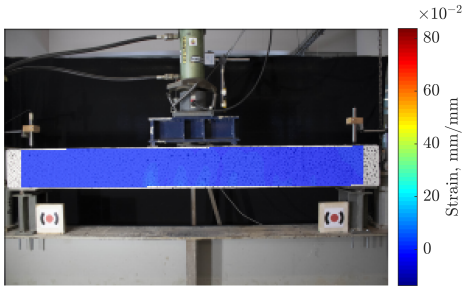

(a) Deflection = 28.4 mm.

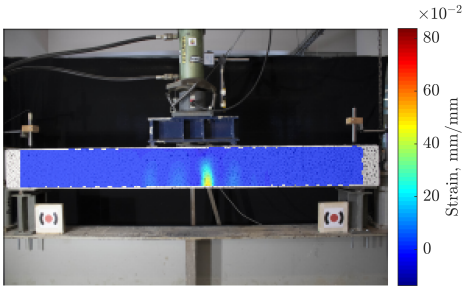

(b) Deflection = 105.8 mm.

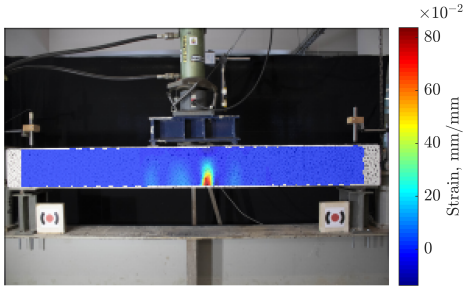

(c) Deflection = 145.9 mm.

Figure 4.36: Longitudinal strain ε_{xx} development over time, long beam.

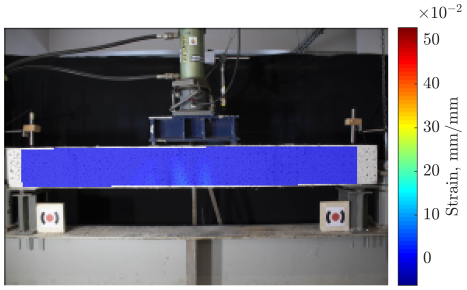

(a) Deflection = 19.8 mm.

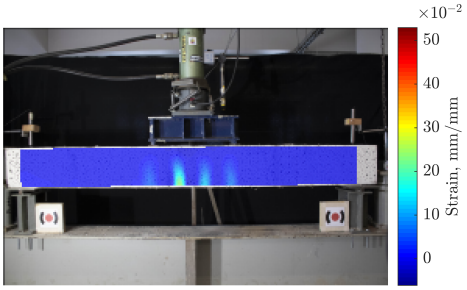

(b) Deflection = 68.3 mm.

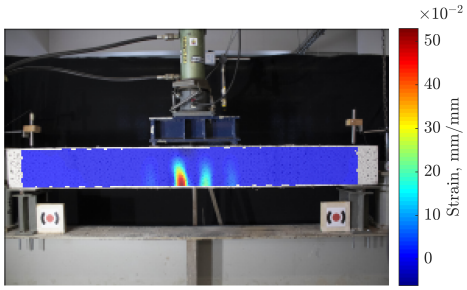

(c) Deflection = 117.3 mm.

Figure 4.37: Longitudinal strain ε_{xx} development over time, long beam with PVA.

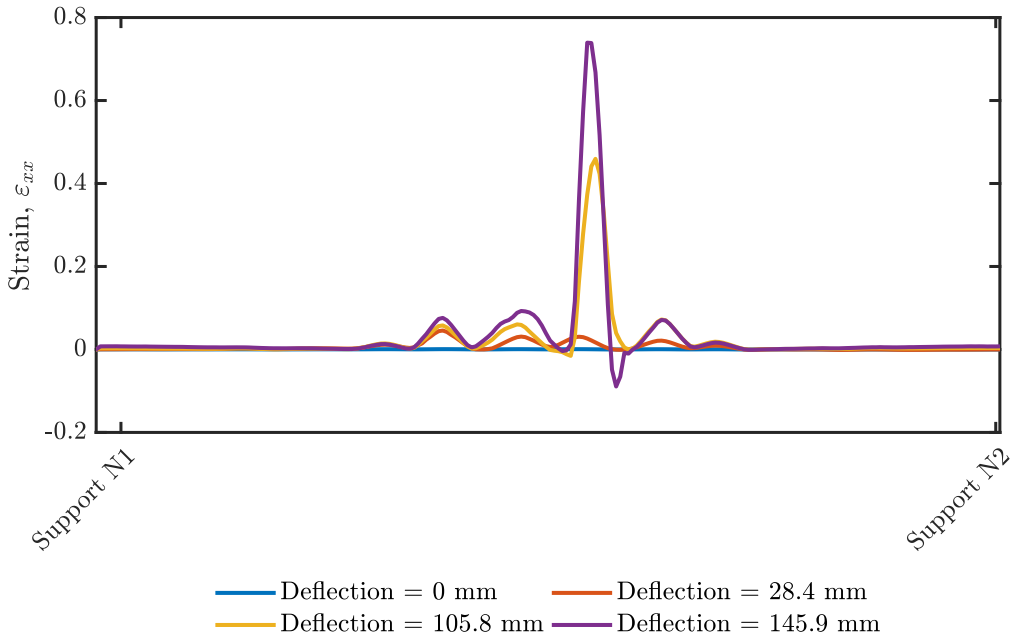

Figure 4.38: Longitudinal strain ε_{xx} plane at the most tensioned plane over time, long beam.

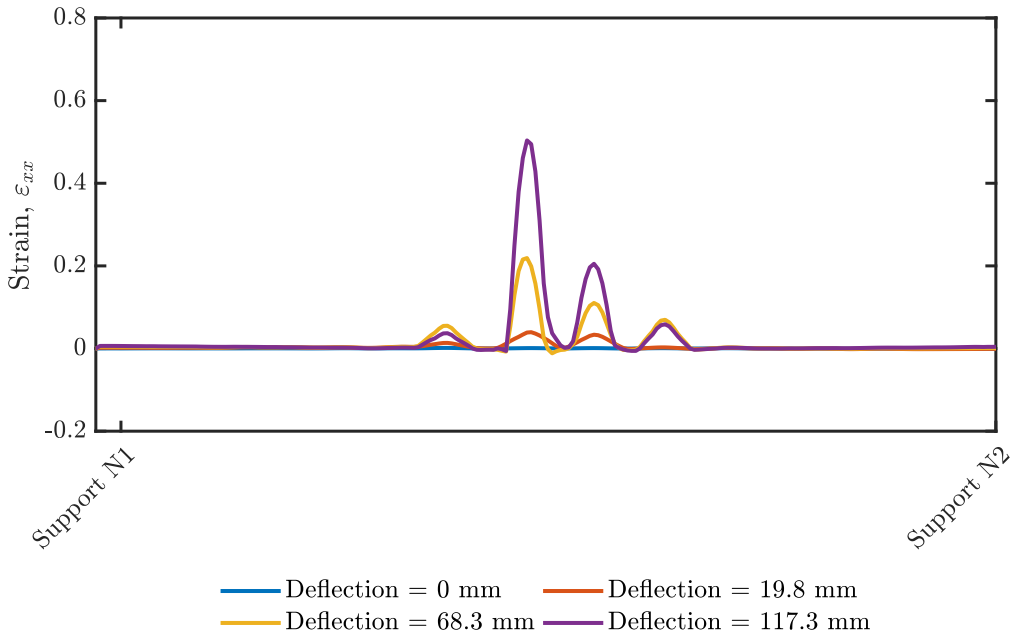

Figure 4.39: Longitudinal strain ε_{xx} plane at the most tensioned plane over time, long beam with PVA.

4.5.2.3. DIC displacement data

Ncorr, within the data provided, gives a pixel displacement matrix at each loading picture step. Thus, it is possible to extract the displacement variation at any beam point for each shot, knowing that the pictures were taken six seconds apart to create a P-Δ diagram, a superposition of the loading vector and displacement vector provided by Ncorr is needed. To achieve that, the sampling frequency of the cell load is 30 Hz or 30 samples per second.

Consequently, to overlap at the same sample rate, cell load data must be extracted every 180 data points to create a loading-displacement diagram. Assuming that at zero displacements, the loading process starts. The following P-Δ diagrams of each beam tested (Figs. 4.40 to 4.43) was extracted using the Ncorr algorithm. For each beam, the displacement at the bottom center pixel was extracted.

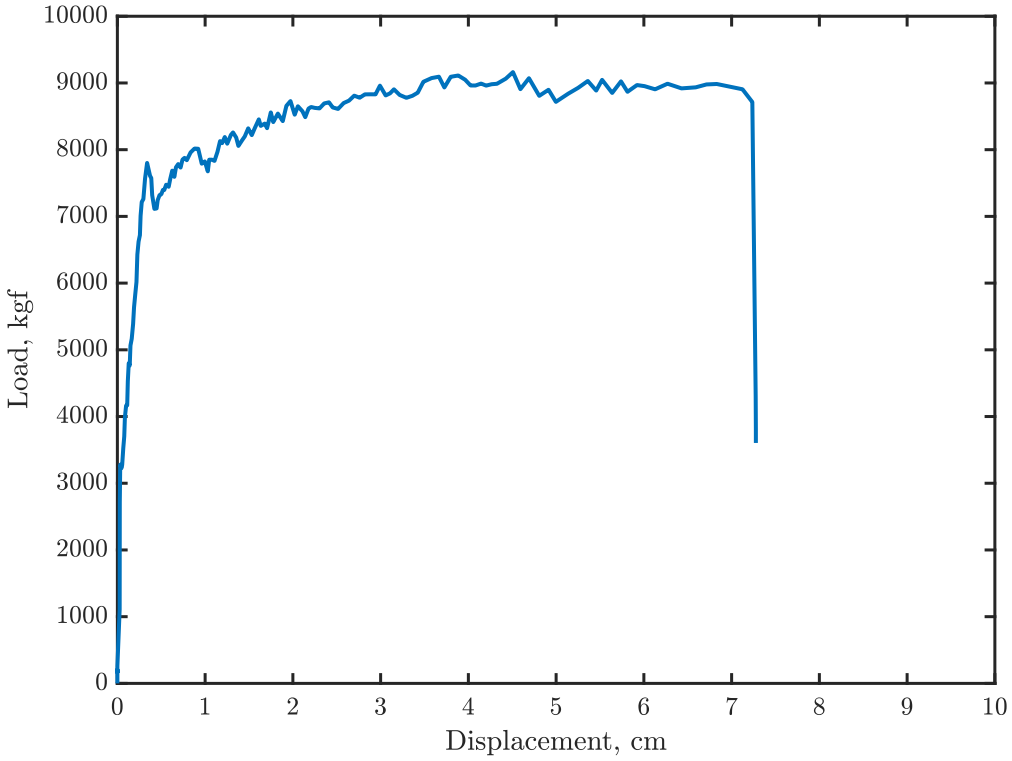

Figure 4.40: Short beam with PVA P-Δ diagram extracted by Ncorr.

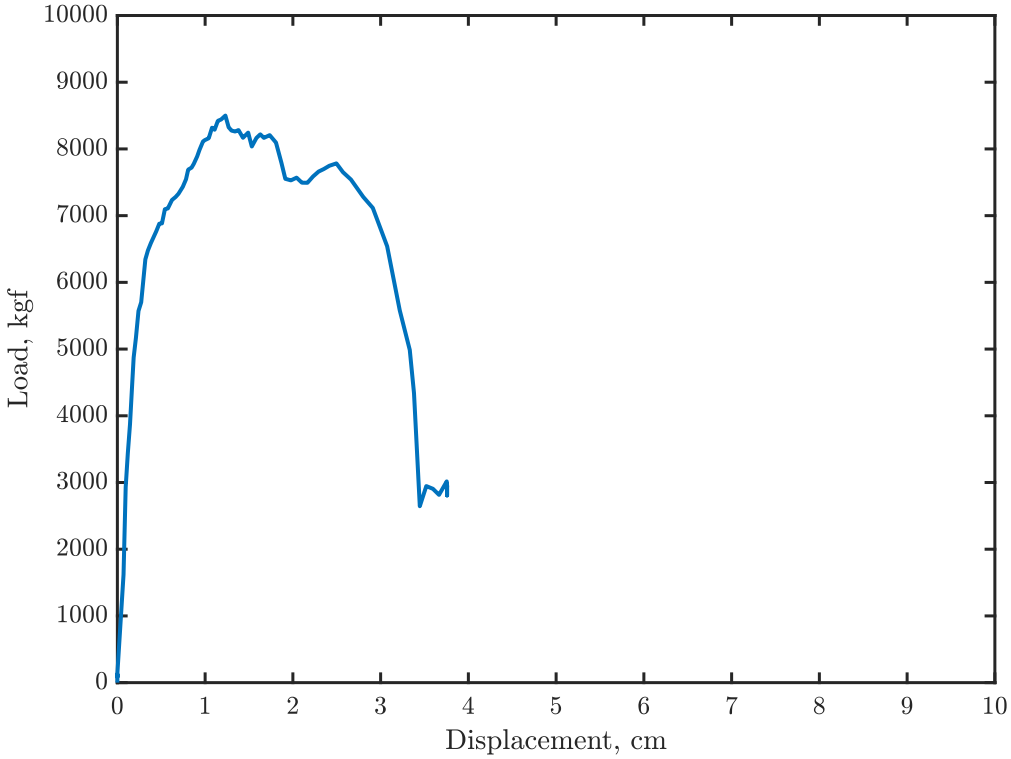

Figure 4.41: Short beam with plain concrete P-Δ diagram extracted by Ncorr.

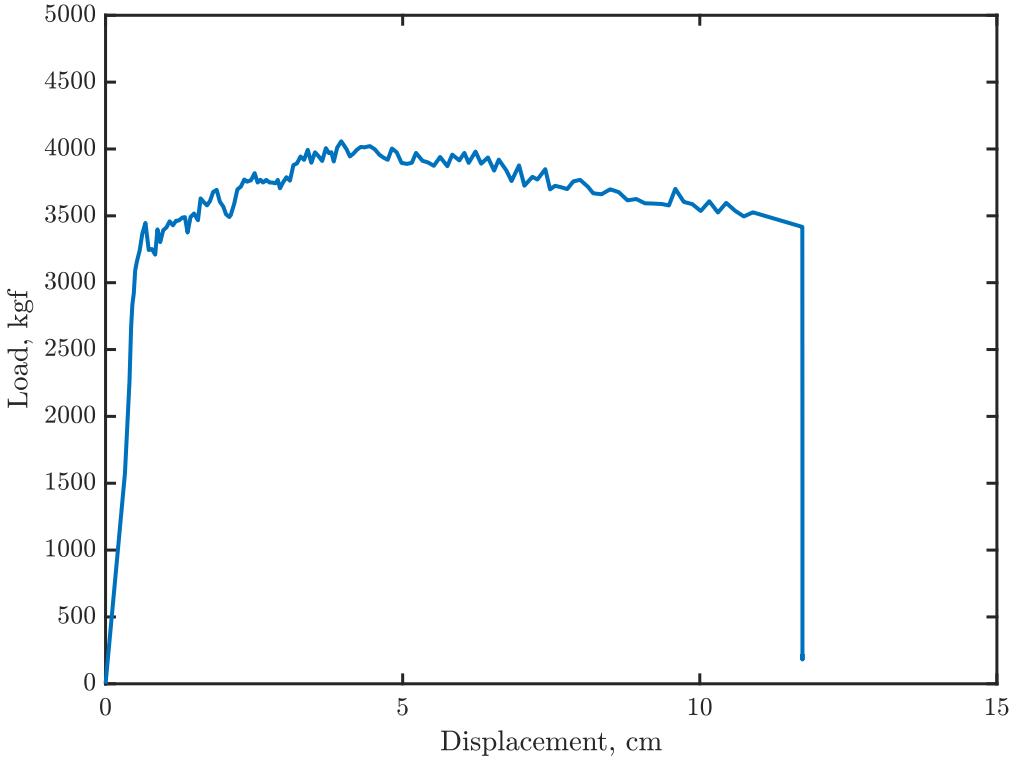

Figure 4.42: Long beam with PVA P-Δ diagram extracted by Ncorr.

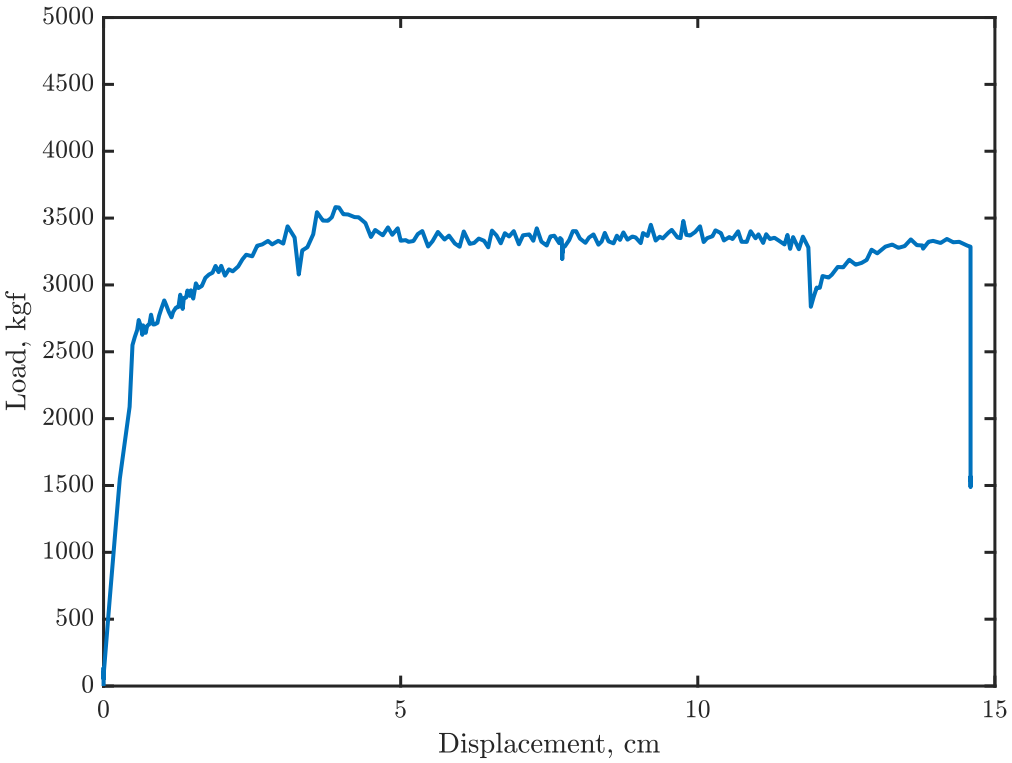

Figure 4.43: Long beam with plain concrete P-Δ diagram extracted by Ncorr.

4.5.3. Physical instruments

4.5.3.1. Flexural Beam

Fig. 4.44 shows the P-Δ diagram obtained by sensor U1. During the test of the plain concrete beam, due to the LVDTs' restricted measurement range, sensor L1, around 100 mm approximately, the deflection measurement could not be obtained during the final loading stage.

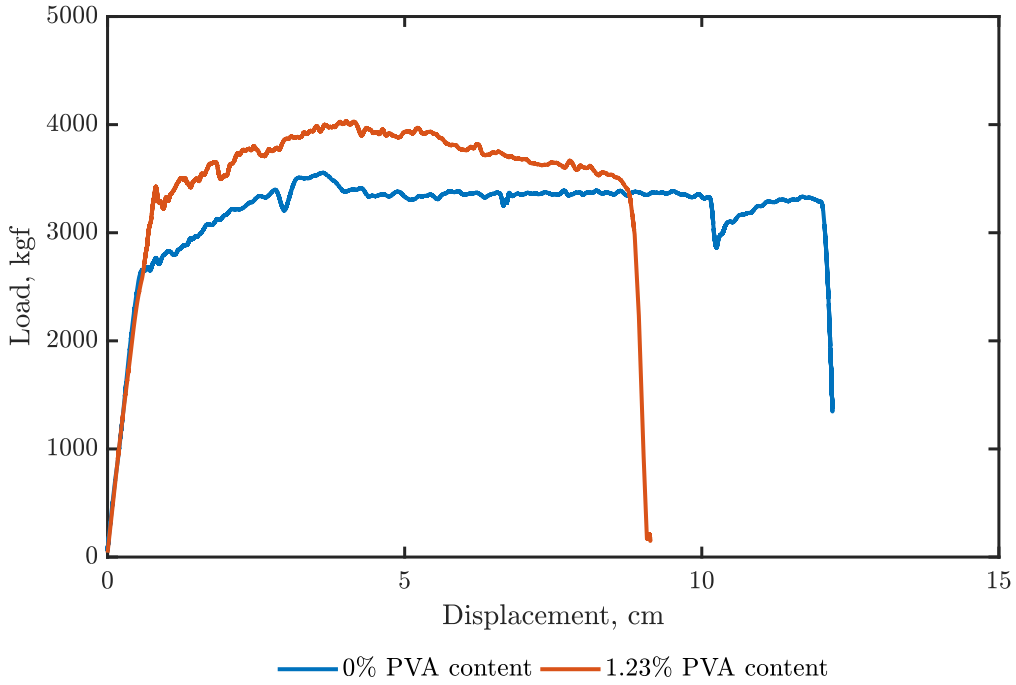

Figure 4.44: Flexural beam pushover curve for sensor U1.

Consequently, the flexural beams with 1.23% PVA content and 0% fiber content had a first peak load capacity of approximately 3,500 kgf and 2,800 kgf, respectively, and a top capacity of approximately 4,000 kgf and 3,500 kgf. In this particular case, the PVA fiber reinforced concrete showed a higher load capacity than the plain concrete beam. However, even though the PVA fiber beam had a higher load capacity, it presented a lower displacement capacity than the control beam. This can be due to many factors, such as aggregate distribution because cracks are produced between the aggregates in the cementitious matrix, therefore, if there is a large amount of aggregate in a particular place, it is easier for the crack to develop; voids inside the beam due to poor vibration; stresses distribution as the rigid beam rotates and produces an asymmetrical load, but mainly to the fiber distribution along the beam. It is known that fiber tends to produce voids inside the matrix by forming little nests in different beam locations.

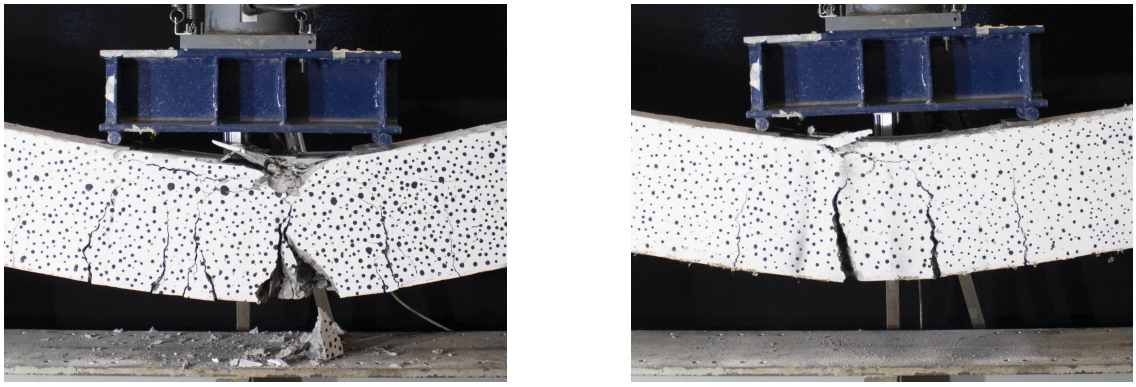

(a) 0% PVA content

(b) 1.23% PVA content

Figure 4.45: Long beam failure, center picture.

Fig. 4.45 depicts the failure mode for each long beam. As each beam had the same high support at the beginning of testing, it is visually noticeable that the PVA fiber reinforced concrete had a lower deflection than the control beam. It is also clearly represented that the cracks concentration is higher in the control beam than the PVA fiber beam. Higher crack distribution along the beam implies a higher deflection and a larger curvature due to the crack width is lower and contained in many cracks distributed.

4.5.3.2. Shear Beam

Fig. 4.46 shows the P-Δ diagrams obtained by the sensor L1 (Fig. 4.28).

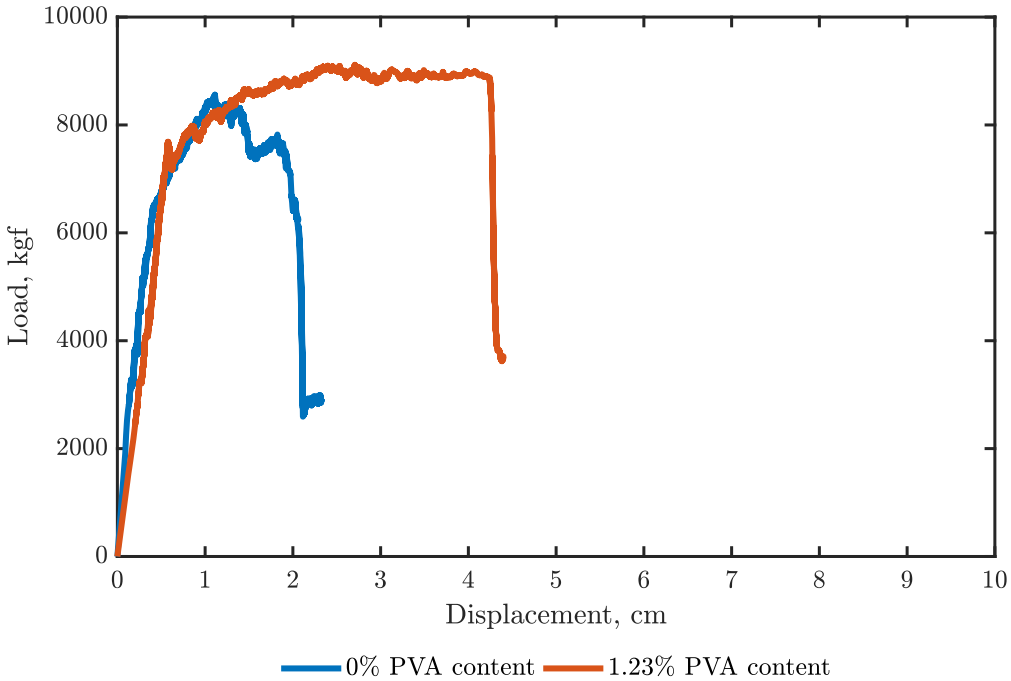

Figure 4.46: Short beam pushover curve for sensor L1.

The shear beams with 1.23% PVA content and 0% fiber content had a first peak load capacity of approximately 8,000 kgf and 6,500, respectively, and a top capacity of approximately 9,000 kgf and 8,500 kgf. PVA fiber reinforced concrete showed a higher load capacity and deflection than the plain concrete beam, reaching up to 480 mm. The curves differences are negligible, because both distance measurement instruments were placed at the same location, above the rigid beam.

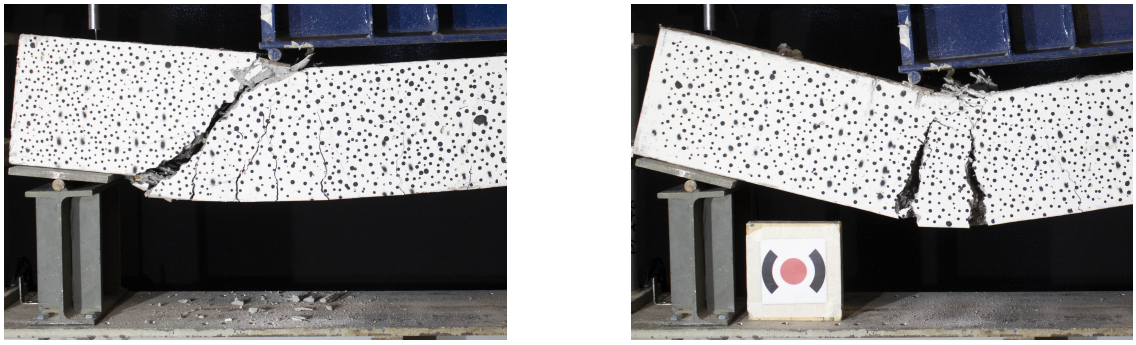

(a) 0% PVA content

(b) 1.23% PVA content

Figure 4.47: Short beam failure, left side.

Fig. 4.47 shows the failure mode for each short beam tested. It can be noticed that each beam had a totally different failure mode, the 0% PVA content beam (Fig. 4.47) presented a shear crack of 45° as expected. However, the 1.23% PVA content beam (Fig. 4.47) changed its failure mode into flexural. This is a huge improvement for short beam design, avoiding the shear failure by switching it to flexural, a non-explosive failure just by adding the right amount of PVA fiber into de mixture.

4.5.4. Measurement comparison

The displacement obtained by Ncorr for short beams depicted in Figs. 4.48 and 4.49, is put against the P-Δ curves obtained by the physical instrument such as Ultrasonic sensor and LVDTs. The displacement magnitude obtained by Ncorr is bigger due to the LVDTs and ultrasonic sensors' placement at the top of the rigid beam (Fig. 4.28), causing that the data extracted, such as the initial stiffness and displacement were influenced by the rigid beam rotation as the loading increased.

On the other hand, in the case of long beams (Figs. 4.50 and 4.51), the displacement obtained is also bigger for both tests. However, the reason for that is different compared to the short beams. In this particular case, the LVDTs were placed at the same spot as the Ncorr displacement data was extracted, but as the deflection increased, LVDTs due to the large displacement were unable to measure the displacement thanks to the limited range measurement. Thus, the initial stiffness of the data extracted with LVDTs and Ncorr is approximately the same, but compared to the ultrasonic sensors, it differs due to the placement of the sensor above the rigid beam, same reason that the short beams.

The following figures contrast the three measurement methods, side by side.

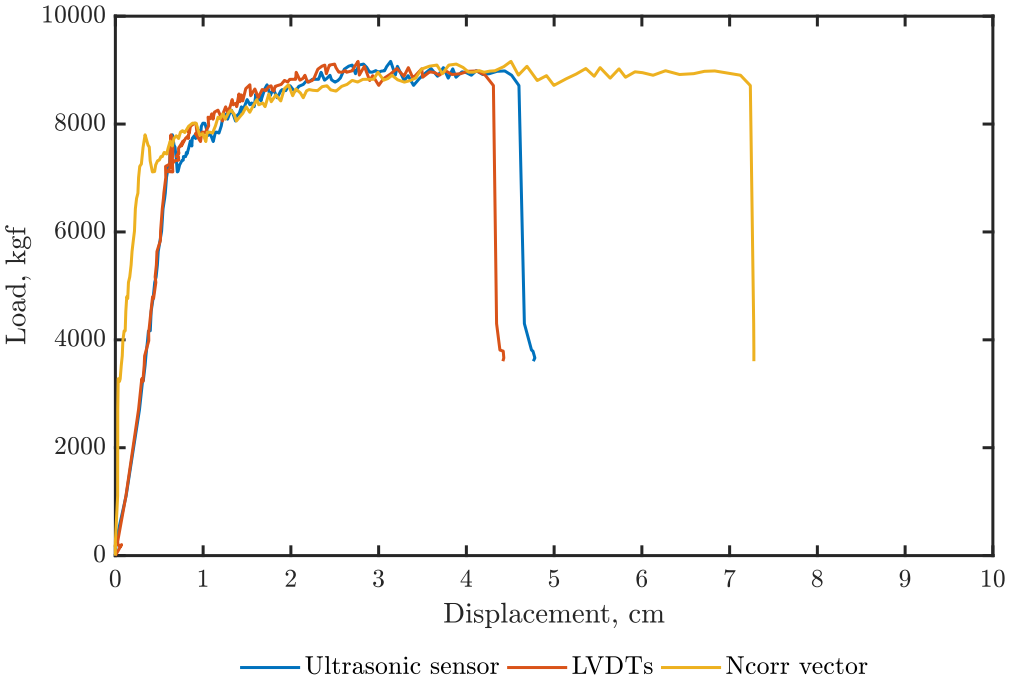

Figure 4.48: Short beam with PVA P-Δ diagram comparison with LVDTs and ultrasonic sensors.

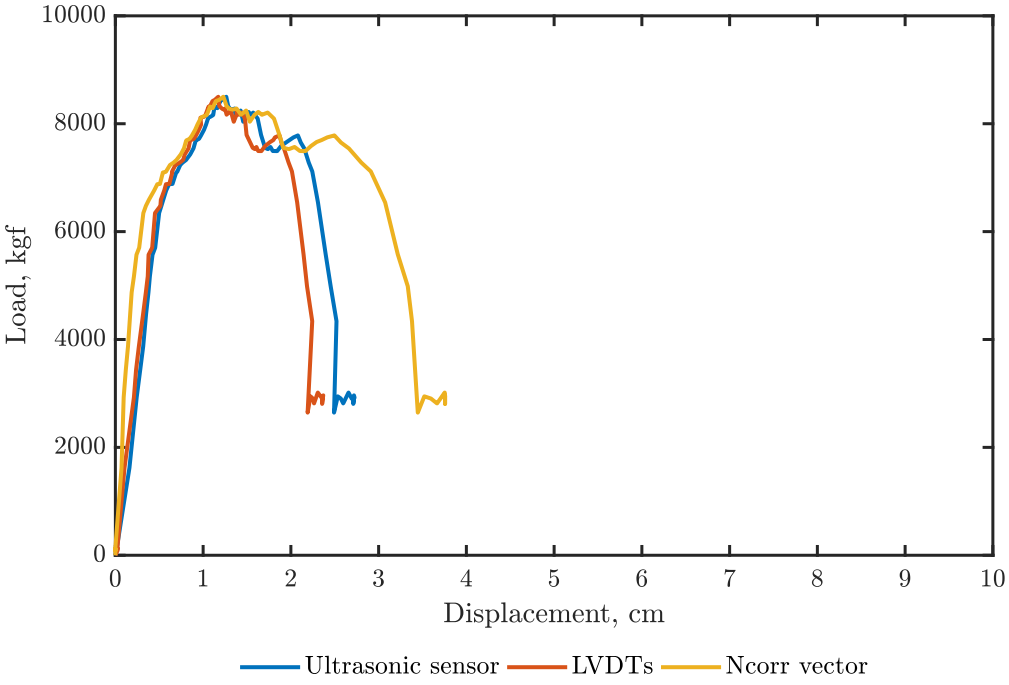

Figure 4.49: Short beam with no PVA P-Δ diagram comparison with LVDTs and ultrasonic sensors.

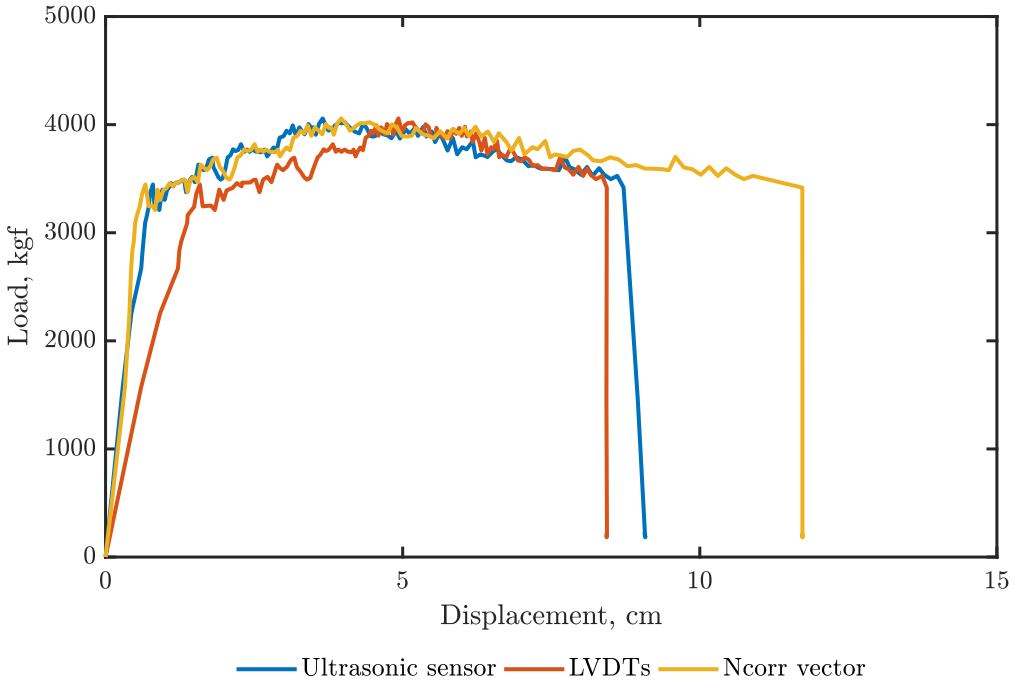

Figure 4.50: Long beam with PVA P-Δ diagram comparison with LVDTs and ultrasonic sensors.

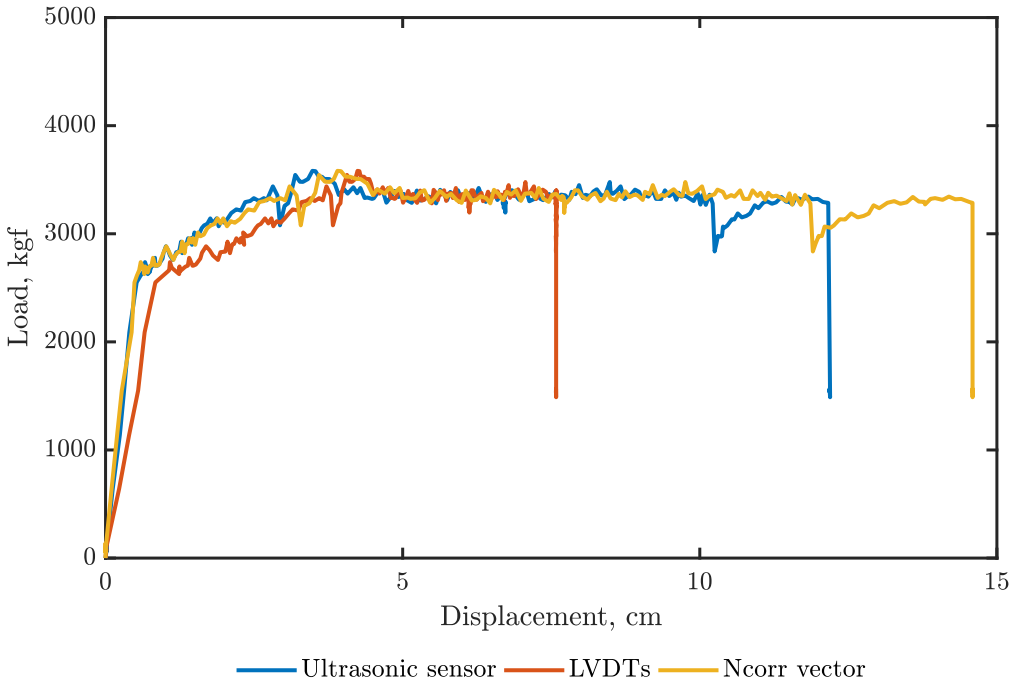

Figure 4.51: Long beam with no PVA P-Δ diagram comparison with LVDTs and ultrasonic sensors.

Therefore, the Ncorr displacement data is more reliable than the other instruments due to the displacement position of the data extracted. Comparing the P-Δ curves with the displacement vector obtained by Ncorr for each set of tests, Fig. 4.52 and 4.53 shows the global response of the long beams and short beams, respectively. These are the final P-Δ

diagrams which will be used for the modeling comparison.

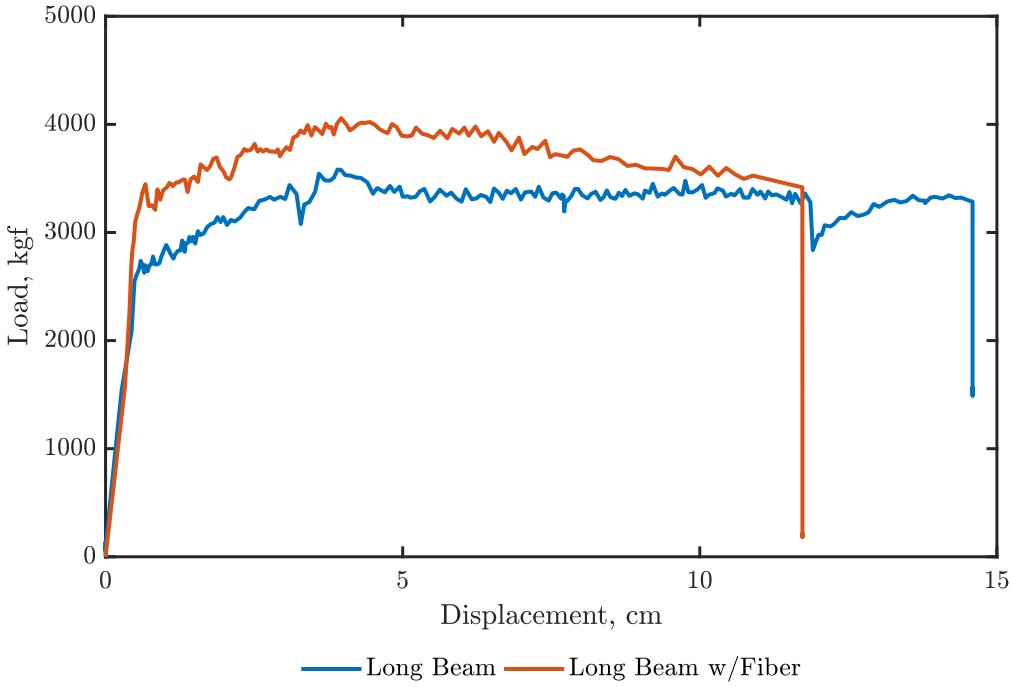

Figure 4.52: Comparison of both long beam diagrams obtained by Ncorr.

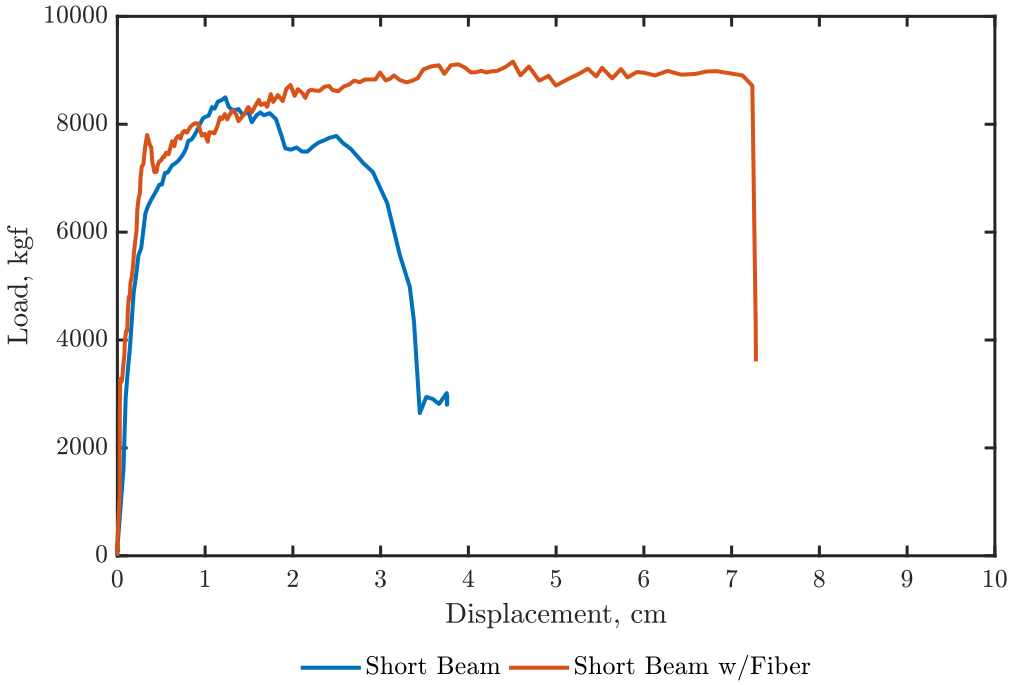

Figure 4.53: Comparison of both short beam diagrams obtained by Ncorr.

Chapter 5

Beam analytical model

After obtained the P-Δ curve in the last section by testing both short and long beams, a computational analytical model was assembled to replicate the PVA concrete beam pushover behavior acquired in the laboratory.

A pushover analytical model was calibrated using OpenSees material called E-SFI, due to the beam symmetry, just half of the beam was modeled to reduce computational loading, considering a central support that only restrained node rotation. Concrete compression constitutive stress-strain curve was previously obtained in Section 4.4.3 for both plain and PVA concrete, as well as steel tensile constitutive stress-strain curve obtained in Section 4.2.

Before the main model details, it is important to know the material constitutive models and parametrization used for both concrete and steel.

5.1. Material calibration

5.1.1. Reinforcing steel

The constitutive law used to assembly steel into the panel element was made manually following the shape of the tensile steel reinforcement bars curves. Assuming that the model is a pushover-type loading (single direction loading), there is no need to use cyclic constitutive models to capture the global element behavior. Thus, a single multi-linear and easy-implementation material model called 'ElasticMultilinear' will be used. Belarbi and Hsu points out that the real yield stress is an 86% of the nominal yield stress when the reinforcing bars are embedded into the concrete. Therefore, this behavior is assessed in the calibrated model.

Thus, performing a simple axial test, it is possible to plot the actual steel constitutive law calibrated for 'ElasticMultilinear', shown in Fig. 5.1.

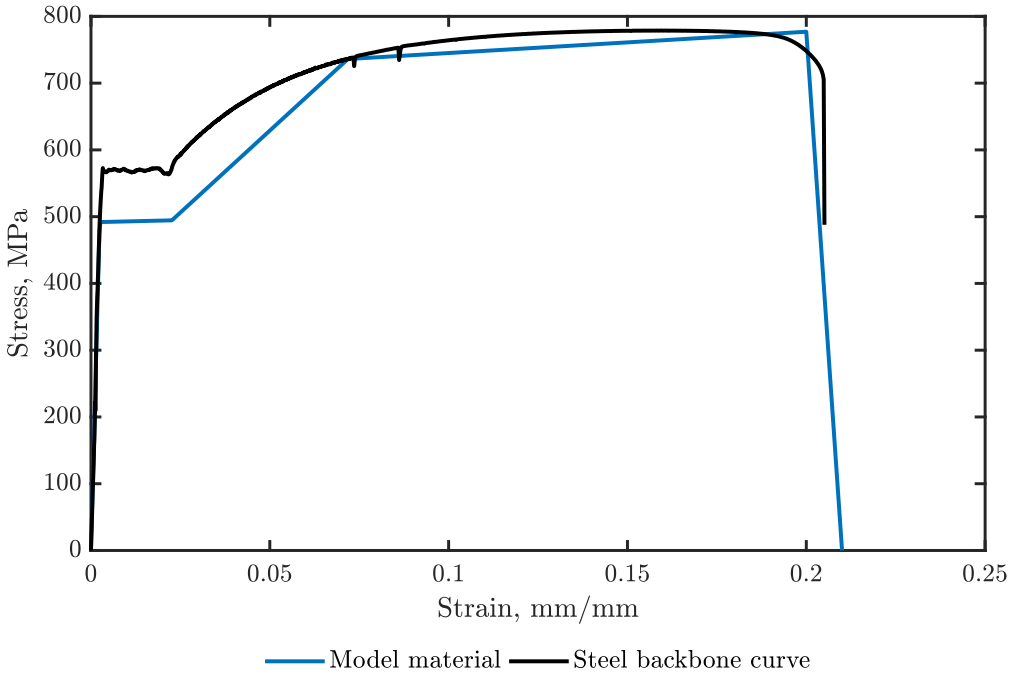

Figure 5.1: Calibrated tensile steel constitutive law - 'ElasticMultilinear'.

On the other hand, for compressive steel bars in which there are no stirrups in the central beam section, these bars might not reach the yield stress before bucking. To assess this behavior, the buckling model of reinforcing bars developed by Massone and Moroder was implemented using a bar diameter-length value of L/d = 16.6. Fig. 5.2 overlaps the actual steel tensile constitutive curve with the steel bucking effect obtained using the Massone and Moroder calibration.

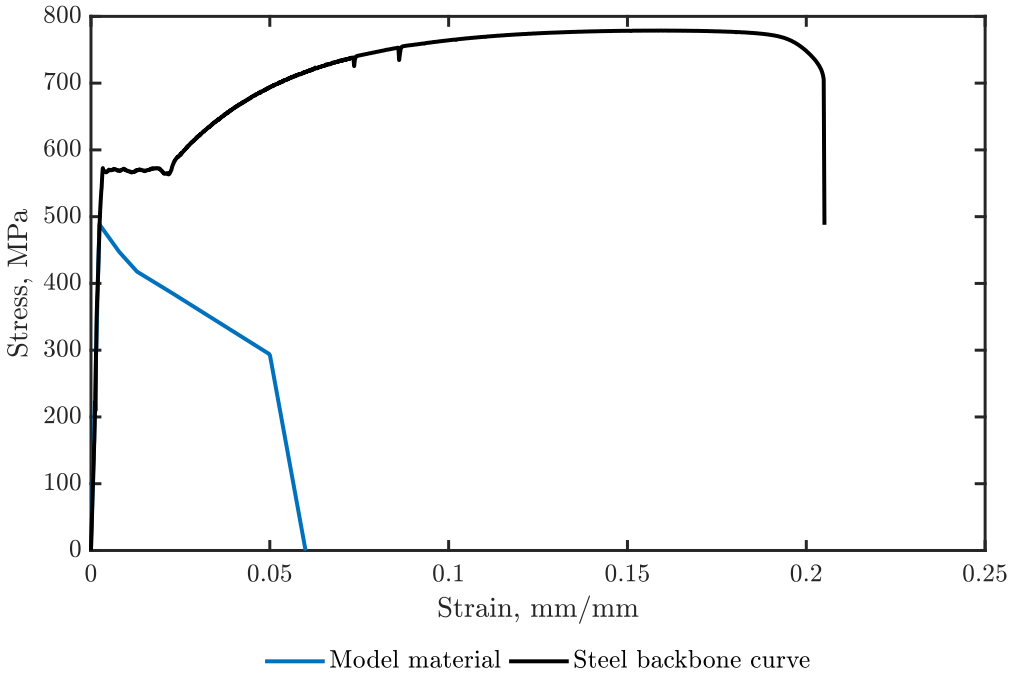

Figure 5.2: Calibrated compression steel constitutive law, including buckling effect - 'ElasticMultilinear'.

5.1.2. Concrete

The constitutive law used to model concrete into the panel element is the denominated 'Concrete04', found in OpenSees. This constitutive law was made for a uniaxial concrete object, and two of its main characteristics are the degraded linear unloading/reloading stiffness, as well as the tensile stress-strain curve has an exponential decay after the tensile stress peak. Confinement is crucial to assess the real model; this is produced by the stirrups restricting the transversal material expansion, increasing the concrete capacity. Fig. 5.3 shows the comparison between the unconfined concrete or the result obtained for specimen M01 (Mixture No. 1 with 0% PVA content) and the confined concrete curve obtain following the procedure elaborated by Saatcioglu and Razvi (1992). In addition, Fig. 5.4 contrast the specimen M03 compression result (Mixture No. 1 with 2% PVA content in weight) against the Saatcioglu and Razvi procedure.

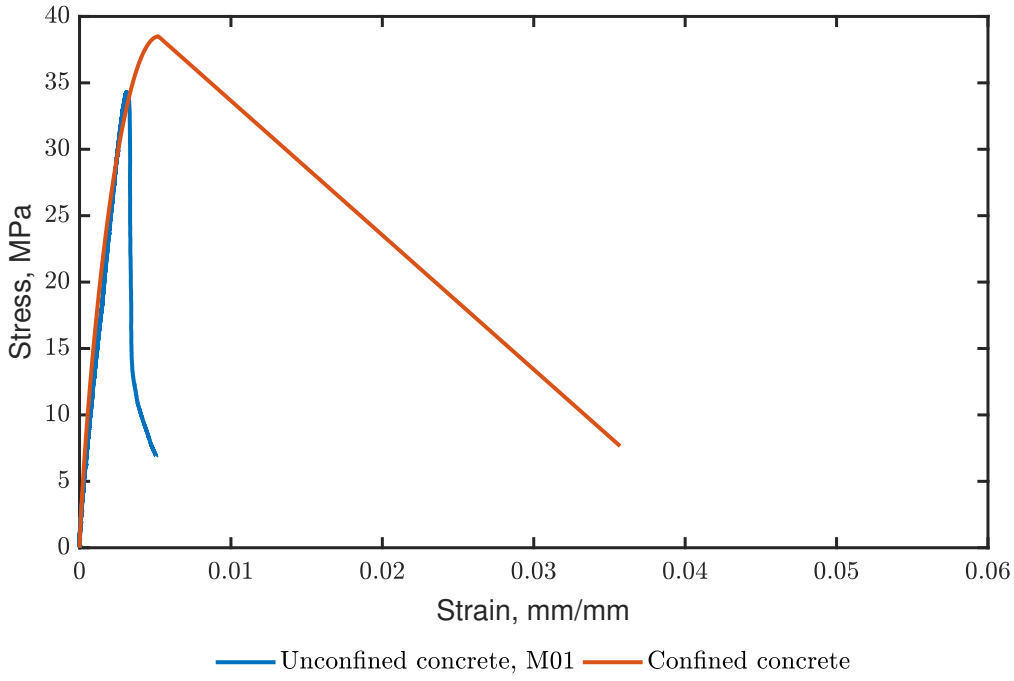

Figure 5.3: Comparison between unconfined concrete (M01) and confined concrete by Saatcioglu and Razvi (1992) in specimens with no PVA content.

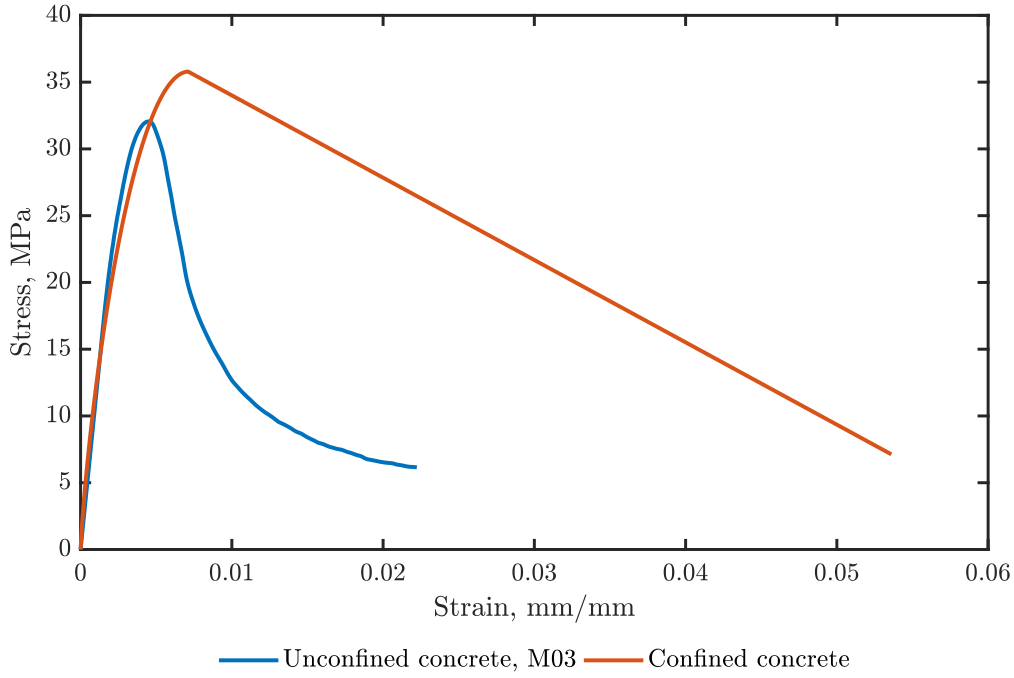

Figure 5.4: Comparison between unconfined concrete (M03) and confined concrete by Saatcioglu and Razvi (1992) in specimens with 2% PVA content.

Considering that no concrete materials available in OpenSees meet the requirements needed to describe concrete behavior with fiber in compression or tension fully, Concrete04 is useful, assuming that the results are approximated.

Fig. 5.5 shows the calibrated Concrete04 material used in the following analytical model for unconfined concrete for both plain concrete and concrete with PVA. On the other hand, Fig. 5.6 shows the calibrated backbone curve for the confined specimens showed in the section before.

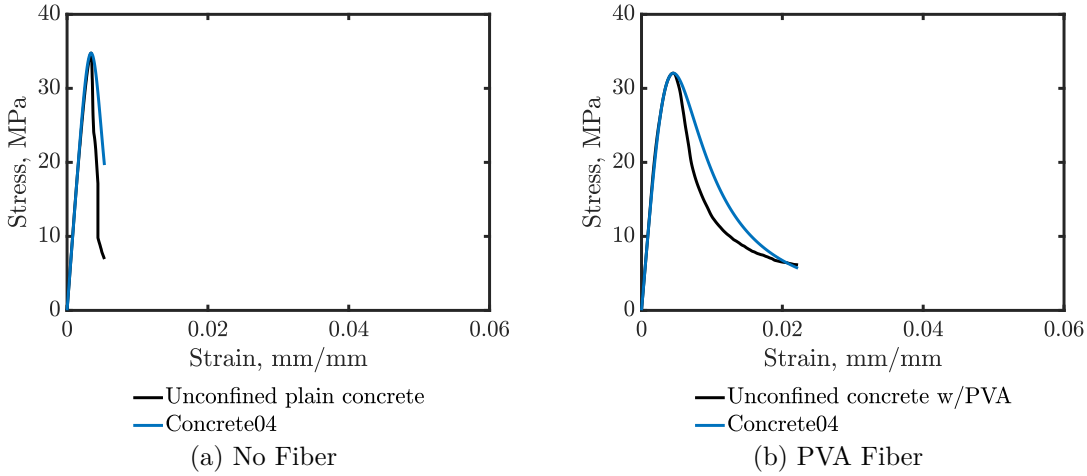

(a) No Fiber (b) PVA Fiber

Figure 5.5: Concrete04 calibration for unconfined concrete.

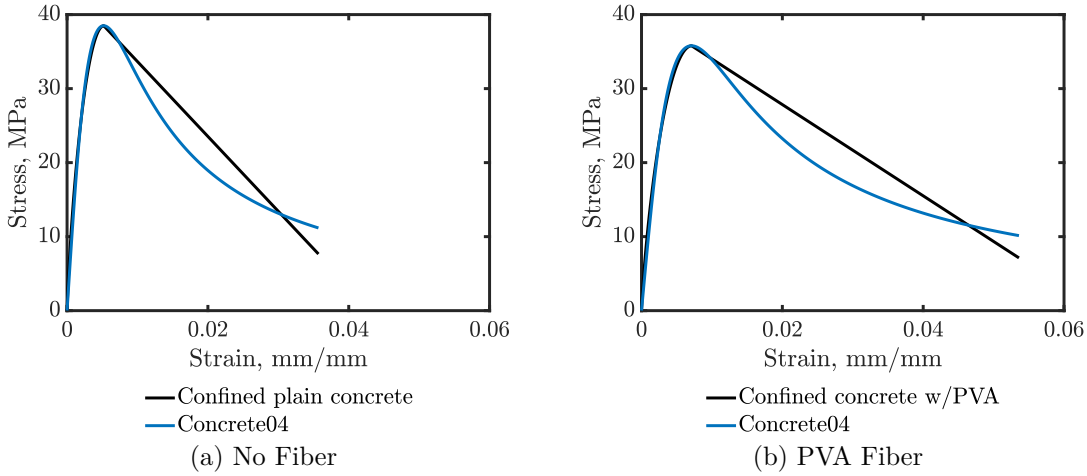

(a) No Fiber (b) PVA Fiber

Figure 5.6: Concrete04 calibration for confined concrete.

Due to the tensile test's failure described in the section before, no tensile experimental data is redeemable. However, thanks to the indirect tensile test, it is possible to obtain the cylindrical specimen's maximum tensile stress (Table 4.15) to start to calibrate the tensile backbone curve. The next part is to depict the residual stress section or the post-peak tensile concrete behavior. This can be done by extrapolating data from previous researchers' works that have performed similar investigation topics, such as Pan et al. (2015), and the Belarbi and Hsu (1994) tensile concrete curve proposal. The curve decay, was made following the curve extracted from Mechtcherine et al. (2011a), showed in Fig. 2.14 . Fig. 5.7 contrasts the tensile curve used in the panel model for both plain concrete and PVA-FRC against the

compressive stress-strain curve obtained by the compression test performed earlier on this investigation.

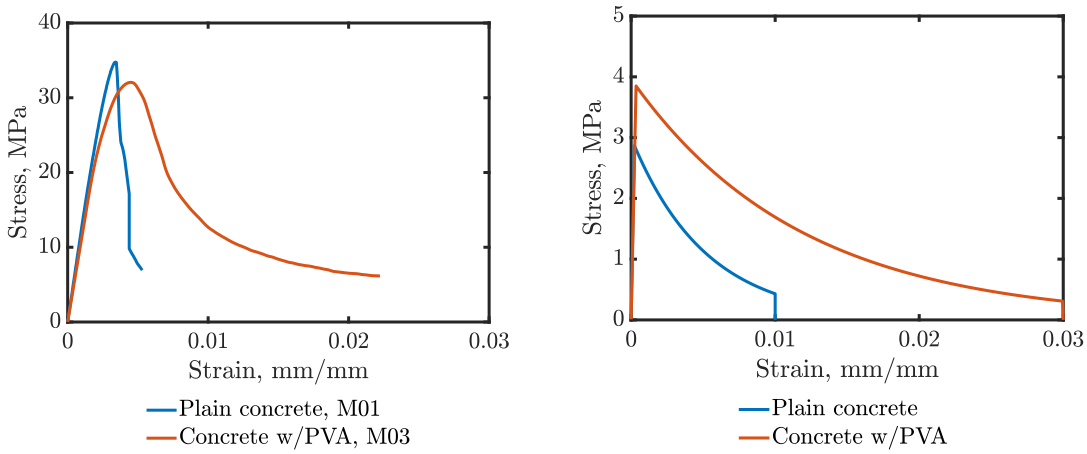

(a) Compression curve

(b) Tensile calibration, 'Concrete04'

Figure 5.7: Concrete04 tensile concrete calibration.

5.2. Sensitivity analysis

In this section, the most important variables in a fiber model will be analyzed. These are the number of elements and the number of fibers/panels in the transversal direction. The constitutive materials described in the section before will be assumed to be calibrated to the real backbone curve obtained by testing; hence it will not vary its main parameters. As mentioned before, half of the beam was modeled considering its longitudinal symmetry adding a rotation restriction on the symmetry axis. As it will be called, the 'symmetry model' is divided into 'n' elements, each containing 'm' fibers in the transversal direction. The analysis consisted in leave 'n' constant and vary the number of panels across the section to assess the influence of the number of panels in the global response, showed in Fig. 5.8.

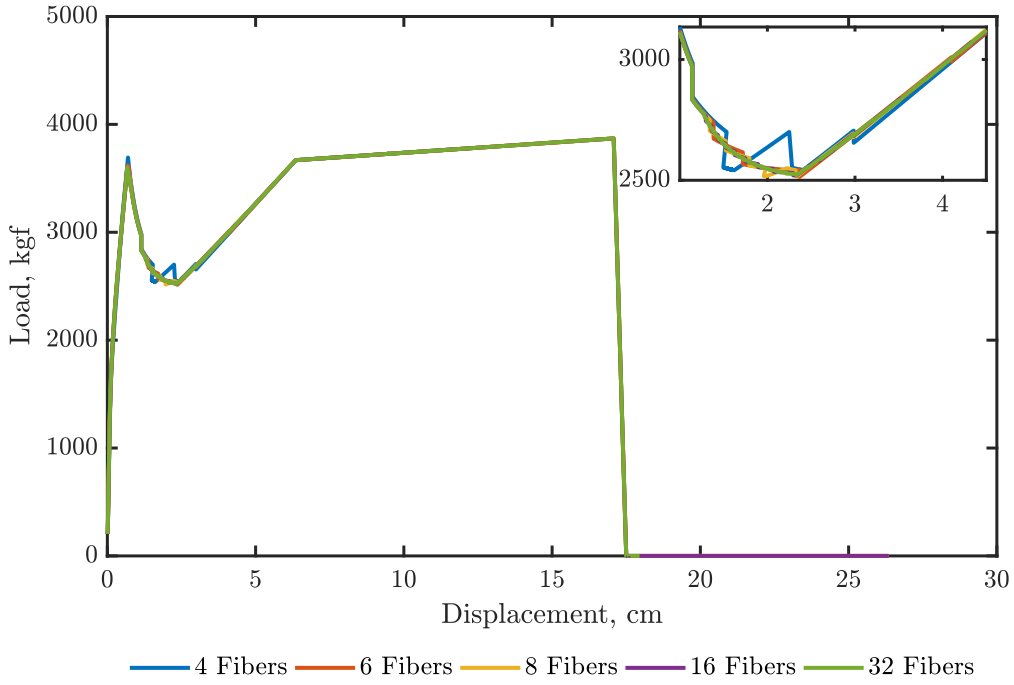

Figure 5.8: Sensitivity analysis varying the panels/fibers number.

On the same criteria, the number of elements is variable this time, leaving constant the number of panels to evaluate the influence on the global response that the number of elements produces. The result of the analysis is shown in Fig. 5.9.

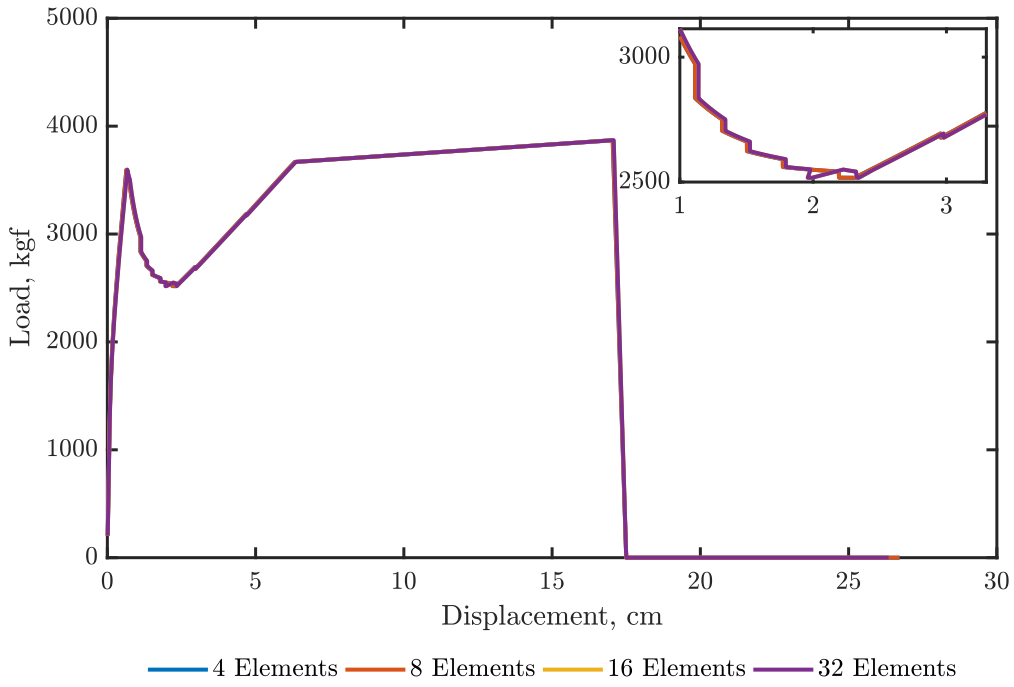

Figure 5.9: Sensitivity analysis varying the element number.

As it can be noticed in Fig. 5.9, the variation of the number of elements produced negligible changes in the pushover global. On the other hand, increasing the number of panels

produces a more smoothed curve. However, it does not change the global response significantly. The magnitude of the load peak and its correspondent displacement presented negligible changes. In conclusion, the choice in the number of panels and element will be exclusively taken assessing the model convergence and the reduction of the number of nodes, without compromising the global response.

5.3. Model's results

The sensitivity analysis performed in Section 5.2 concludes that the number of elements and panels across each element does not change the global response in this simple pushover model significantly. Hence, the criteria used to select the number of elements on each set of models was to keep constant the length of each element. As mentioned before, just half of the beam was modeled to reduce computational loading. Therefore, considering the length of the rigid beam of 200 mm (symmetry) and in the case of the long beams, the length between the support and the loading point of 650 mm, each element along the beam was set to have a length of 50 mm. Therefore, the long beam had 13 elements between the support and the loading point and 4 elements under the rigid beam, 17 elements. Fig. 5.10 depicts the element mesh in the long beams. On the other hand, in the case of short beams, the length between the support and the loading point was 300 mm, hence keeping each element's length. Consequently, short beams had 6 elements between the support and the loading point, keeping the 4 elements in the central section (Fig. 5.11), having 10 elements in total.

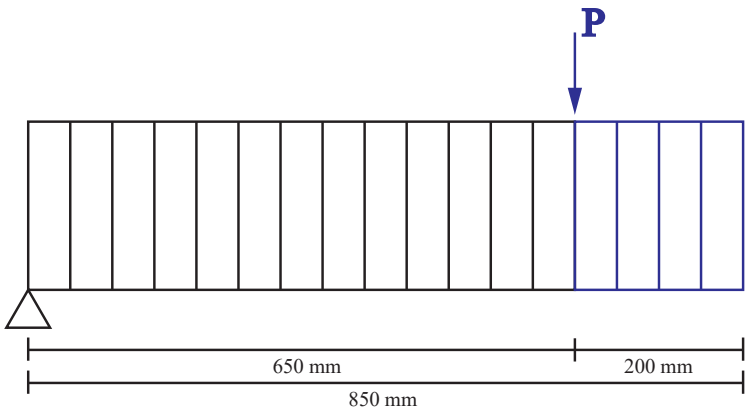

Figure 5.10: Long beams meshing.

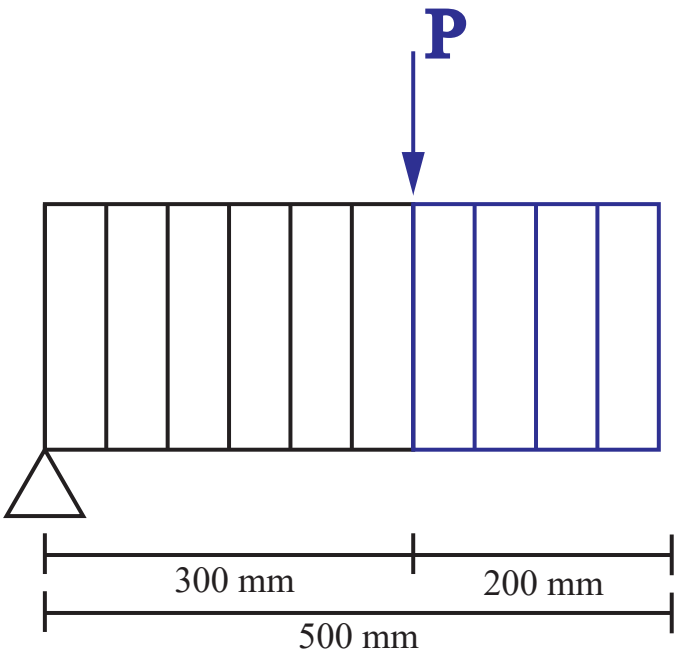

Figure 5.11: Short beams meshing.

5.3.1. Long beams

The result considering the criteria mentioned before, are shown for the long beam with plain concrete in Fig. 5.12 and long beam with 1.23% PVA content concrete in Fig. 5.13. The comparison of both result is shown in Fig. 5.14.

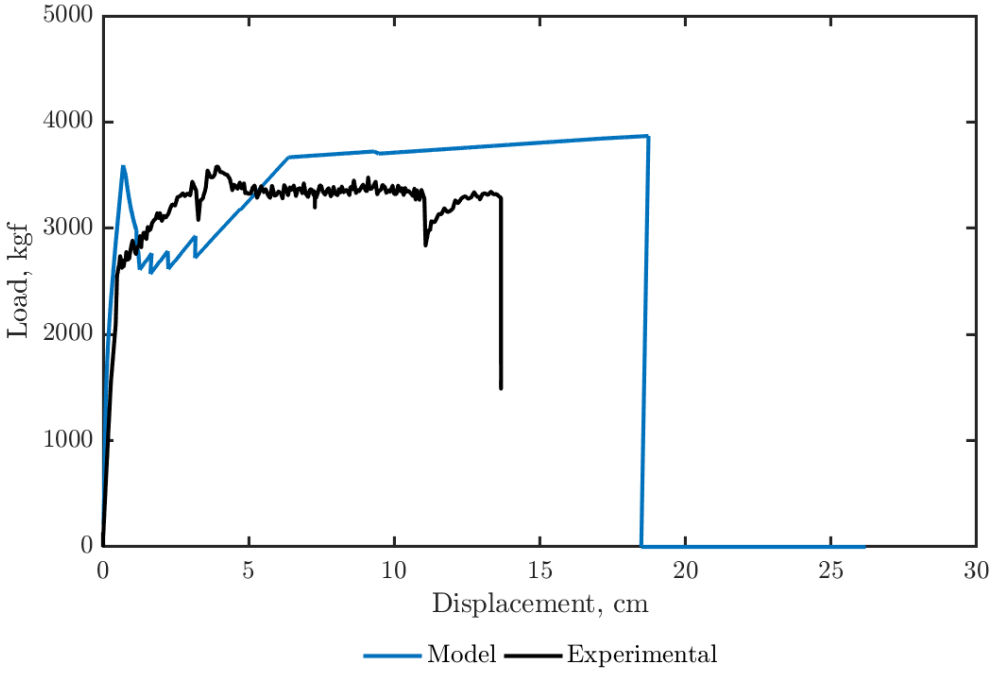

Figure 5.12: Model results for long beam with plain concrete.

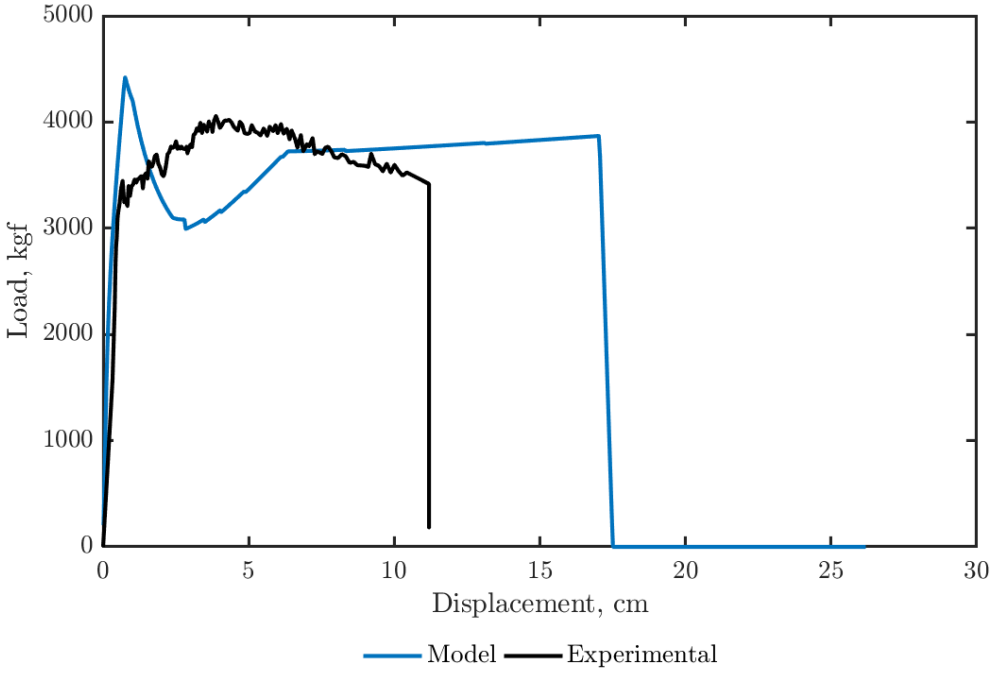

Figure 5.13: Model results for long beam with 1.23% PVA content.

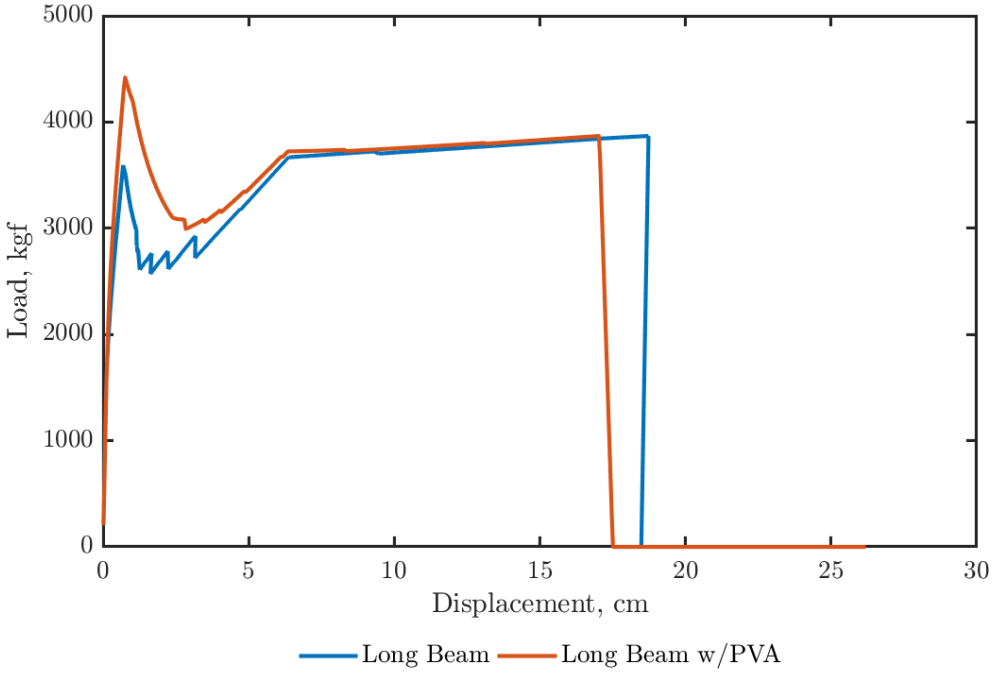

Figure 5.14: Comparison between plain concrete and 1.23% PVA content concrete long beams.

From the results presented in Fig. 5.12 and 5.13 assessing the response of the long beam with plain concrete and long beam with PVA fiber content, respectively, it can be noticed that both models overestimate the peak capacity and the maximum displacement compared to the real response. The main capacity difference is at the moment the reinforcement bars start yielding, at the same time, the concrete in the compressive panel begins to unload, not reaching its maximum capacity. Both beams were tested until the failure of the positive reinforcing bar, the long beam with plain concrete presented lower loading capacity but higher displacement capacity compared to the beam with PVA fiber included (Fig. 4.52), this particular phenomenon was corroborated with the model (Fig. 5.14). The damage obtained by the model is consistent with the pushover testing on the laboratory. However, the decay after the peak is not consistent with the data obtained by testing. All the flexural failures analytical model ended with the steel strain at its maximum value provided by the steel backbone curve. On the other hand, the short beam with plain concrete did not reach the steel yielding point and thus it did not failed by the steel failure.

The overestimation presented by the model is a common result because the model simulates perfect testing conditions and a homogeneous mixture, with no discontinues. These testing conditions are hard to be found in real testing situations. PVA fibers tend to produce voids inside the mixture, which decreases the global response.

In conclusion, the results difference is mainly caused by tensile concrete calibration. No material available in the OpenSees library adjusts closely to the real constitutive law, and the E-SFI elements restrict the concrete material just to two choices, 'Concrete04' and 'ConcreteCM'.

5.3.2. Short beams

The result considering the criteria mentioned before, are shown for the short beam with plain concrete in Fig. 5.15 and short beam with 1.23% PVA content concrete in Fig. 5.16. The comparison of both result is shown in Fig. 5.17.

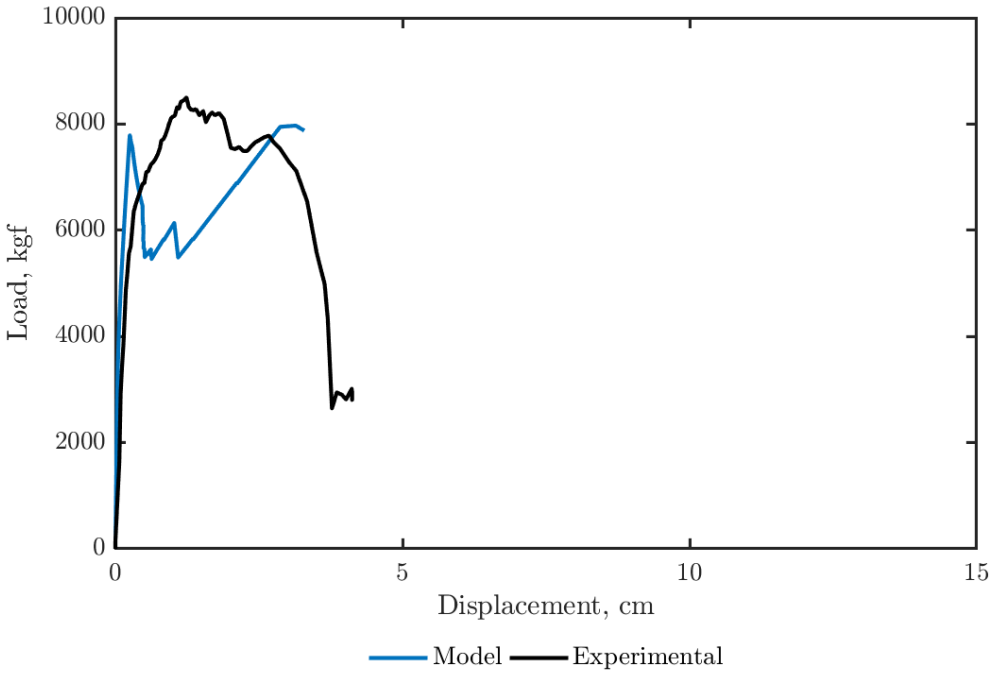

Figure 5.15: Model results for short beam with plain concrete.

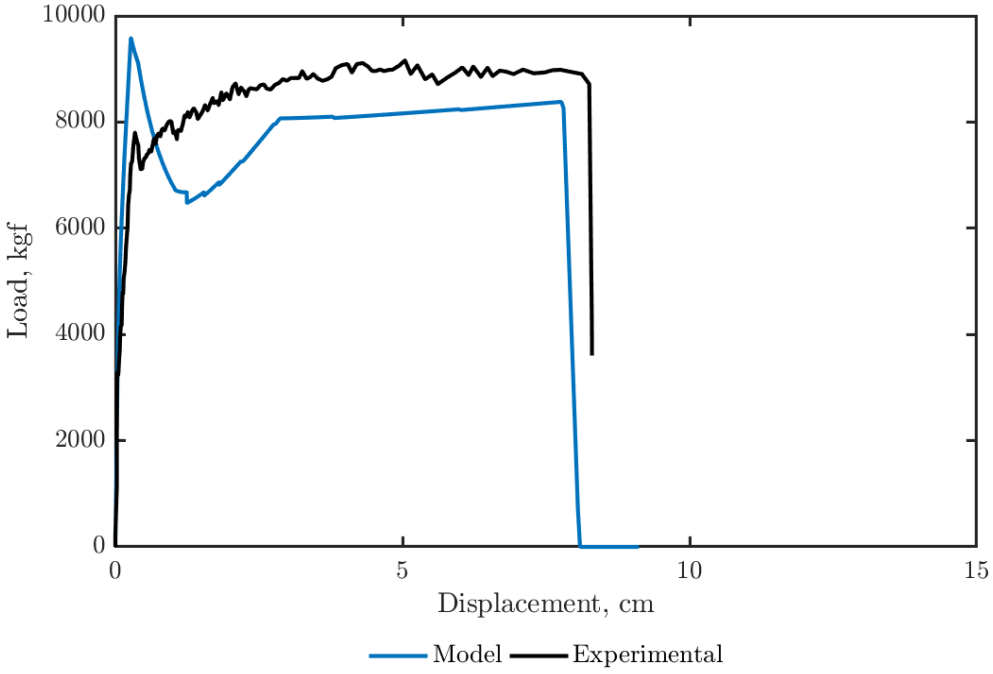

Figure 5.16: Model results for short beam with 1.23% PVA content.

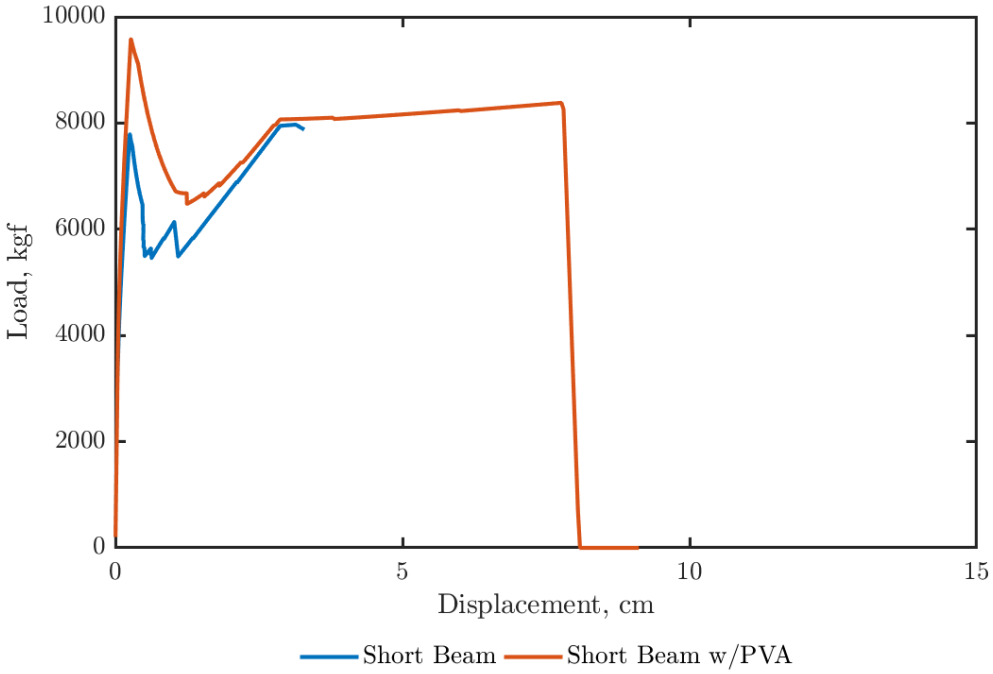

Figure 5.17: Comparison between plain concrete and 1.23% PVA content concrete short beams.

In the case of short beams, both were expected to have a shear failure due to the absence of

stirrups and the short distance between the support and the loading point. On the contrary, just the short beam with plain concrete (Fig. 5.15) failed in the expected mode. The short beam with PVA fiber included failed in flexural mode (Fig. 5.16). Both failure modes were captured by the panel model with E-SFI elements. Both beams were tested until failure or the break of the positive reinforcing bars (flexural failure).

The short beam with PVA fibers presented the same global behavior than the long beam models, an overestimation on the peak capacity but the peak displacement were slightly short compared to the real test (Fig. 5.16). In some way by increasing the concrete tensile capacity and adding more strain capacity to the concrete constitutive law calibration thanks to the addition of fibers, the failure mode can change drastically from shear to flexural. The linear stiffness remains with no changes between the model and the pushover test.

On the other hand, the short beam with plain concrete model (Fig. 5.15) presented a lower loading capacity and a lower deflection compared with the PVA fiber model. Fig. 5.18 depicts the shear strain (ε_{xy}) of both short beams in the point of load element to capture the parameter variation. It can be seen that the short beam with plain concrete (Fig. 5.18(a)) shear strain drastically increases at the end of the analysis compared against the case with PVA fiber. This variation describes a shear strain concentration in the element, denoting a shear failure mode.

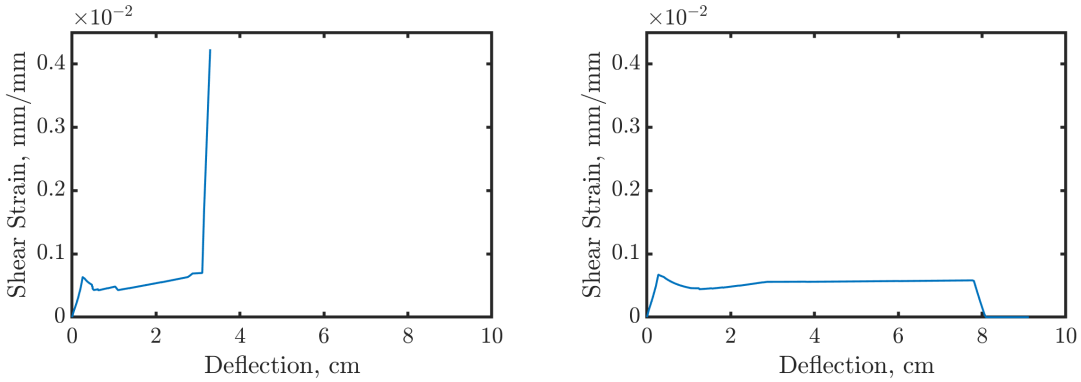

(a) Short beam with plain concrete

(b) Short beam with PVA

Figure 5.18: Element 6 shear strain of both short beams.

5.3.3. Model strain fields

In addition to the nodal displacement, E-SFI also provides the strain magnitude at each panel on each element at any given time, and thus, it is possible to obtain the strain field and compare it against the DIC analysis strain field shown in Section 4.5.2.2. The following sections show the strain fields obtained by the analytical model. The strain fields not found in this section are shown in Appendix E. The resulting strain fields follow the model's element-panel distribution explained in the section before, and just half of the beam for all cases was modeled to reduce computational loading.

5.3.3.1. Shear beam

Figs. 5.19 and 5.20 show the strain field obtained by using the analytical model data. In the shear beam with plain concrete, it can be noticed that at early deflection, the strain concentration focuses on only one element (Fig. Figs. 5.19, element No. 6), and as the deflection increases, the strain concentration remains in the same element. On the other hand, Fig. 5.20 depicts the longitudinal strain (ε_{xx}) due to the flexural behavior capture during the beam testing. The strain concentration is located in the center of the beam, and its magnitude kept increasing as the loading increases. The model also captured the short beam with PVA content flexural failure (Fig. 5.16), and it is reflected in the longitudinal strain as they are located at the center.

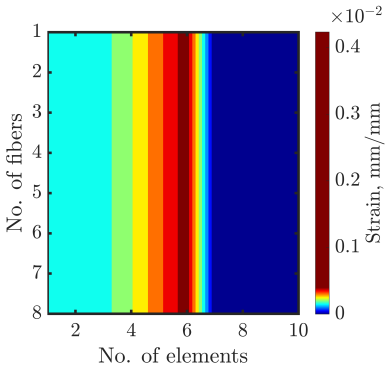

(a) Deflection = 6.7 mm., E-SFI.

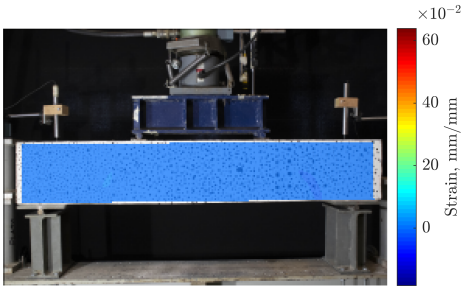

(b) Deflection = 6.7 mm., Ncorr.

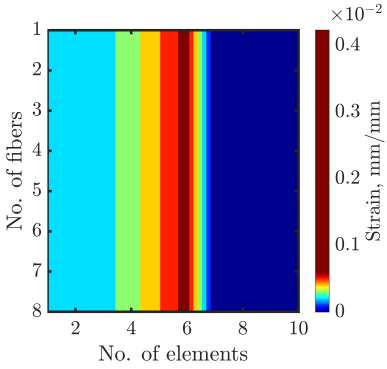

(c) Deflection = 27.9 mm., E-SFI.

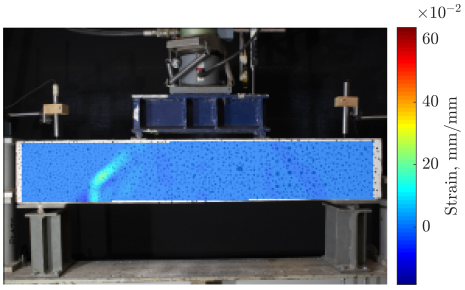

(d) Deflection = 27.9 mm., Ncorr.

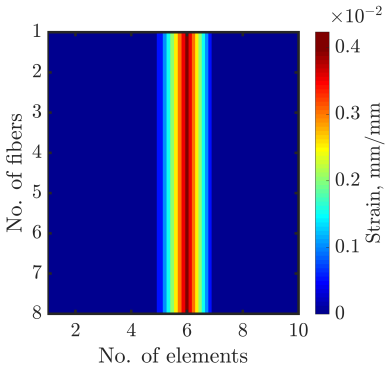

(e) Deflection = 37.6 mm., E-SFI.

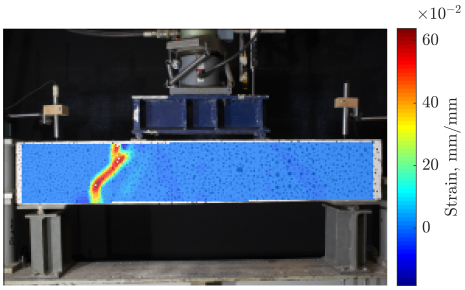

(f) Deflection = 37.6 mm., Ncorr.

Figure 5.19: Comparison between Ncorr and E-SFI field shear strain ε_{xy} development over time, short beam with plain concrete.

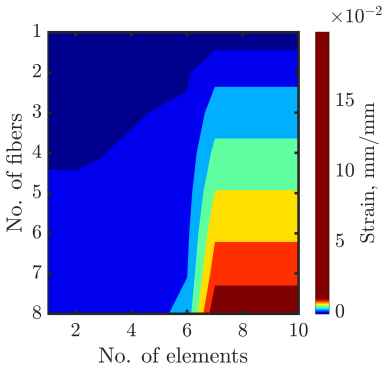

(a) Deflection = 5.6 mm., E-SFI.

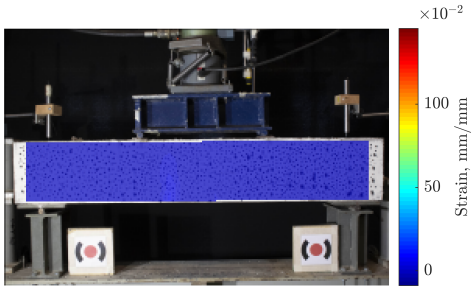

(b) Deflection = 5.6 mm., Ncorr.

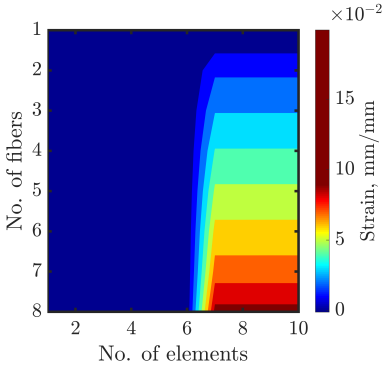

(c) Deflection = 37.3 mm., E-SFI.

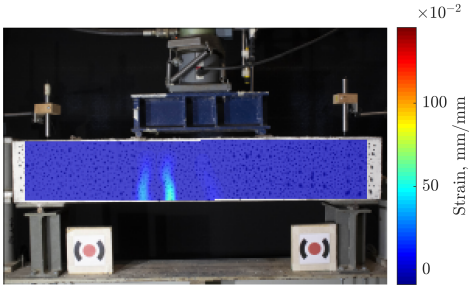

(d) Deflection = 37.3 mm., Ncorr.

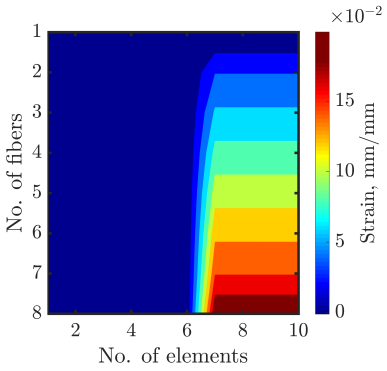

(e) Deflection = 72.8 mm., E-SFI.

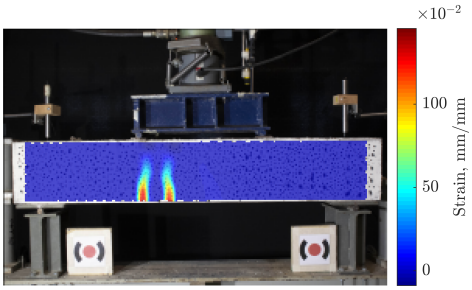

(f) Deflection = 72.8 mm., Ncorr.

Figure 5.20: Comparison between Ncorr and E-SFI field longitudinal strain ε_{xx} development over time, short beam with PVA.

5.3.3.2. Flexural beam

Figs. 5.21 and 5.22 show the strain field obtained by using the data provided by the model. as mentioned in Section 4.5.2.2, both beams had flexural failure as designed. However, the long beam with no PVA fiber presented a greater deflection than the long beam with PVA fiber content, and the model was able to capture this behavior and the loading capacity increment. However, compared with the DIC analysis, the model could not capture the crack distribution, remaining the same for both cases (i.e., long beam and long beam with 1.23% PVA).

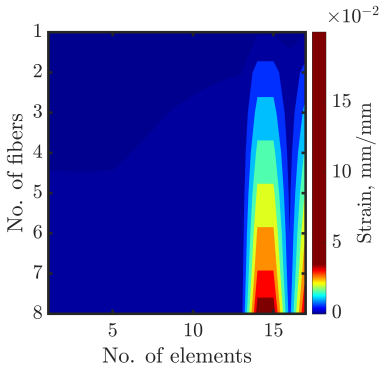

(a) Deflection = 28.4 mm., E-SFI.

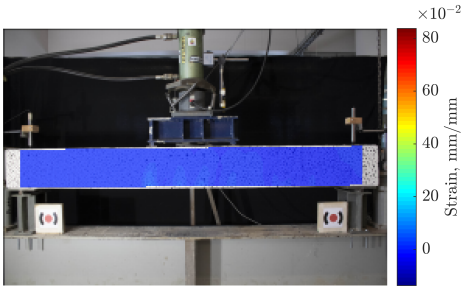

(b) Deflection = 28.4 mm., Ncorr.

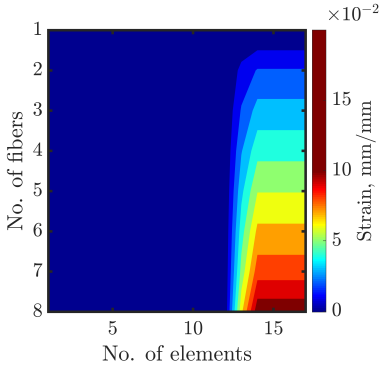

(c) Deflection = 105.8 mm., E-SFI.

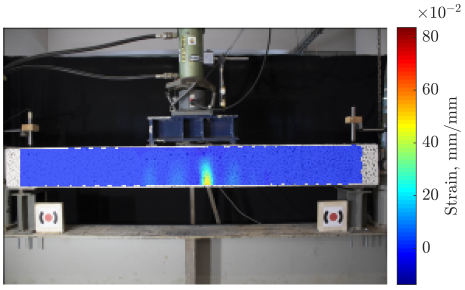

(d) Deflection = 105.8 mm., Ncorr.

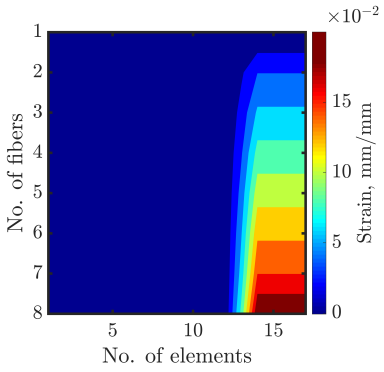

(e) Deflection = 145.9 mm., E-SFI.

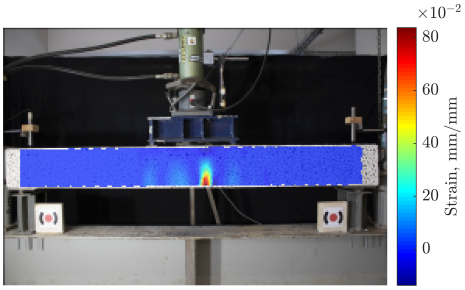

(f) Deflection = 145.9 mm., Ncorr.

Figure 5.21: Comparison between Ncorr and E-SFI field longitudinal strain ε_{xx} development over time, long beam.

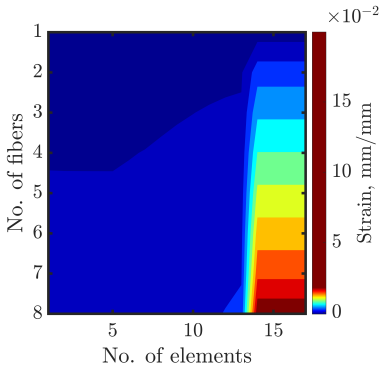

(a) Deflection = 19.8 mm., E-SFI.

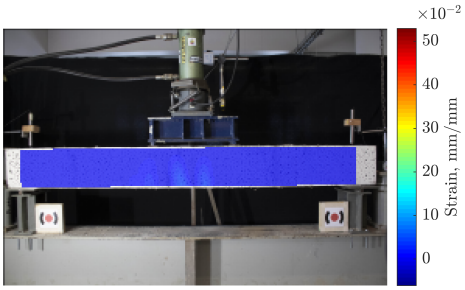

(b) Deflection = 19.8 mm., Ncorr.

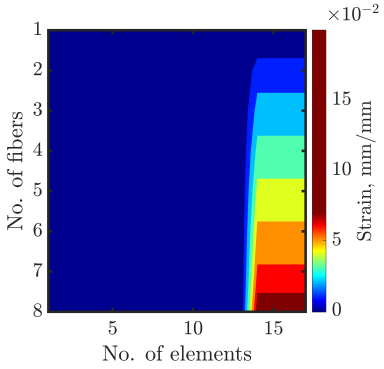

(c) Deflection = 68.3 mm., E-SFI.

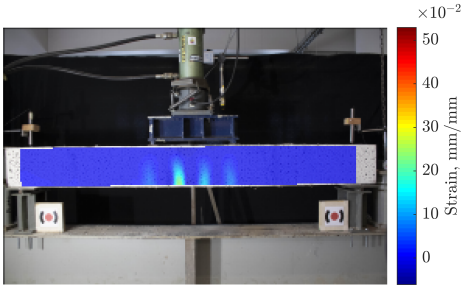

(d) Deflection = 68.3 mm., Ncorr.

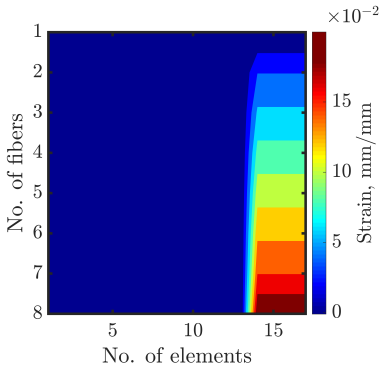

(e) Deflection = 117.3 mm., E-SFI.

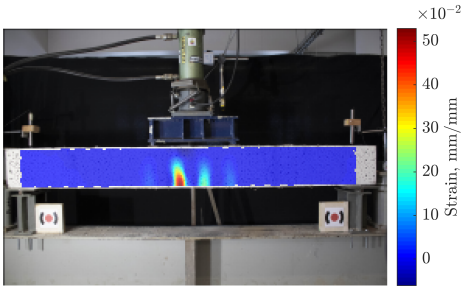

(f) Deflection = 117.3 mm., Ncorr.

Figure 5.22: Comparison between Ncorr and E-SFI field longitudinal strain ε_{xx} development over time, long beam with PVA.

Chapter 6

Conclusion

This investigation gives a complete procedure to characterize the influence of the addition of low PVA fiber content, less than 1.23% by volume to the concrete mixture with coarse aggregate. Summarizes the documentation of what has been done thus far, gives a complete description of compressive and tensile concrete tests and fully describe the data analysis. Also, shows a computational model calibration using a panel element, such as E-SFI to replicate the beam pushover test performed before. The literature review showed that the PVA fiber addition in mortars increases the ductility without significantly degrading its resistance, differentiate of other researchers by the mixture used in all tests. The research resumes the project developed from the mixture design to the analytical panel model developed in OpenSees to validate the experimental results, detailing the experimental setup and specimens tested.

PVA-FRC with coarse aggregate does not change the concrete elasticity modulus compared to plain concrete in compression testing, as it can be seen in Fig. 4.15 (a). The same figure shows another particularity due to the addition of PVA fiber to the mixture; as the PVA amount increases, its compressive capacity decays. This is because PVA fibers tend to produce air voids inside the mixture; more PVA means more air voids, which does not help to increase the stress capacity. This phenomenon is consistent with researchers' work on PVA fiber investigation with mortars. It is well known that concrete compressive failure occurs right after the peak, forming a 45 degree crack across the cylindrical specimen (Fig. 4.18(a), plain concrete) and abruptly decreasing its capacity. However, the addition of PVA to the mixture increases the post-peak strain, reducing the post cracked slope, which provides concrete a lower decreasing rate and increases its residual capacity. This is due to PVA forming bridges inside the cracks, preventing it from increasing. Therefore, this bridging effect allow concrete to hold the micro cracks formed in the transversal direction of loading, producing what the author called a 'pseudo-confinement', decreasing the residual slope rate, increasing its maximum strain up to 11 times (Table 4.14).

Due to the testing condition, it was not possible to assess the behavior of PVA-FRC in tension loads to obtain the material's stress-strain curve. However, the indirect tensile test allowed to know the peak tensile strength of PVA-FRC with coarse aggregate and compare it to the plain concrete specimen. The results showed that increasing the amount of PVA in the mixture increases the material tensile strength, approximately up to 34% comparing specimens M01 and M03 (Table 4.15). Consequently, adding PVA to the concrete mixture

increases the tensile strength significantly. It was not possible to retrieve data to conclude that PVA-FRC increases the ultimate strain as the literature review points out, due to the direct tensile test's failure. Nevertheless, it is necessary to assess this behavior to characterize the PVA-FRC fully. Therefore, a direct tensile test is suggested, keeping the same mixture and PVA content and increasing the mixture's fiber to assess tensile behavior.

From the two short beams tested, it is possible to notice the failure improvement by adding PVA fiber to the mixture. Both short beams were expected to have the same shear failure mode. However, PVA incorporation switched the failure mode into the flexural mode, a ductile failure. This is a huge improvement due that allows beams to reach high deformation with no strength reduction. Both beams also had the same strength capacity of approximately 8,000 kgf (Fig. 4.46), concluding that the addition of PVA into the mixture does not change the stress capacity considerably and improves its deflection significantly. Considering the valuable result obtained, the author also suggests repeating the test, with no mixture variation but increasing the beam tested to validate the result.

On the other hand, from the two long beams tested is clearly that PVA-FRC increases the load capacity up to 25% approximately. However, the deflection decreased 30 mm approximately (Fig. 4.52), and reduced the crack-distribution in the beam compared to the control specimen. Higher crack distribution along the beam implies a higher deflection and a larger curvature. The author also suggests repeating the test to validate the results.

DIC analysis was fundamental to obtain the beam deflection at any point, and it was helpful to compare the displacement data obtained by the instruments and the DIC displacement. As explained in the investigation, the instruments (ultrasonic sensor and LVDTs) due to the limited measurement range. This method presented the most feasible data of the three and it was the one employed to retrieve the beam deflection.

Finally to implement the analytical model, the PVA-FRC obtained by both compressive and tensile tests were calibrated along with the steel backbone curve. Concrete was calibrated using the 'Concrete04' material found in the OpenSees library. Assuming a pushover test (non cyclic), steel on the other hand, was calibrated manually using an elastic material from the library available, following the backbone curve obtained by the direct tensile reinforcing bar testing described in this research. In the concrete, also the confinement was includes in the calibration following procedure from Saatcioglu and Razvi obtained by using traditional reinforced concrete.

For slender elements (long beams), the model is capable to capture the specimen behavior fully. Following the real linear stiffness from the tests (Fig. 5.14) and able to capture the strength increase and the deflection difference between both. For short elements, the model is able to capture the switched failure mode between the concrete with PVA and the plain concrete specimen (Fig. 5.17), just by changing the mechanical concrete properties, such as ultimate strain, both peak stress (tensile and compressive) and the tensile post-peak decay.

PVA fiber inclusion to the coarse aggregate concrete in compression, increases the strain capacity without degrading significantly its compressive strength. It also, increments the tensile strength thanks to the PVA fiber bridging effect. Fiber 'A' compared to the other

fibers, showed higher strain capacity, even though, it has the short diameter and the lower elongation at break. Pushover test on short beams showed an incredibly failure mode switch by adding 1.23% PVA content into the mixture, increasing significantly its performance, creating a precedent of what the right addition of PVA fiber can do to the global performance.

List of terms

ASTM	American Society of Testing Materials.
CPU	Central Processing Unit.
DIC	Digital image correlation.
DOFs	Degrees of Freedom.
E-SFI	Efficient Shear-Flexure Interaction.
ECC	Engineered Cementitious Composite.
FRC	Fiber Reinforced Concrete.
GPa	Gigapascal or 10^9 Pa.
ICGN	Inverse Compositional Gauss-Newton.
LVDTs	Linear variable differential transformers.
MATLAB®	Matrix Laboratory is a multi-paradigm numerical computing environment and proprietary programming language developed by MathWorks.
MPa	Megapascal or 10^6 Pa.
MVLEM	Multiple Vertical Line Element Model.
Ncorr	Open-Source 2D Digital Image Correlation for MATLAB®.
PE	Polyethylene.
PP	Polypropylene.
PVA	Polyvinyl-alcohol.
PVA-FRC	Polyvinyl-alcohol Fiber Reinforced Concrete.
PVAc	Polyvinyl acetate.
ROI	Region of Interest.

SCC	Self-Consolidating Concrete.
SFI-MVLEM	Shear-Flexural interaction model.
SFRC	Steel Fiber Reinforced Concrete.
SHCC	Strain-hardening cement-based composites.
SP	Superplasticizer.
SRC	Steel Reinforced Concrete.

Bibliography

318, A. C. (2019). *ACI 318-19 Building Code Requirements for Structural Concrete (ACI 318-19) and Commentary (ACI 318R-19)*. American Concrete Institute.

Aghdasi, P., Heid, A. E., and Chao, S.-h. (2016). Developing Ultra-High-Performance Fiber-Reinforced Concrete for Large-Scale Structural Applications. *ACI Materials Journal*, 113(5):559–570.

Allahverdi, A., Kianpur, K., and Moghbeli, M. R. (2010). Effect of polyvinyl alcohol on flexural strength and some important physical properties of Portland cement paste. *Iranian Journal of Materials Science and Engineering*, 7(1):1–6.

American Society of Testing and Materials. (2010). ASTM C78/C78M-18: Standard Test Method for Flexural Strength of Concrete (Using Simple Beam with Third-Point Loading). *ASTM International*, C78-02(C):1–4.

American Society of Testing and Materials. (2011). ASTM C496-11: Standard Test Method for Splitting Tensile Strength of Cylindrical Concrete Specimens. *Annual Book of ASTM Standards Volume 04.02*, i:1–5.

American Society of Testing and Materials. (2014). ASTM C136/C136M - 19: Standard Test Method for Sieve Analysis of Fine and Coarse Aggregates. *Annual Book of ASTM Standards*, pages 3–7.

American Society of Testing and Materials. (2015). ASTM C39: Compressive Strength of Cylindrical Concrete Specimens. *ASTM Standards*, pages 1–7.

Annam, R. (2015). *Study of Mechanical Properties of PVA Fiber- Reinforced Concrete With Raman Spectroscopic Analysis*. Msc thesis, Western Kentucky University.

Arslan, M. (2016). Effects of basalt and glass chopped fibers addition on fracture energy and mechanical properties of ordinary concrete: CMOD measurement. *Build. Mater.*, 114:383—-391.

Ayub, T., Khan, S. U., and Ayub, A. (2019). Analytical model for the compressive stress–strain behavior of PVA-FRC. *Construction and Building Materials*, 214:581–593.

Belarbi, A. and Hsu, T. T. (1994). Constitutive laws of Concrete in Tension and Reinforcing Bars Stiffened by Concrete. *ACI Structural Journal*, 91:465–474.

Bentur, A. and Mindess, S. (2007). *Fibre Reinforced Cementitious Composites*. Taylor and Francis, second ed. edition.

Blaber, J., Adair, B., and Antoniou, A. (2015). Ncorr: Open-Source 2D Digital Image Correlation Matlab Software. *Experimental Mechanics*, 55(6):1105–1122.

Brandt, A. M. (2008). Fibre reinforced cement-based (FRC) composites after over 40 years of development in building and civil engineering. *Composite Structures*, 86(1-3):3–9.

Cadoni, E., Meda, A., and Plizzari, G. A. (2009). Tensile behaviour of FRC under high strain-rate. *Materials and Structures/Materiaux et Constructions*, 42(9):1283–1294.

Carmona, S. and Aguado, A. (2012). New model for the indirect determination of the tensile stress-strain curve of concrete by means of the Brazilian test. *Materials and Structures/-Materiaux et Constructions*, 45(10):1473–1485.

Choi, S. J., Yang, K. H., Sim, J. I., and Choi, B. J. (2014). Direct tensile strength of lightweight concrete with different specimen depths and aggregate sizes. *Construction and Building Materials*, 63:132–141.

Cotterell, B. and Mai, Y. (1995). *Fracture Mechanics of Cementitious Materials*. Taylor & Francis.

Felekoglu, B., Tosun-Felekoglu, K., and Gödek, E. (2015). A novel method for the determination of polymeric micro-fiber distribution of cementitious composites exhibiting multiple cracking behavior under tensile loading.

Fiore, V., Scalici, T., Di Bella, G., and Valenza, A. (2015). A review on basalt fibre and its composites. *Compos. B Eng.*, 74:74—-94.

Hamoush, S., Abu-Lebdeh, T., and Cummins, T. (2010). Deflection behavior of concrete beams reinforced with PVA micro-fibers. *Construction and Building Materials*, 24(11):2285–2293.

Hoff, G. C. (1986). *Use of steel fiber reinforced concrete in bridge decks and pavements, in: Steel Fiber Concrete*. Elsevier Applied Sciences Publishers Ltd.

Holschemacher, K. and Höer, S. (2008). 'influence of pva fibers on load carrying capacity of concrete with coarse aggregates'. *7th Int. Rilem Symp. on Fibre Reinforced Concrete: Design and Applications*, pages 219–229.

Holschemascher, K. and Höer, S. (2008). Influence of PVA fibers on load carrying capacity of concrete with coarse aggregates.

Horikoshi, T., Ogawa, A., Saito, T., Hoshiro, H., Fischer, G., and Li, V. (2006). Properties of polyvinyl alcohol fiber as reinforcing materials for cementitious composites. In *Proceedings of the International RILEM Workshop on High Performance Fiber Reinforced Cementitious Composites in Structural Applications*, pages 145–153.

Hossain, K. M., Lachemi, M., Sammour, M., and Sonebi, M. (2013). Strength and fracture energy characteristics of self-consolidating concrete incorporating polyvinyl alcohol, steel and hybrid fibres. *Construction and Building Materials*, 45:20–29.

Jeon, E., Ahn, S., Lee, I., Koh, H., Park, J., and Kim, S. (2015). Investigation of mechanical/dynamic properties of carbon fiber reinforced polymer concrete for low noise railway slab. *Compos. Struct.*, 134:27—35.

Khan, S. U. and Ayub, T. (2016). Modelling of the pre and post-cracking response of the PVA fibre reinforced concrete subjected to direct tension. *Construction and Building Materials*, 120:540–557.

Kolozvari, K., Orakcal, K., and Wallace, J. W. (2015a). Modeling of cyclic shear-flexure inter-

action in reinforced concrete structural walls. I: Theory. *Journal of Structural Engineering*, 141(5):1–10.

Kolozvari, K., Tran, T. A., Orakcal, K., and Wallace, J. W. (2015b). Modeling of cyclic shear-flexure interaction in reinforced concrete structural walls. II: Experimental validation. *Journal of Structural Engineering*, 141(5):1–12.

Li, M. and Li, V. C. (2013). Rheology, fiber dispersion, and robust properties of engineered cementitious composites. *Materials and Structures/Materiaux et Constructions*, 46(3):405–420.

Li, Z., Li, F., Chang, T. Y. P., and Mai, Y. W. (1998). Uniaxial tensile behavior of concrete reinforced with randomly distributed short fibers. *ACI Materials Journal*, 95(5):564–574.

Massone, L. M., López, C. N., and Kolozvari, K. (2020). Formulation of an efficient shear-flexure interaction model for planar reinforced concrete walls. *Engineering Structures*, (Submitted for publication).

Massone, L. M. and Moroder, D. (2009). Buckling modeling of reinforcing bars with imperfections. *Engineering Structures*, 31(3):758–767.

Mechtcherine, V., De Andrade Silva, F., Butler, M., Zhu, D., Mobasher, B., Gao, S. L., and Mader, E. (2011a). Behaviour of strain-hardening cement-based composites under high strain rates. *Journal of Advanced Concrete Technology*, 9(1):51–62.

Mechtcherine, V., Millon, O., Butler, M., and Thoma, K. (2011b). Mechanical behaviour of strain hardening cement-based composites under impact loading. *Cement and Concrete Composites*, 33(1):1–11.

Mehta, P. K. and Monteiro, P. J. (2006). *Concrete: Microstructure, properties, and materials*. Mc Graw Hill, 3 edition.

Nilson, A. H., Darwin, D., and Dolan, C. W. (2010). *Design of Concrete Structures*. Mc Graw Hill, New York, 14 edition.

Pan, Z., Wu, C., Liu, J., Wang, W., and Liu, J. (2015). Study on mechanical properties of cost-effective polyvinyl alcohol engineered cementitious composites (PVA-ECC). *Construction and Building Materials*, 78:397–404.

Redon, C., Li, V. C., Wu, C., Hoshiro, H., Saito, T., and Ogawa, A. (2002). Measuring and Modifying Interface Properties of PVA Fibers in ECC Matrix. *Journal of Materials in Civil Engineering*, 13(6):399–406.

Saatcioglu, M. and Razvi, S. R. (1992). Strength and Ductility of Confined Concrete. *Journal of Structural Engineering*, 118:1590–1607.

Sahmaran, M., Yücel, H. E., Demirhan, S., Arık, M. T., and Li, V. C. (2012). Combined Effect of Aggregate and Mineral Admixtures on Tensile Ductility of Engineered Cementitious Composites. *ACI Materials Journal*, 109(6):627–638.

Sasmal, S. and Avinash, G. (2016). Investigations on mechanical performance of cementitious composites micro-engineered with poly vinyl alcohol fibers. *Construction and Building Materials*, 128:136–147.

Sear, L., Dews, J., Kite, B., Harris, F., and Troy, J. (1996). Abrams law, air and high water-to-cement ratios. *Construction and Building Materials*, 10(3):221 – 226.

Swaddiwudhipong, S., Lu, H. R., and Wee, T. H. (2003). Direct tension test and tensile strain capacity of concrete at early age. *Cement and Concrete Research*, 33(12):2077–2084.

Thong, C. C., Teo, D. C., and Ng, C. K. (2016). Application of polyvinyl alcohol (PVA) in cement-based composite materials: A review of its engineering properties and microstructure behavior. *Construction and Building Materials*, 107:172–180.

Toutanji, H., Xu, B., Gilbert, J., and Lavin, T. (2010). Properties of poly(vinyl alcohol) fiber reinforced high-performance organic aggregate cementitious material: Converting brittle to plastic. *Construction and Building Materials*, 24:1–10.

Ulugtekin, D. (2010). Analytical modeling of reinforced concrete panel elements under reversed cyclic loadings. Master's thesis, Bogazici Univ., Istanbul, Turkey.

Vasquez, N. (2019). *Estudio de la variación de ductilidad y resistencia del hormigón al reforzarlo con microfibras de PVA*. PhD thesis, Universidad de Chile.

Wang, Z., Zuo, J., Zhang, X., Jiang, G., and Feng, L. (2020). Stress-strain behaviour of hybrid-fibre engineered cementitious composite in compression. *Advances in Cement Research*, 32(2):53–65.

Yu, K., Li, L., Yu, J., Wang, Y., Ye, J., and Xu, Q. F. (2018). Direct tensile properties of engineered cementitious composites: A review. *Construction and Building Materials*, 165:346–362.

Appendix A

Preliminary tests

The purpose of the preliminary tests is to obtain results that provide a first behavior approximation of traditional cementitious mixture reinforced with PVA microfibers compare to the plain mixture. Considering that the cementitious mixture workability decreases with the addition of PVA fibers. Thus the first preliminary test assesses the influence of superplasticizer coarse aggregate cementitious mixture and creates a procedure to create the mixture consistently without a considerable response change between the two specimens tested.

Table A.1: Mixture's types.

Mixture No.	Concrete (kg/m^3)	Water (kg/m^3)	Aggregate (kg/m^3)		
			Gravel	Sand	
				Coarse	Fine
1	500	250	770	500	375
2	500	250	-	940	705
3	500	250	-	-	1645

A.1. Preliminary test #1

For the preliminary test, eight specimens of 100 mm diameter x 200 mm height were cast and cured for seven days each. All three mixtures were tested without fiber included; this test's main purpose was to assess the influence of superplasticizer in the mixture and reduce the variability of the mixture process. To achieve that, all three mixtures had a w/c-ratio of 0.5. The tests were performed seven days after the mixture process. The testing matrix is shown in Tab. A.2.

Table A.2: Preliminary testing matrix #1.

Specimen	Test	Mixture	Superplasticizer
PT01	Compression	1	Yes
PT02	Compression	1	Yes
PT03	Compression	1	No
PT04	Compression	1	No
PT05	Compression	2	No
PT06	Compression	2	No
PT07	Compression	3	No
PT08	Compression	3	No

The results of the compressive testing are presented in Fig. A.1. As the tests were performed in seven days after the mixture process, the compressive strength is not the main concern, the SP improves the workability of the mixture but has a little impact in the concrete strength (Fig. A.1 (b) & Fig. A.1 (a)). Besides, the matrix stiffness increases in the same period of time with the use of SP. Specimens showed low variability. Thus the mixing process is acceptable and will be used in the following tests. The variability of specimens PT07 and PT08 may be caused by the water retained in the fine sand aggregate. During this preliminary test, the water retained by each aggregate was not assessed. The following tests will consider this, which has a tremendous impact on the cementitious mixture behavior. The main data extracted in Fig. A.1 is tabulated in Tab. A.3.

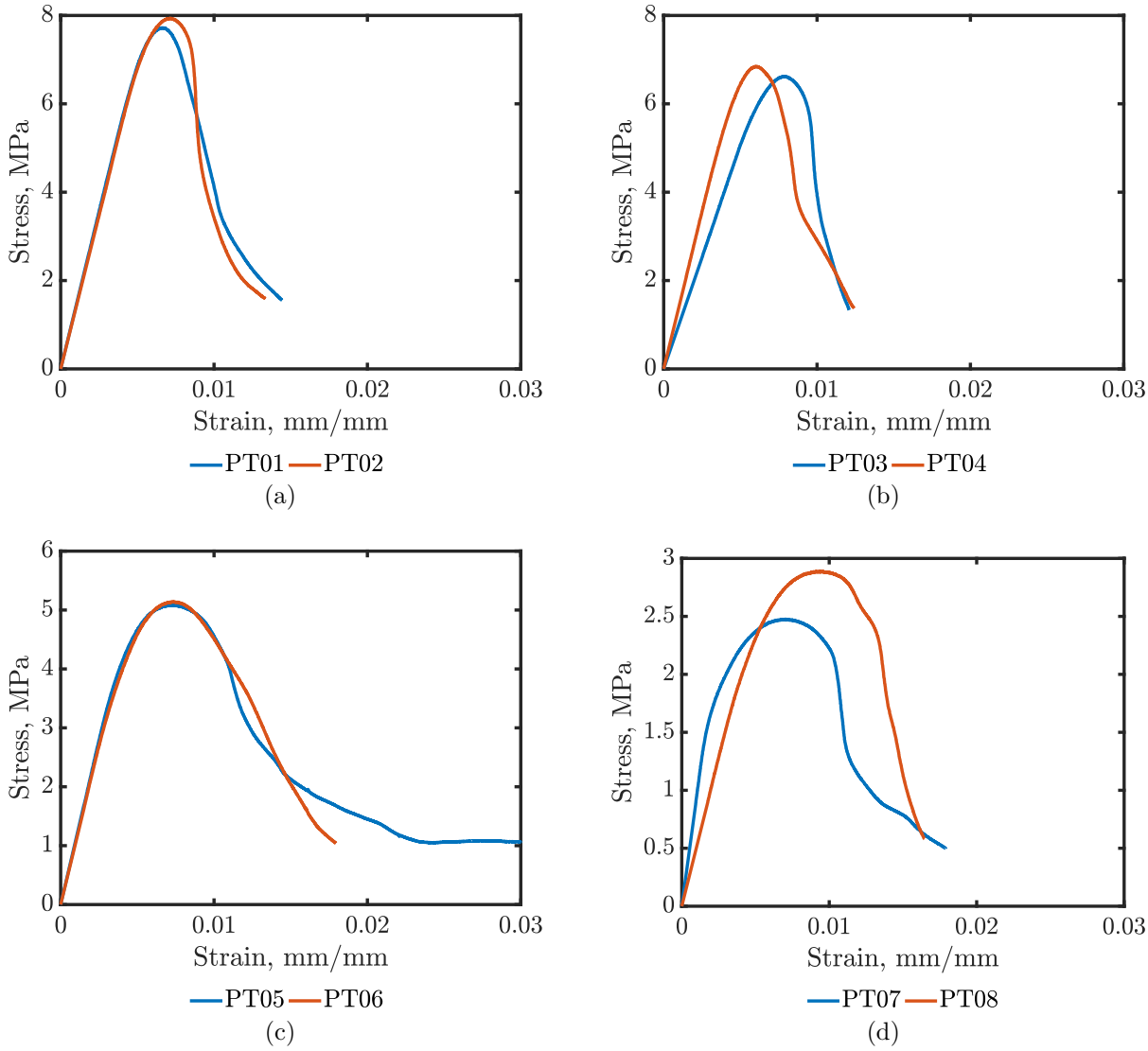

Figure A.1: Preliminary test #1 results.

Table A.3: Main data of preliminary test #1.

Specimen	E_c (MPa)	Peak Stress (MPa)	Strain at peak (-)	Max. Strain (-)
PT01	1425.663	7.723	0.00662	0.01444
PT02	1388.837	7.933	0.00710	0.01336
PT03	1007.543	6.620	0.00789	0.01209
PT04	1412.352	6.845	0.00607	0.01243
PT05	1115.497	5.086	0.00713	0.03020
PT06	1072.549	5.141	0.00727	0.01795
PT07	933.051	2.477	0.00704	0.01790
PT08	509.068	2.889	0.00911	0.01646

A.2. Preliminary test #2

In the second preliminary test, thirteen specimens of 100 mm diameter and 200 mm height were used. Each specimen was fourteen days cured. Just one mixture was tested, knowing that superplasticizer increases the mixture's plasticity and, by that, improves workability. Thus, the main purpose was to find the right amount of superplasticizer needed in the mixture and try the direct tensile setup used by Nicolas Vasquez in its research (Vasquez, 2019). During the first preliminary test, a lack of peak compressive stress was noticed, which is due to the seven days of curing and the high w/c-ratio; for this second preliminary test, all mixtures reduced the w/c-ratio to 0.4. The tests were performed right after the curing process. The fiber used in some specimens corresponds to fiber 'A', which mechanical properties can be found in Tab. 4.2. The testing matrix is shown in Tab. A.4.

Table A.4: Preliminary testing matrix #2.

Specimen	Test	Mixture	Superplasticizer (ml)	Fiber content (%)
PT2_01	C	1	18.0	0.0
PT2_02	C	1	18.0	0.0
PT2_03	T	1	6.0	0.0
PT2_04	T	1	6.0	0.0
PT2_05	C	1	3.0	0.0
PT2_06	C	1	3.0	0.0
PT2_07	C	1	3.0	0.0
PT2_08	C	1	3.0	0.0
PT2_09	T	1	6.0	1.23
PT2_10	T	1	6.0	1.23
PT2_11	C	1	6.0	1.23
PT2_12	C	1	6.0	1.23
PT2_13	C	1	6.0	0.0

C : Compression
T : Direct tensile

A.2.1. Compression test

As shown in Tab. A.4, the test considered compression stress assessment. The mixture process used is the same as the previous preliminary test.

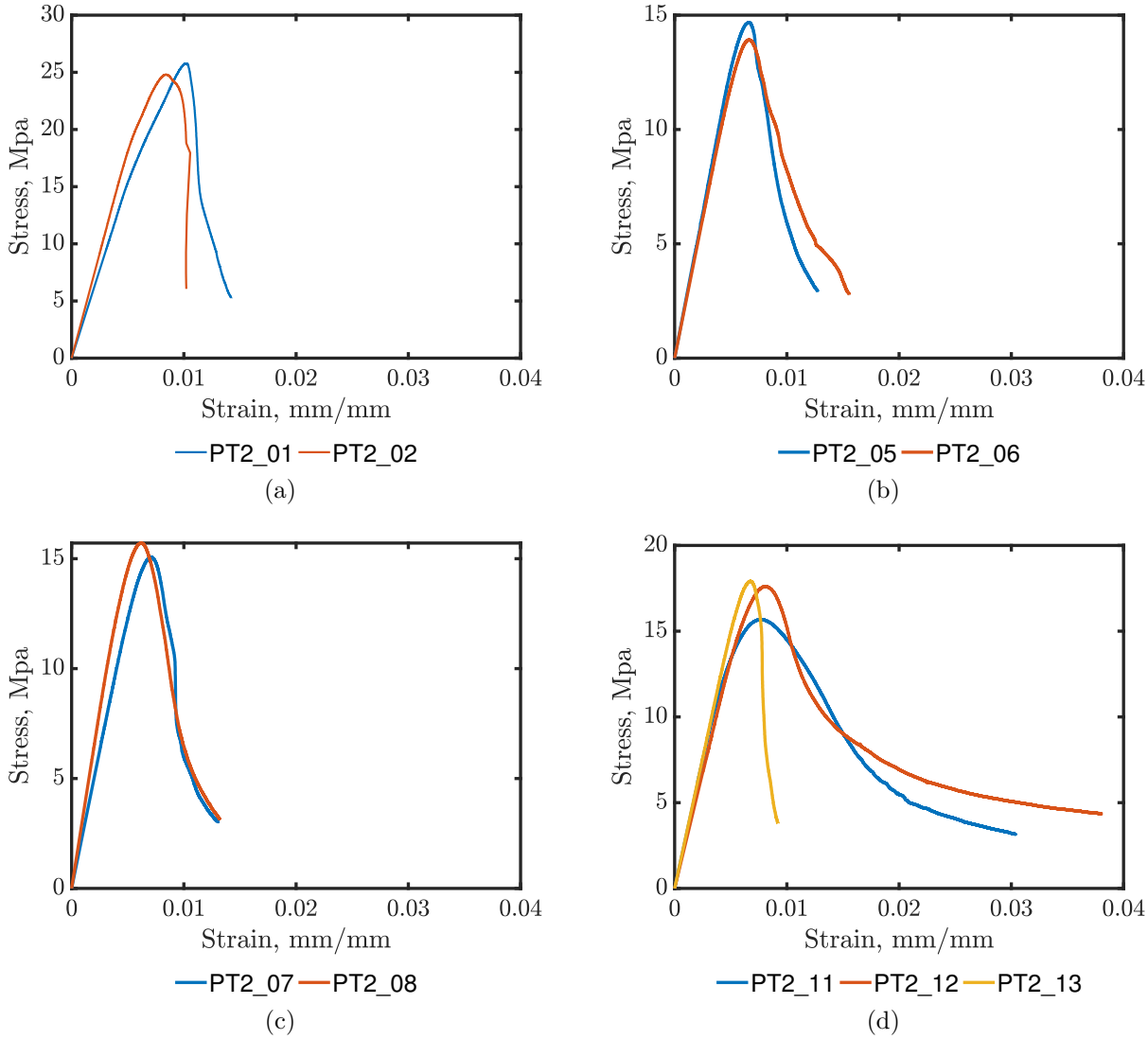

Figure A.2: Compression test specimens result.

Due to the direct tensile test results, which will be discussed in the next section, four mixtures with the same characteristics were tested in compression (PT2_05 - 08). This helped to conclude that the tests had despicable variability and reinsure that the mixture process is well implemented. The results of the compression tests are shown in Tab. A.5

Table A.5: Main data of preliminary test #2.

Specimen	E_c (MPa)	Peak Stress (MPa)	Strain at peak (-)	Max. Strain (-)
PT2_01	3085.527	25.779	0.01021	0.01423
PT2_02	3666.464	24.805	0.00838	0.01056
PT2_05	2541.935	14.682	0.00665	0.01274
PT2_06	2443.245	13.926	0.00663	0.01557
PT2_07	2504.749	15.076	0.00711	0.01307
PT2_08	3240.415	15.712	0.00624	0.01321
PT2_11	2993.327	15.684	0.00767	0.03038
PT2_12	2706.249	17.608	0.00805	0.03803
PT2_13	3039.828	17.911	0.00669	0.00920

A.2.2. Direct tensile test

Direct tensile tests were performed on the second preliminary testing in both specimens with PVA fiber content and plain concrete with coarse aggregate. Testing was performed by the INSTRON® universal machine model 600LX, with displacement control at a 0.2 mm/min rate. To measure both displacement and load, the internal INSTRON® dial and cell load was used. To hold the specimen into the machine, it was necessary to use circular steel plates with a 150 mm diameter and a steel bar ϕ25 welded normal to the plate surface. Then, the plate is glued to the specimen by a Sikadur® 31 epoxy adhesive and left drying for five days. Finally, the specimen is placed into the machine, and the mechanical jaws are tightened. The test setup is shown in Fig. A.3.

Figure A.3: Direct tensile test setup.

The main result obtained by the test are shown in Fig. A.5 and Tab. A.6. There were in-

consistencies and unexpected results. Some specimens failed in planes should not have failed (e.g., at the epoxy gluing in the borders), shown in Fig. A.4(b). Only two specimens had the expected failure, one of each mixture. Thus, the results among them are not comparable, and the PT2_09 had two failure planes, one torsional due to the border condition applied by the testing machine, and the other as the expected failure, same as PT2_04 (Fig. A.4(a)). Either way, at the specimens with expected failure, it was noticed that the fiber was correctly distributed along the transversal section.

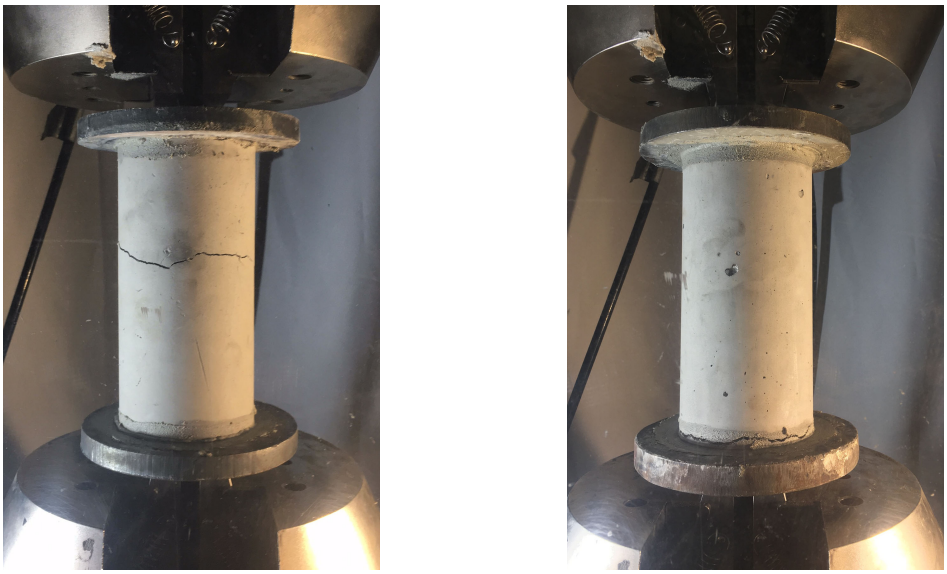

(a) Expected failure - PT2_04.

(b) Failure due to border conditions - PT2_03.

Figure A.4: Mixture consistency.

Besides, the testing machine had a measurement problem in its cell load for low displacement rates. That can be noticed in Fig. A.5(a) with the PT2_04 curve, where after the failure, the load should have dropped to zero, but it remained constant instead. In conclusion, adding to the results inconsistency and testing machine measurement problems, the direct tensile test demands a high time consumption on its setup and the fact that the results are not consistent even if both fail as expected due to the mixture orthotropy (i.e., fiber distribution inside the specimen). Considering all the above, the direct tensile test was discarded for future testing, and the author had to find another way to assess the residual strength of coarse aggregate PVA cementitious mixtures.

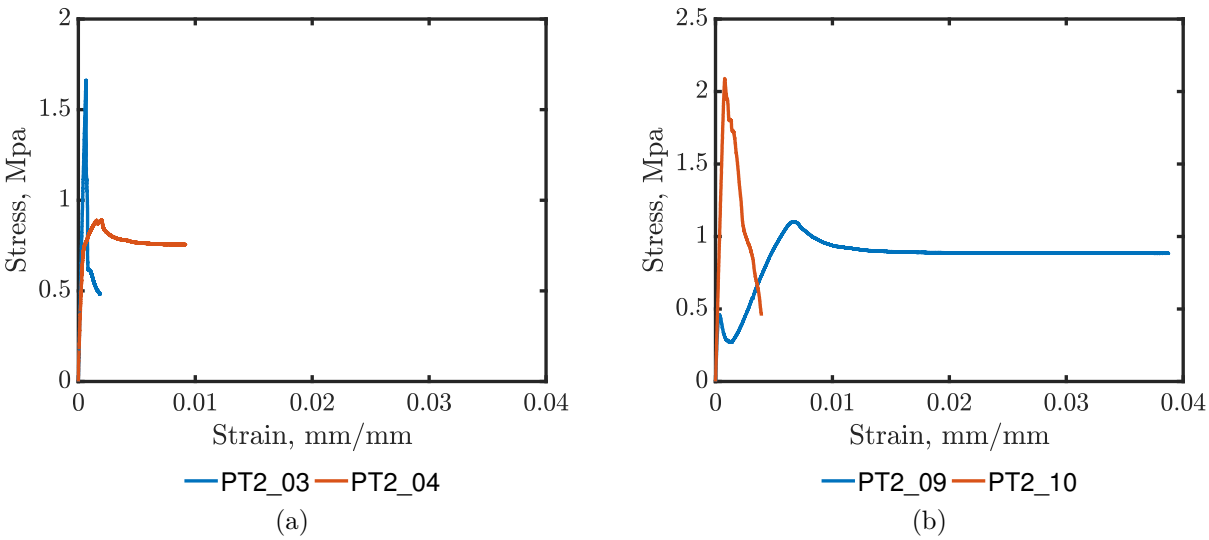

Figure A.5: Direct Tensile test specimens result.

Table A.6: Direct Tensile test specimens main results.

Specimen	E_c (MPa)	Peak Stress (MPa)	Strain at peak (-)	Max. Strain (-)
PT2_03	2946.065	1.663	0.00066	0.00186
PT2_04	3182.404	0.890	0.00198	0.00916
PT2_09	2204.804	1.102	0.00669	0.03876
PT2_10	2786.466	2.090	0.00078	0.00393

Appendix B

Ncorr methodology

In order to obtain the material strain of the studied element, it is required to select the images to analyze, these images must have one undeformed image, and the Region of Interest (ROI) must be visible in all pictures (no interference element between the studied element and the camera). With the image selection done, the images must be named correlatively to the time that they were taken, and must be named as TestImageName_#, starting at 0 (undeformed image). After naming the pictures selected to perform the analysis, it is needed to load the undeformed picture (Reference Image), this is accomplished by going to File>Load Reference Image. Next step is to select all the rest of the pictures, this is done by clicking File>Load Current Image(s) > Load all (memory heavy) or Load Lazy (slower but less memory) and then pick the rest of the images. The author recommends the second option, it will be slower but it all depends on the hardware used to perform the analysis (Fig. B.1).

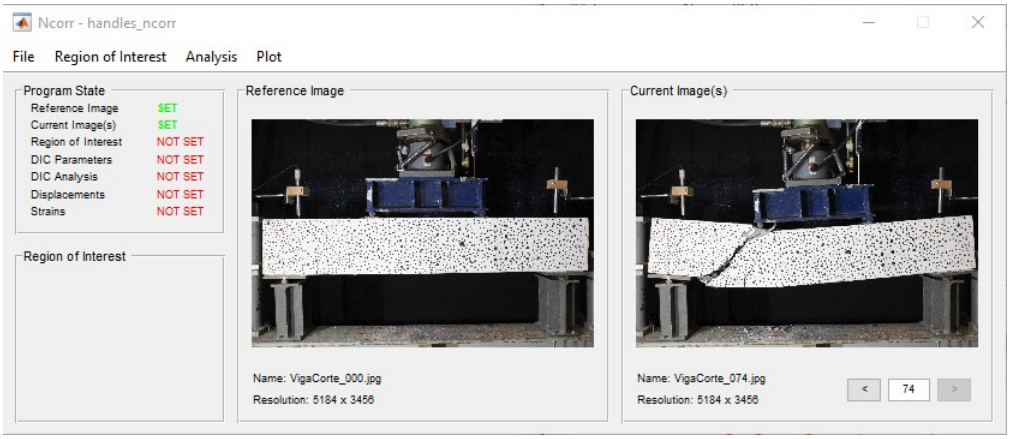

Figure B.1: Ncorr - Loading images procedure.

To continue the analysis is necessary to set the ROI; this area of the image is where all the displacements and strain are calculated, as mentioned before, it must be visible in all pictures. To set the ROI is necessary to click Region of Interest > Set Reference ROI and then click 'Draw ROI', it will automatically open a new window where a ROI can be drawn (Fig. B.2), click 'Finish' twice and continue to the next step.

Figure B.2: Ncorr - Draw ROI.

Consequently, the next step is to set the DIC parameters for the analysis (Analysis > Set DIC Parameters); the Subset Options are the main components of the analysis. It is essential to pick the smallest subset possible, which does not result in noisy displacement data to reduce the computational load. There are several pieces of literature available in order to choose the right Subset radius and Subset Spacing. Menus not mentioned previously, in the DIC parameter options, allow the user the choice of how many threads the CPU uses and the High Strain Analysis, which, if checked, refresh at each picture the ROI, the procedure is shown in Fig. B.3. More details of the analysis can be found in Blaber et al. (2015).

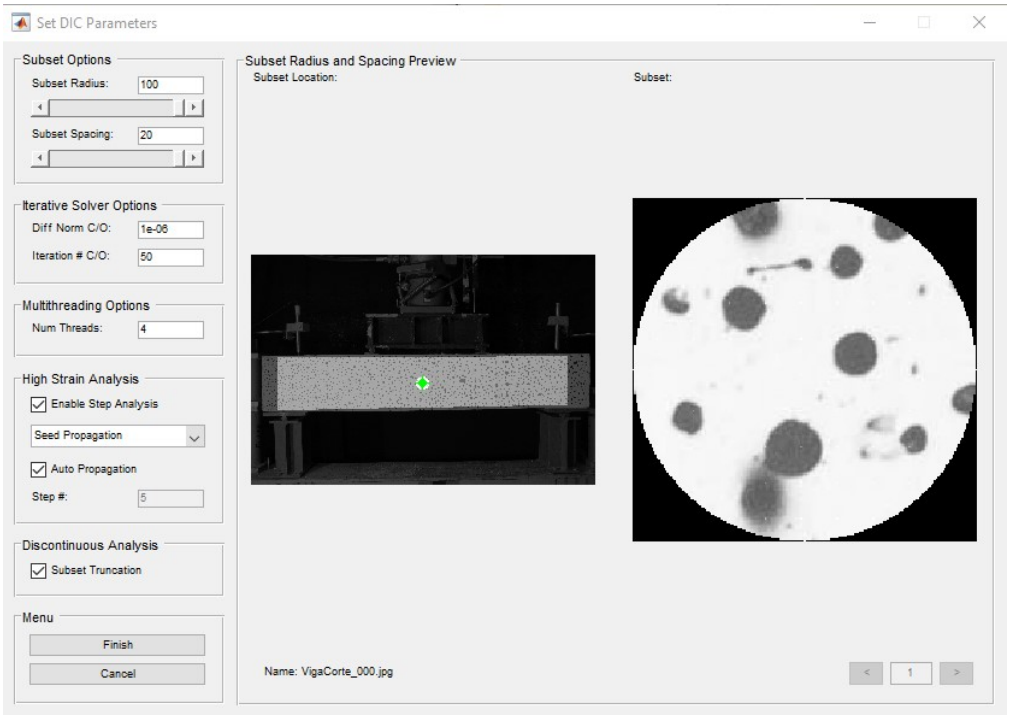

Figure B.3: Ncorr - DIC analysis parameters.

The procedure continues by selecting the Analysis Region (Analysis > Perform Analysis) and then placing the 'Seeds'. The number of Seeds will depend on the number of threads used to perform the analysis. The seeds are the starting convergence point, it is necessary

to place the seeds in strategic places but no over the high strain regions due to convergence problems (Fig. B.4).

Figure B.4: Ncorr - Placing 'Seeds'.

To finally perform the analysis, click 'Finish' twice on windows shown in Fig. B.4. When the analysis is done, it is time to set the correlation between pixels to mm (Analysis>Format Displacements). The software gives an option to set this up, just click on 'Get Unit Conversion' and draw a line on the image with a known distance (e.g. beam height). Once selected, the software automatically will format the displacement (Fig. B.5).

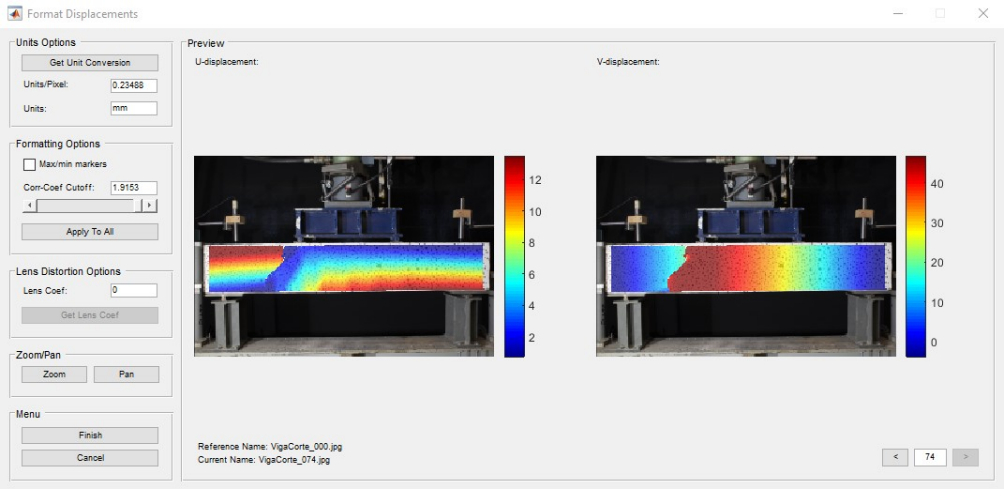

Figure B.5: Ncorr - Format displacement.

Finally, to get the analysis strains, go to Analysis > Calculate Strains, the software allows to select an appropriate strain radius to see the strain calculated dispersion on that radius.

Also, it allows to pick the calculation method (Lagrangian or Eulerian) and calculate strain in discontinuous analysis (Fig. B.6).

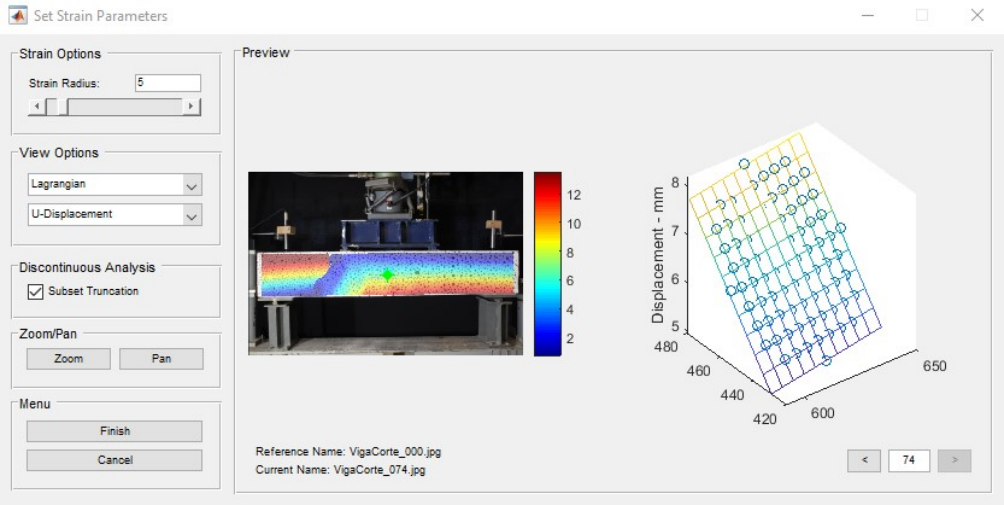

Figure B.6: Ncorr - Strain calculation.

Appendix C

Detailed compression results

In this appendix, the total compression test collected for each specimen is listed in the following tables (Table C.1 and C.2).

Table C.1: Compression results by specimen, part 1.

Specimen	Peak Stress (MPa)	Strain at peak (-)	Max. Strain (-)
M01-1	35.37	0.00362	0.00438
M01-2	34.34	0.00336	0.00532
M02-1	32.08	0.00358	0.01019
M02-2	34.57	0.00373	0.01515
M03-1	33.87	0.00448	0.01305
M03-2	30.25	0.00454	0.02555
M04-1	33.40	0.00466	0.00860
M04-2	32.75	0.00416	0.00438
M05-1	33.15	0.00399	0.00621
M05-2	31.48	0.00416	0.01046
M06-1	35.43	0.00370	0.01266
M06-2	30.98	0.00355	0.02600
M07-1	25.89	0.00550	0.00635
M07-2	26.01	0.00540	0.00767
M08-1	24.68	0.00423	0.00853
M08-2	23.16	0.00505	0.01509
M09-1	20.31	0.00486	0.01657
M09-2	23.21	0.00625	0.02615

Table C.2: Compression results by specimen cont.

Specimen	Peak Stress (MPa)	Strain at peak (-)	Max. Strain (-)
M10-1	18.04	0.00333	0.00602
M10-2	18.28	0.00315	0.01100
M11-1	19.79	0.00557	0.01689
M11-2	18.75	0.00515	0.01649
M12-1	18.83	0.00529	0.01169
M12-2	18.12	0.00593	0.03759
M13-1	35.37	0.00362	0.00438
M13-2	35.37	0.00362	0.00438
M14-1	32.32	0.00321	0.00927
M14-2	34.50	0.00333	0.00703
M15-1	30.82	0.00258	0.01653
M15-2	31.51	0.00316	0.00918
M16-1	23.75	0.00489	0.00745
M16-2	21.87	0.00450	0.00536
M17-1	24.88	0.00500	0.00603
M17-2	23.70	0.00471	0.01117
M18-1	22.93	0.00402	0.00692
M18-2	25.19	0.00559	0.00963
M19-1	18.04	0.00336	0.00606
M19-2	18.28	0.00315	0.01100
M20-1	19.79	0.00511	0.00671
M20-2	18.91	0.00497	0.02520
M21-1	17.77	0.00469	0.01214
M21-2	20.01	0.00471	0.01758

Appendix D

DIC analysis results

In this appendix, strain fields obtained by DIC analysis data are shown and ordered by type of beams.

D.1. Long beam with plain concrete

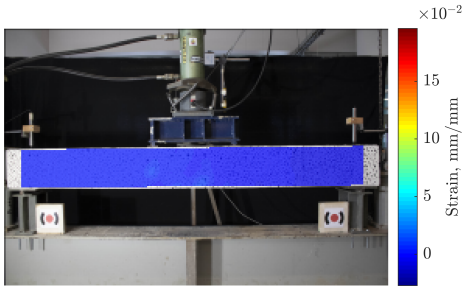

(a) Deflection = 28.4 mm.

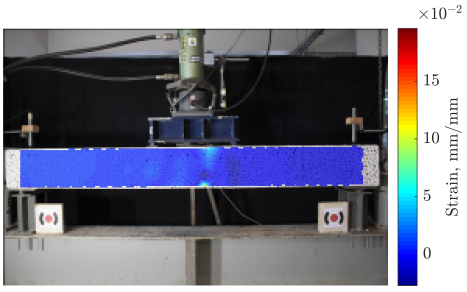

(b) Deflection = 105.8 mm.

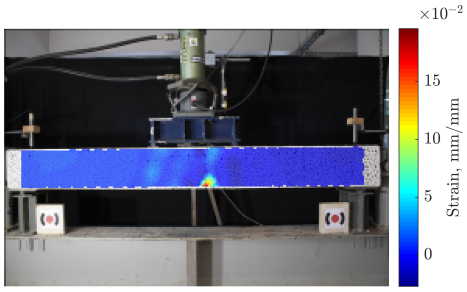

(c) Deflection = 145.9 mm.

Figure D.1: Strain ε_{xy} development over time, long beam.

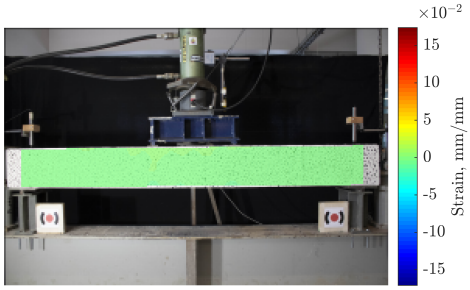

(a) Deflection = 28.4 mm.

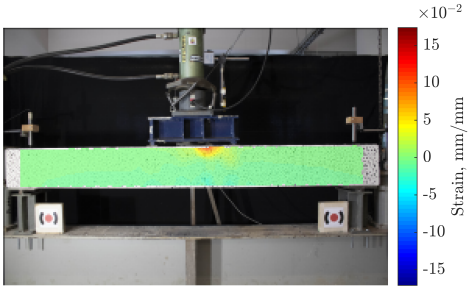

(b) Deflection = 105.8 mm.

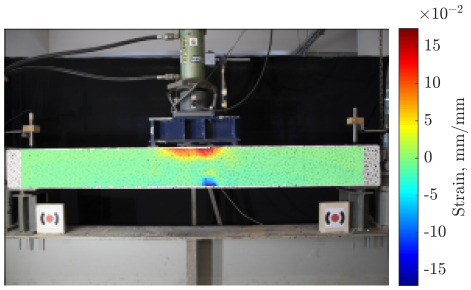

(c) Deflection = 145.9 mm.

Figure D.2: Strain ε_{yy} development over time, long beam.

D.2. Long beam with PVA fiber

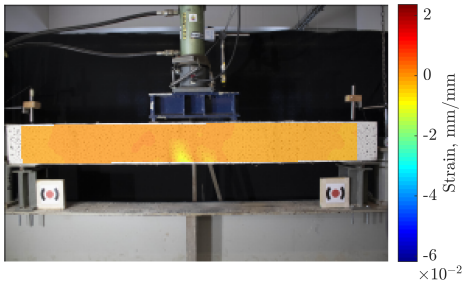

(a) Deflection = 19.8 mm.

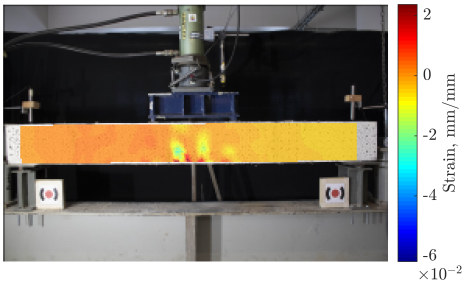

(b) Deflection = 68.3 mm.

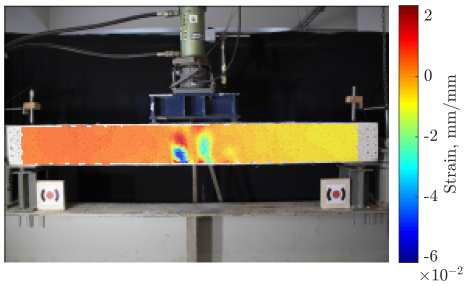

(c) Deflection = 117.3 mm.

Figure D.3: Strain ε_{xy} development over time, long beam with PVA.

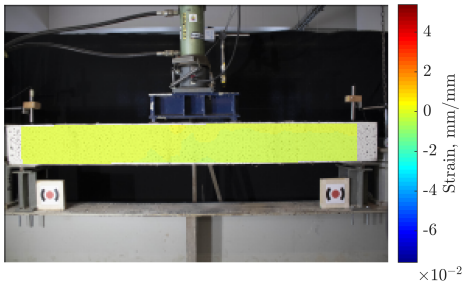

(a) Deflection = 19.8 mm.

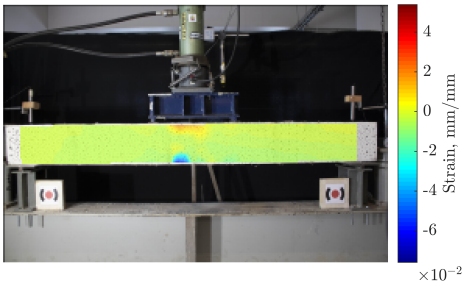

(b) Deflection = 68.3 mm.

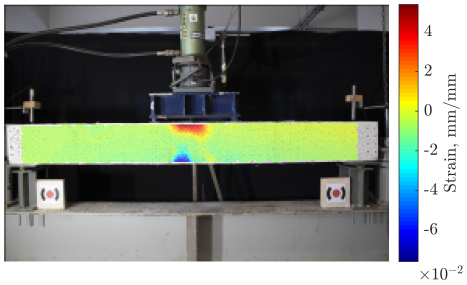

(c) Deflection = 117.3 mm.

Figure D.4: Strain ε_{yy} development over time, long beam with PVA.

D.3. Short beam with plain concrete

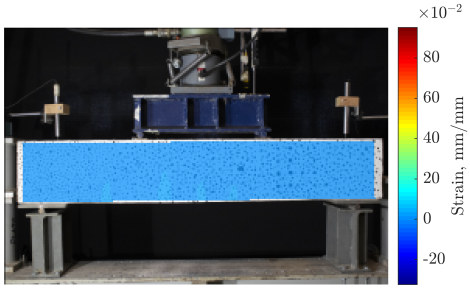

(a) Deflection = 6.7 mm.

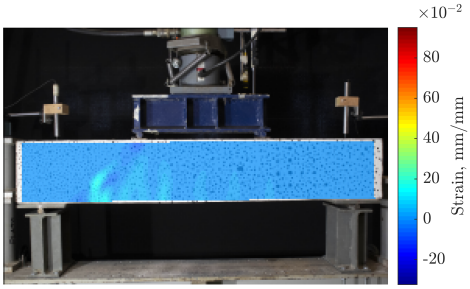

(b) Deflection = 27.9 mm.

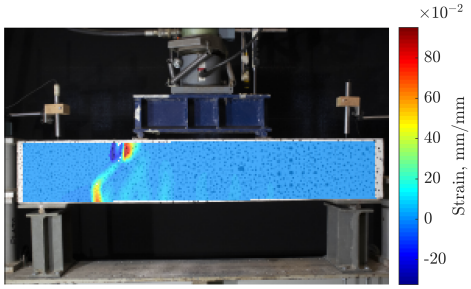

(c) Deflection = 37.6 mm.

Figure D.5: Strain ε_{xx} development over time, short beam.

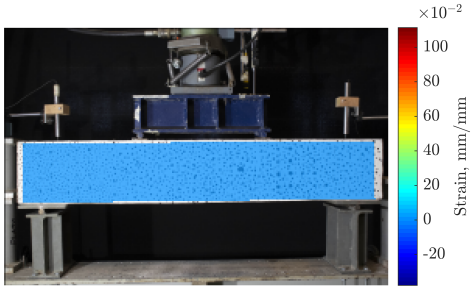

(a) Deflection = 6.7 mm.

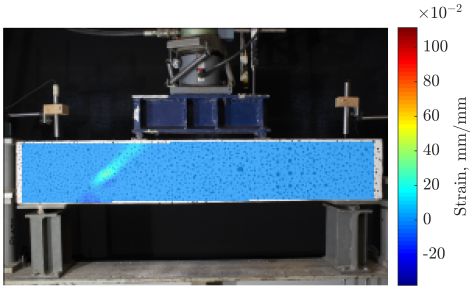

(b) Deflection = 27.9 mm.

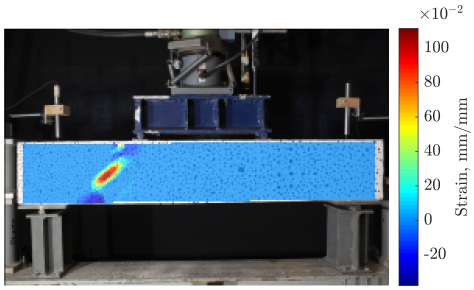

(c) Deflection = 37.6 mm.

Figure D.6: Strain ε_{yy} development over time, short beam.

D.4. Short beam with PVA fiber

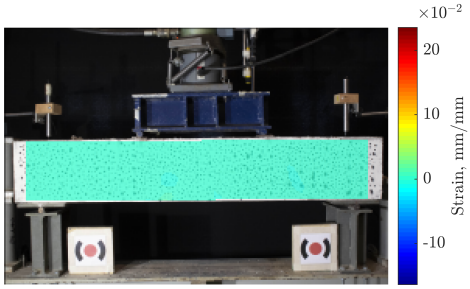

(a) Deflection = 5.6 mm.

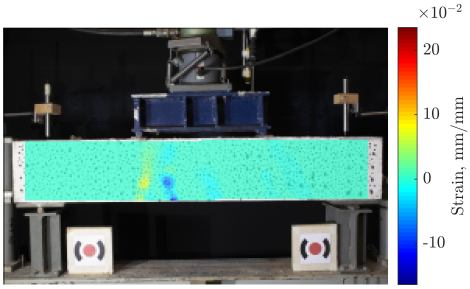

(b) Deflection = 37.3 mm.

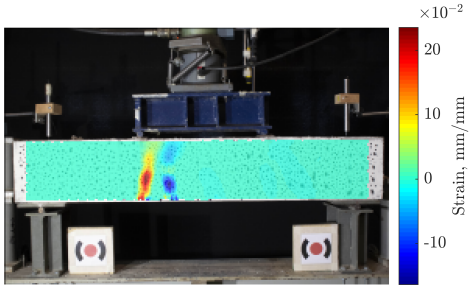

(c) Deflection = 72.8 mm.

Figure D.7: Strain ε_{xy} development over time, short beam with PVA.

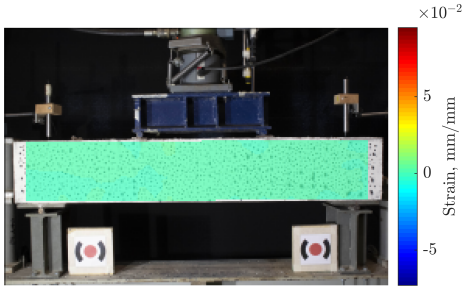

(a) Deflection = 5.6 mm.

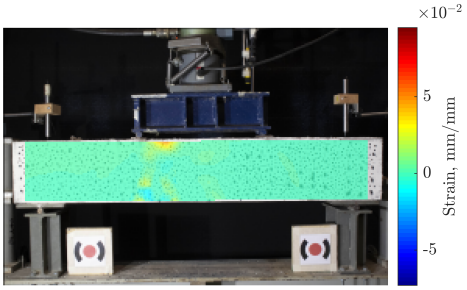

(b) Deflection = 37.3 mm.

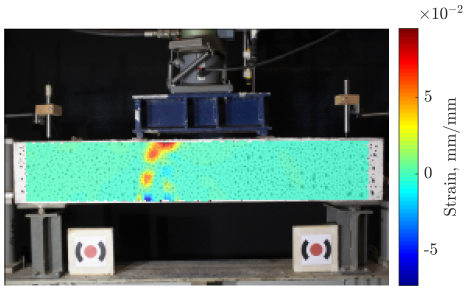

(c) Deflection = 72.8 mm.

Figure D.8: Strain ε_{yy} development over time, short beam with PVA.

Appendix E

E-SFI strain field

In this appendix, strain fields obtained by the analytical model using E-SFI element are shown and ordered by type of beams.

E.1. Long beam with plain concrete

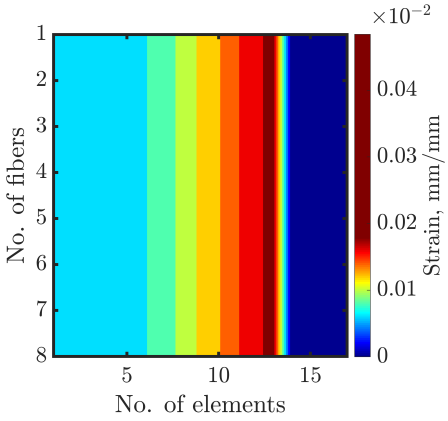

(a) Deflection = 28.4 mm.

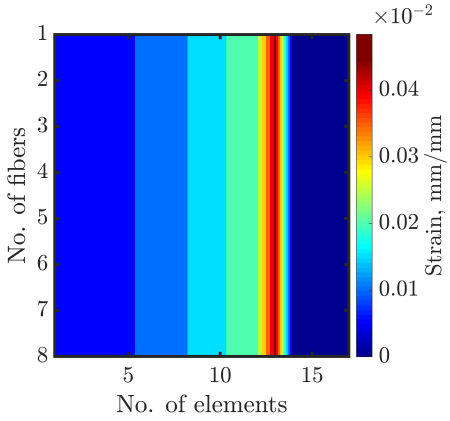

(b) Deflection = 105.8 mm.

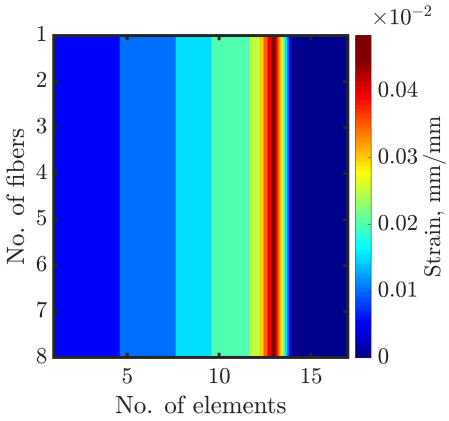

(c) Deflection = 145.9 mm.

Figure E.1: Strain ε_{xy} development over time, long beam with plain concrete.

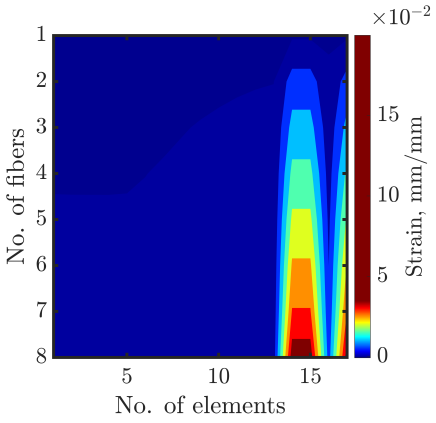

(a) Deflection = 28.4 mm.

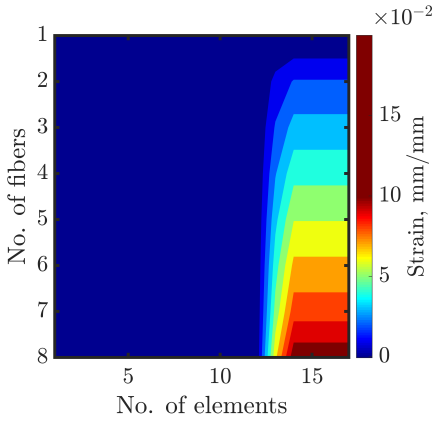

(b) Deflection = 105.8 mm.

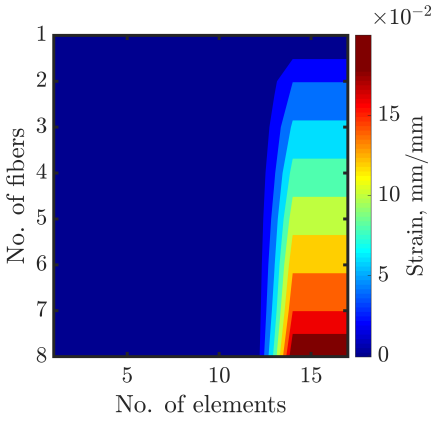

(c) Deflection = 145.9 mm.

Figure E.2: Strain ε_{yy} development over time, long beam with plain concrete.

E.2. Long beam with PVA fiber

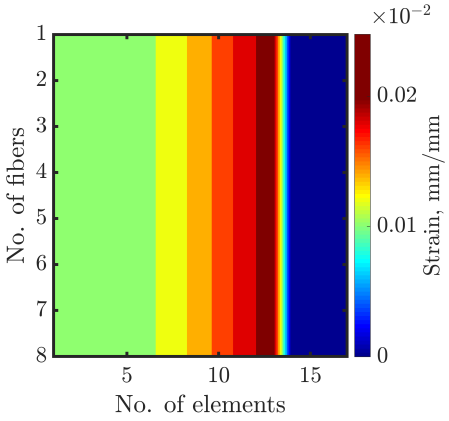

(a) Deflection = 19.8 mm.

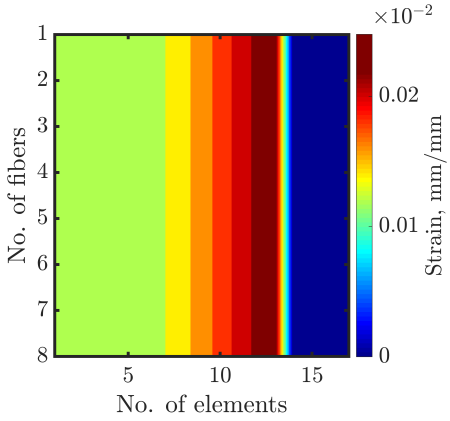

(b) Deflection = 68.3 mm.

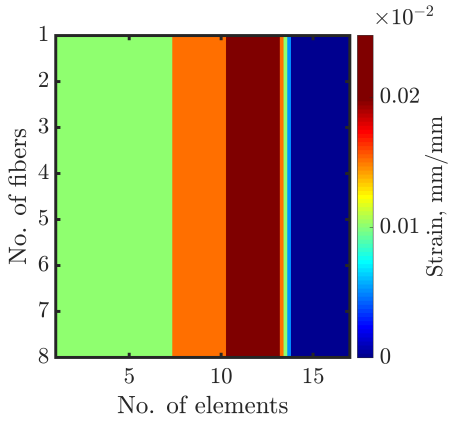

(c) Deflection = 117.3 mm.

Figure E.3: Strain ε_{xy} development over time, long beam with PVA.

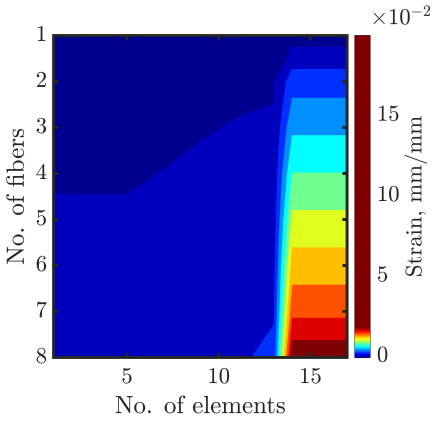

(a) Deflection = 19.8 mm.

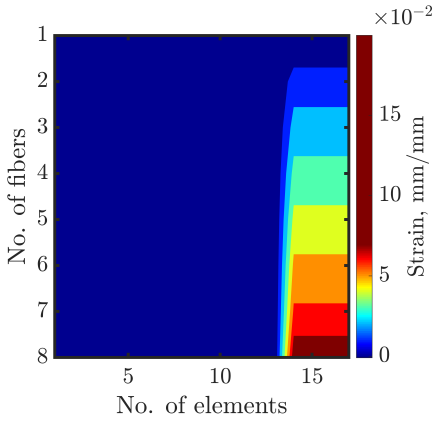

(b) Deflection = 68.3 mm.

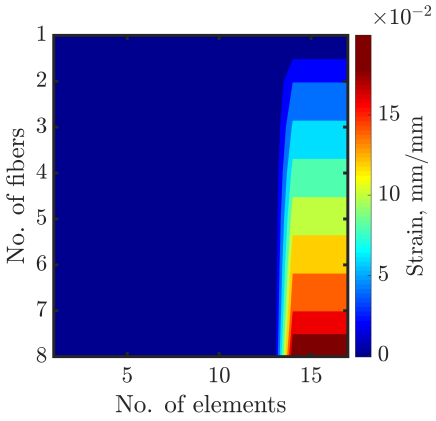

(c) Deflection = 117.3 mm.

Figure E.4: Strain ε_{yy} development over time, long beam with PVA.

E.3. Short beam with plain concrete

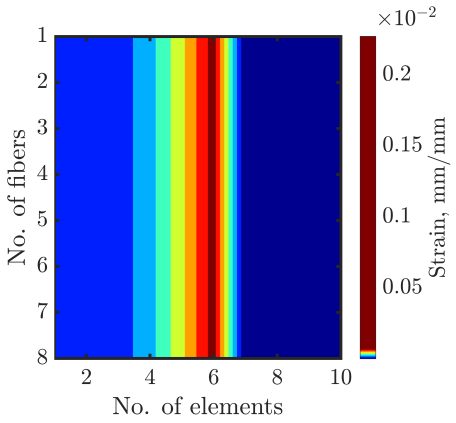

(a) Deflection = 6.7 mm.

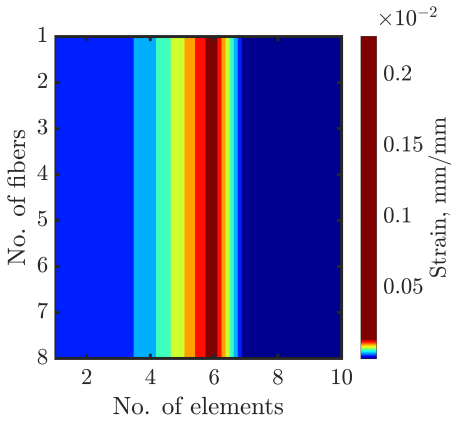

(b) Deflection = 27.9 mm.

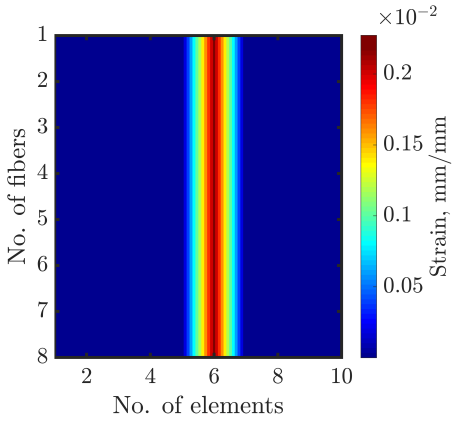

(c) Deflection = 37.6 mm.

Figure E.5: Strain ε_{xx} development over time, short beam with plain concrete.

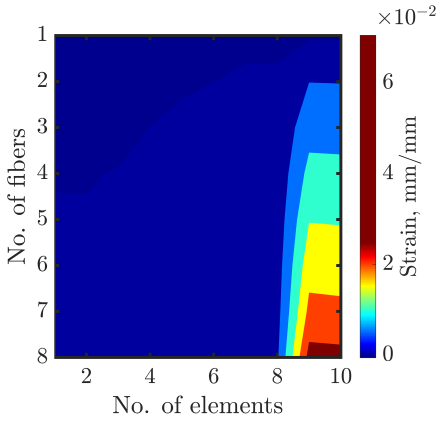

(a) Deflection = 6.7 mm.

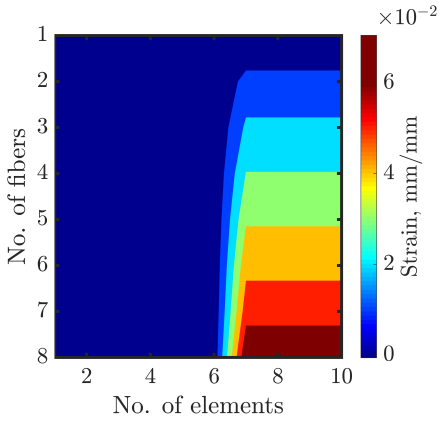

(b) Deflection = 27.9 mm.

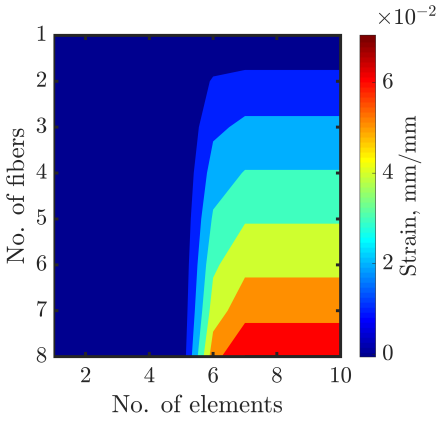

(c) Deflection = 37.6 mm.

Figure E.6: Strain ε_{yy} development over time, short beam with plain concrete.

E.4. Short beam with PVA fiber

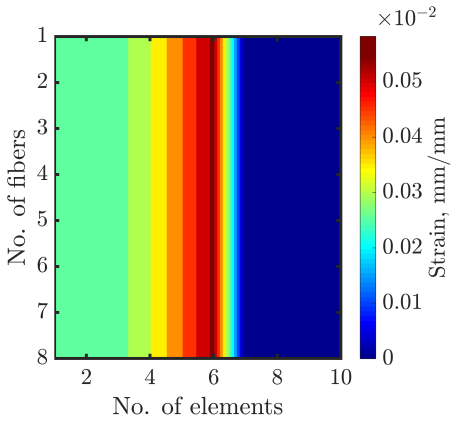

(a) Deflection = 5.6 mm.

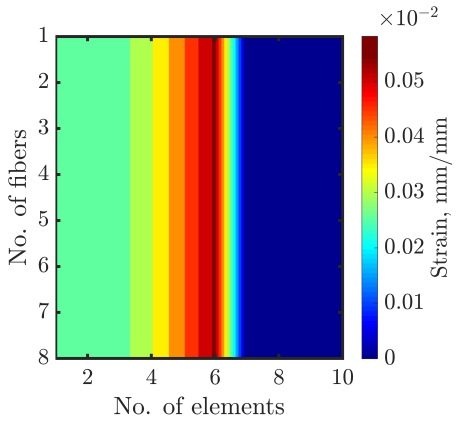

(b) Deflection = 37.3 mm.

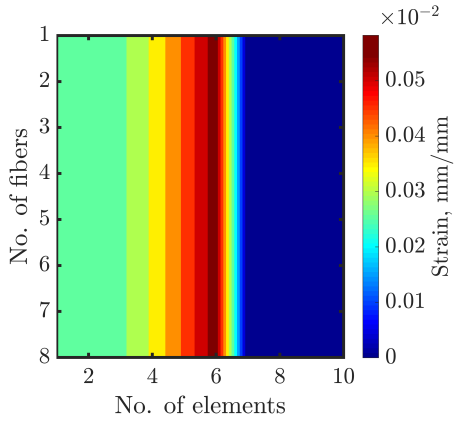

(c) Deflection = 72.8 mm.

Figure E.7: Strain ε_{xy} development over time, short beam with PVA.

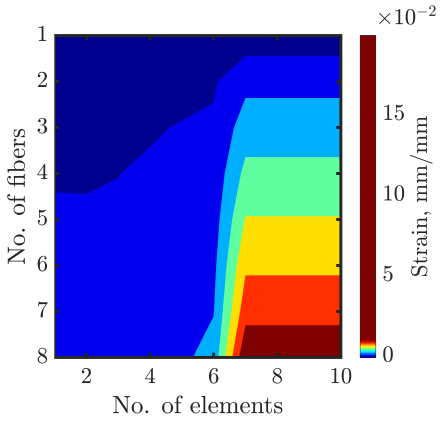

(a) Deflection = 5.6 mm.

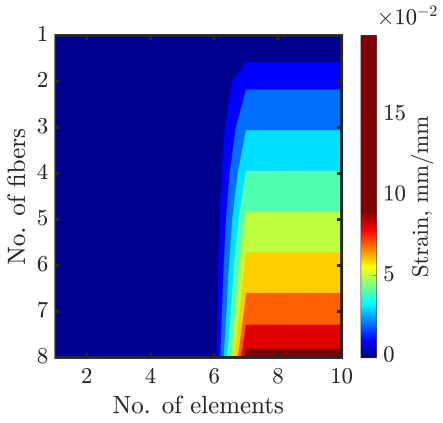

(b) Deflection = 37.3 mm.

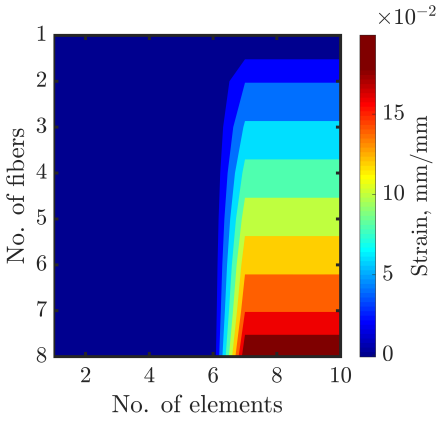

(c) Deflection = 72.8 mm.

Figure E.8: Strain ε_{yy} development over time, short beam with PVA.